Dissertation
submitted to the
Combined Faculties for the Natural Sciences and for Mathematics
of the Ruperto-Carola University of Heidelberg, Germany
for the degree of
Doctor of Natural Sciences

presented by

Diplom-Physiker: Jan Jakob Wilkens
born in: Munich, Germany

Oral examination: 26th May 2004

Evaluation of Radiobiological Effects in Intensity Modulated Proton Therapy:

New Strategies for Inverse Treatment Planning

Referees: PD Dr. Uwe Oelfke
Prof. Dr. Josef Bille

Zusammenfassung

Untersuchung strahlenbiologischer Effekte in der intensitätsmodulierten Protonentherapie: Neue Strategien für die inverse Bestrahlungsplanung

Zur Zeit werden Variationen der relativen biologischen Wirksamkeit (RBW) in der Bestrahlungsplanung der intensitätsmodulierten Protonentherapie (IMPT) meist vernachlässigt. Um mögliche klinische Auswirkungen einer variablen RBW für gescannte Protonenstrahlen zu untersuchen, werden neue Strategien zur Beurteilung dieser strahlenbiologischen Effekte und zur Integration der RBW in die inverse Bestrahlungsplanung vorgestellt. Sie basieren auf einem schnellen Algorithmus zur dreidimensionalen Berechnung des dosis-gemittelten linearen Energietransfers (LET) als einem Maß der lokalen Strahlenqualität und auf einem einfachen phänomenologischen Ansatz für die RBW als Funktion der Dosis, des LET und des Gewebetyps. Es zeigte sich, dass der biologische Effekt aufgrund unterschiedlicher LET-Verteilungen stark von der jeweils verwendeten Scanning-Technik abhing. Neue Zielfunktionen zur Berücksichtigung von LET und RBW wurden in ein inverses Bestrahlungsplanungsprogramm integriert, welches nun eine gleichzeitige Vielfelder-Optimierung des biologischen Effekts in einer akzeptablen Zeit erlaubt. An mehreren klinischen Beispielen wird demonstriert, wie mit diesen Methoden nachteilige RBW-Effekte erkannt und durch die direkte Optimierung des Produkts von RBW und Dosis kompensiert werden können. Die vorgeschlagenen Strategien sind somit eine wertvolle Hilfe, um die Qualität von IMPT-Bestrahlungsplänen zu beurteilen und zu verbessern.

Abstract

Evaluation of Radiobiological Effects in Intensity Modulated Proton Therapy: New Strategies for Inverse Treatment Planning

Currently, treatment planning for intensity modulated proton therapy (IMPT) usually disregards variations of the relative biological effectiveness (RBE). To investigate the potential clinical relevance of a variable RBE for beam scanning techniques, new strategies for the evaluation of radiobiological effects and for the incorporation of the RBE into the inverse planning process are presented. These strategies are based on a fast algorithm for three-dimensional calculations of the dose averaged linear energy transfer (LET) as a measure of the local radiation quality, and on a simple phenomenological approach for the RBE as a function of dose, LET and tissue type. It was found that the biological effect depended strongly on the type of scanning technique used, mainly due to differences in the LET distributions. New objective functions that account for LET and RBE were integrated into an inverse planning software, which now allows simultaneous multi-field optimization of the biological effect in a reasonable time. With these methods, unfavourable RBE effects can be identified and compensated for by direct optimization of the product of RBE and dose, which is demonstrated for several clinical examples. The proposed strategies are therefore valuable tools to evaluate and improve the quality of treatment plans in IMPT.

Contents

Chapter 1

Introduction

Besides surgery and chemotherapy, radiation therapy is one of the three main options for treating tumour patients. Over the last years, advances in research and technology led to significant improvements in all fields of radiotherapy (for an overview see Webb 1993, 1997, 2001). While the majority of irradiations is done by high energy photons, another promising approach is the treatment with proton beams, which enjoys rising interest and importance with an increasing number of clinical proton therapy facilities worldwide. Due to the different depth dose characteristic of charged particles compared to X-rays, superior dose distributions in the patient and therefore higher tumour control and less side effects can be anticipated for treatments with proton beams.

The most sophisticated technique in proton therapy is *Intensity Modulated Proton Therapy* or IMPT (cf Lomax 1999), which involves narrow beam spots that are delivered to the patient in a scanning pattern (cf Goitein and Chen 1983, Pedroni et al. 1995). The intensity of the beam spots is modulated individually, and their relative weights are determined by an optimization algorithm to obtain the best possible treatment plan. This process is called *inverse treatment planning*, since it solves the problem of automatically finding the best set of treatment parameters for a given (prescribed) dose distribution rather than the other way round, which was the conventional approach in treatment planning systems.

Today, inverse planning for protons (cf Lomax 1999, Oelfke and Bortfeld 2001, Nill et al. 2004) is based on fast and reliable algorithms for dose calculation. However, the physical dose is apparently not the only parameter one should look at in treatment planning for protons, as there is experimental evidence that the biological effect caused by proton beams does not depend on the physical dose alone (e.g. Belli et al. 1993, Wouters et al. 1996, Skarsgard 1998, Paganetti et al. 2002), but also on the energy spectrum of the beam. In other words: the same physical dose delivered by protons of different energy does not lead to the same biological results (e.g. in terms of cell survival). These radiobiological effects need careful investigation, and their consideration in the optimization process might be necessary to further improve the clinical results. The purpose of this work is therefore to develop new strategies to evaluate radiobiological effects in IMPT, and to integrate them into inverse treatment planning.

1.1 The relative biological effectiveness (RBE)

The biological effect of proton beams in comparison to a reference radiation is described by the *Relative Biological Effectiveness* or RBE (cf Hall 2000, chap. 7, Wambersie and Menzel 1997, Wambersie 1999). It is defined as the ratio of the dose of the reference radiation (D_{ref}) and the respective proton dose (D_{p}) required to yield the same biological effect (e.g. cell survival level S):

$$\mathrm{RBE}(S) = \frac{D_{\mathrm{ref}}(S)}{D_{\mathrm{p}}(S)}. \tag{1.1}$$

Currently most clinical proton centres use a constant RBE of 1.1 relative to ^{60}Co (Gerweck and Kozin 1999, Paganetti et al. 2002), i.e. protons are assumed to be 10% more effective than ^{60}Co gamma-rays, although there is experimental evidence that the RBE is not constant. In general, the RBE of protons depends on the dose or dose per fraction, the tissue or cell type, the biological endpoint (e.g. cell survival or chromosome aberrations), the reference radiation and the radiation quality, i.e. the local energy spectrum of the protons (Skarsgard 1998, Hall 2000, Kraft 2000). The latter is often characterized by the *Linear Energy Transfer* or LET, which can be understood as a measure of the density of ionization events along the track of a proton. These dependencies of the RBE are most obvious for *in vitro* experiments with cell cultures (e.g. Hall et al. 1978, Blomquist et al. 1993, Belli et al. 1993, Wouters et al. 1996, Tang et al. 1997). In most of these studies, a clear increase of RBE with decreasing dose was found. Up to a certain LET maximum, increasing LET also causes higher RBE values, which leads to variations of RBE with depth in tissue, in particular at the end of the proton range. Beyond the LET maximum, the RBE decreases again.

On the other hand, smaller RBE variations were found for *in vivo* systems (e.g. in animal studies, cf Tepper et al. 1977, Gueulette et al. 2000, Ando et al. 2001). In particular, the dose dependency of the RBE is less pronounced *in vivo*, while the increase of the RBE at the end of the proton range can still be seen (e.g. Gueulette et al. 2001). Some studies also evaluated the clinical experience with proton therapy (e.g. Debus et al. 1997, Paganetti et al. 2002) and found no evidence that using a constant RBE of 1.1 significantly underestimated the real RBE, although this does neither prove that the RBE is constant, nor that it is exactly 1.1 in all cases.

At the moment, the ability to determine or predict variable RBE values for clinical applications is limited (Paganetti et al. 2002, Paganetti 2003). Therefore the use of a constant RBE of 1.1 is continued in clinical practice of proton therapy, although the RBE is in fact not constant. However, it is still under investigation whether the effects of a variable RBE can be clinically significant, and there are doubts that a constant factor of 1.1 is sufficient for all cases. At least the increased effectiveness at the end of the range of proton beams should certainly be accounted for in treatment planning (Paganetti et al. 2002). To clarify this situation, more radiobiological measurements are needed, especially for *in vivo* systems and clinically relevant endpoints. Additionally, fast and robust tools have to be developed that allow the integration of a variable RBE into the treatment planning process in order to investigate the potential impact of RBE variations for different irradiation conditions.

1.2 Objectives of this work

While new scanning techniques in intensity modulated proton therapy offer the possibility to create highly conformal dose distributions for almost any desired target volume, there are also some risks associated with them. It is therefore necessary to quantify and minimize the impact of these potentially adverse effects, which include intra- and interfraction organ motion, range uncertainties and the influence of a variable RBE. In this work, I will focus on the last point and investigate radiobiological effects.

The aims of this thesis are therefore to study the potential clinical impact of a variable RBE for various situations and compare these effects for different dose delivery techniques (e.g. distal edge tracking and 3D modulation, see chapter 2). This question is particularly interesting for IMPT since scanning techniques might show different biological properties than the conventional delivery with passive beam scattering systems. Thus, it is highly desirable to provide tools for a fast evaluation of RBE effects in treatment planning, i.e. a method to identify situations where a constant RBE of 1.1 is not sufficient in clinical practice. A first approach could be to take an existing model for a variable RBE (e.g. track structure models, cf Paganetti and Goitein 2001) and apply it to the treatment plan after the conventional optimization of the physical dose to obtain a three-dimensional distribution of RBE × dose (sometimes also called “biological dose” or “effective dose”).

While this method could certainly be used to study the impact of a variable RBE and to identify potentially dangerous situations, it does not offer an option to directly improve the biological outcome, since the optimization algorithm cannot take the RBE effects into account. Therefore we would rather like to include the RBE into the optimization process in order to achieve an optimized distribution of the biological effect or RBE × dose, because only this approach can answer the question if and how disadvantageous RBE effects can be compensated for in inverse treatment planning.

To integrate the RBE calculations into the optimization loop of inverse planning, a very efficient RBE model is required to keep the optimization times reasonable. This means that the track structure models (which need long computing times) are not suitable for this purpose. Instead, a phenomenological model based on experimental data for the RBE as a function of dose, LET and tissue type will be developed and employed in this work. Despite being simple, it has to account for the most relevant properties of the RBE, in particular the increase of RBE at the end of the proton range.

The assessment of RBE effects for complex IMPT treatment techniques therefore requires three main components: i) a fast algorithm for three-dimensional LET calculations to characterize and quantify the physical properties of the radiation field (cf Wilkens and Oelfke 2003, 2004), ii) a simple and reliable method to compute the corresponding RBE distributions and iii) the integration of these models into the inverse planning process.

The material in this thesis is organized as follows:

- In chapter 2, an introduction to proton therapy with particular emphasis on IMPT, scanning techniques and the inverse planning process is given.
- Chapter 3 describes the algorithm for three-dimensional LET calculations, which — in addition to the dose — will provide the physical input data for the following RBE calculations.
- In chapter 4, the phenomenological model for the RBE as a function of dose, LET and tissue type is presented and compared to experimental results.
- Chapter 5 then introduces new optimization strategies that integrate the RBE into the optimization process, and the effects of a variable RBE are discussed for several clinical examples.
- As an outlook, chapter 6 addresses the potential transfer of these strategies from protons to heavier charged particles, e.g. for radiotherapy with carbon ions.
- Finally, a summary and the main conclusions are given in chapter 7.

Chapter 2

Intensity Modulated Proton Therapy

The therapeutical use of proton beams was proposed by Wilson in 1946, and the first patients were irradiated in the 1950s and 1960s in the USA (Berkeley and Harvard), Sweden (Uppsala) and the former Soviet Union (Dubna and Moscow). Since then, more than 36 000 tumour patients have been treated with protons all over the world (Sisterson 2004). The number of proton facilities is increasing, and especially in the last few years a couple of new hospital based proton accelerators started their operation in the USA and Japan, while some more are under construction. Rather than the high energy physics laboratories, where the first patients were treated, these new machines are dedicated only to medical applications and can provide a patient friendly environment, higher patient throughput and research facilities in the fields of oncology and medical physics.

In Germany only the Hahn-Meitner-Institute (HMI) in Berlin currently irradiates patients with protons, though their 68 MeV beam is only used for the treatment of ocular tumours (Heese et al. 2001). However, several facilities with higher energies for deep seated tumours are planned or under construction, in particular a centre for protons and heavier ions at the University of Heidelberg and the Rinecker Proton Therapy Center (RPTC) in Munich. Listings of all operating and proposed facilities can be found in the *Particles* newsletter (Sisterson 2004).

Intensity modulated proton therapy (IMPT) is a special and relatively new technique of proton therapy. One could argue that almost every kind of proton therapy involves some degree of intensity modulation (e.g. the weighted superposition of pristine Bragg peaks to yield a spread-out Bragg peak). However, following the argument of Lomax (1999), IMPT is understood as a technique with several fields or beam ports that each create an inhomogeneous dose distribution in the target; these fields are optimized in such a way that their total dose distribution satisfies the clinical objectives, e.g. a homogeneous and conformal dose to the target volume while sparing neighbouring organs at risk. This is in agreement with the current understanding of intensity modulated radiotherapy for photons (IMRT, for an overview see Webb 2001). Compared to conventional techniques, intensity modulation can yield better target coverage and improved sparing of normal tissues.

In this chapter, I will summarize the fundamentals of proton therapy in general, and in particular of IMPT. Emphasis will be placed on those formulas and techniques that will be needed in the subsequent chapters of this work. More detailed introductions into the physics of proton therapy and into treatment planning for protons can be found in Bichsel (1968), Webb (1993, chap. 4), Webb (1997, chap. 6) and Oelfke (2002). In section 2.1, a brief review on the physical properties and therapeutical advantages of proton beams is given. I will then describe current delivery techniques (section 2.2), with the focus on scanning techniques that are employed in intensity modulated proton therapy. Finally, dose calculation algorithms and optimization strategies for treatment planning will be addressed in section 2.3.

2.1 Physical properties and therapeutical advantages of proton beams

2.1.1 Stopping power, range and dose

In contrast to uncharged particles like photons, protons as charged particles have a distinctive range in matter. The depth dose curve shows a characteristic maximum, called the Bragg peak (cf figure 2.1). The amount of energy that a proton looses per unit length of its track is called the stopping power $S(E)$, which can be obtained from Bethe's formula (see Johns and Cunningham 1983, ICRU 1993).

The range itself is defined as the position of the 80% dose behind the peak. The higher the initial velocity or the kinetic energy of the protons, the greater is the range. In the continuous slowing down approximation (CSDA), the range R for protons of energy E can be calculated easily from the energy dependent stopping powers $S(E)$ by

$$R(E) = \int_E^0 \frac{1}{S(E')} \mathrm{d}E'. \tag{2.1}$$

This range-energy relationship can be parameterized by a simple power law, which was already given by Wilson (1946):

$$R = \alpha E^p. \tag{2.2}$$

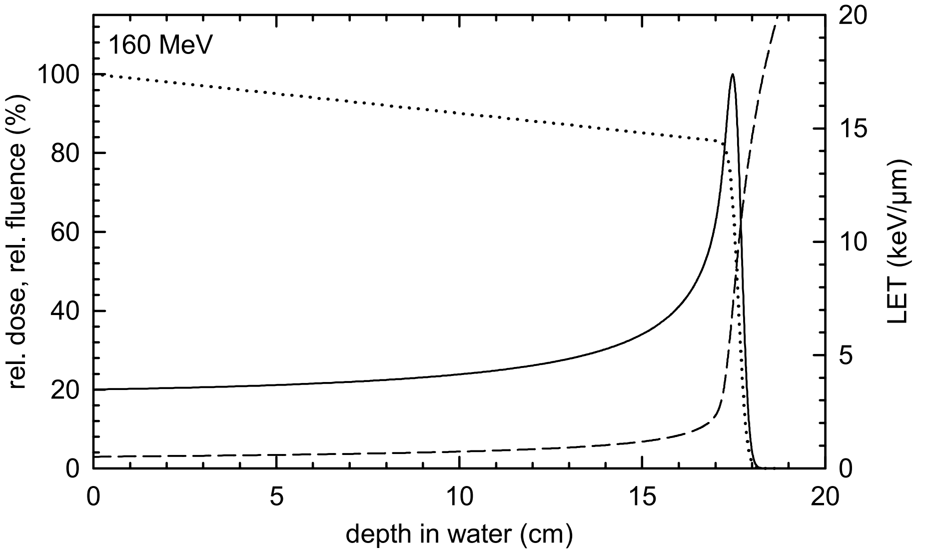

Figure 2.1: *Dose (——), fluence (······) and dose averaged LET (– – –, right ordinate) along the central axis for a 160 MeV proton beam. A similar figure was already given by Larsson (1961).*

Using the stopping powers given in ICRU report 49 (1993), Bortfeld (1997) gave as a best fit $\alpha = 0.0022$ cm MeV^{-p} and $p = 1.77$. The dose D at a specific point $\boldsymbol{x}$ (i.e. the absorbed energy per unit mass) can be obtained by

$$D(\boldsymbol{x}) = \frac{1}{\rho} \int_0^\infty S(E) \phi_E(\boldsymbol{x}) \mathrm{d}E, \tag{2.3}$$

where ρ is the density of the material and $\phi_E(\boldsymbol{x})$ the fluence spectrum with respect to energy. Strictly speaking, this is *cema* (converted energy per unit mass) rather than absorbed dose (Kellerer et al. 1992, ICRU 1998), which can be used as a good approximation of the dose.

The stopping power quantifies the density of ionization events along the proton track, and is usually given in units of keV/μm. It is strongly connected to the term “linear energy transfer” (LET), which will be discussed in more detail in chapter 3. In figure 2.1 the dose averaged LET as a local mean of the stopping power is also shown. The LET is low in the entrance region, and rises first slowly and then very steeply at or behind the Bragg peak.

The characteristic depth dose curve with the Bragg peak (figure 2.1) illustrates the therapeutical advantages of protons: the dose is low in the entrance region (where the beam passes through normal tissue to reach the tumour), and the high dose region of the Bragg peak can be conveniently placed in the target volume. Behind the peak, the steep dose falloff leads to an almost zero exit dose. The width of the Bragg peak is given by the range straggling of the protons and by the initial width of the energy spectrum. Analytical expressions for the depth dose curve have been developed by Bortfeld and Schlegel (1996) and Bortfeld (1997).

The lateral dose falloff ("penumbra") of a proton beam can be very sharp in the entrance region, but it becomes broader with increasing depth in the tissue due to multiple Coulomb scattering (Gottschalk et al. 1993). The lateral penumbra is therefore roughly the same as for mega-voltage photon beams from linear accelerators. To gain a therapeutical advantage in comparison to photons in the penumbra region, one would have to go to heavier charged particles like helium or carbon ions, which show less lateral scattering in tissue.

2.1.2 Coulomb and nuclear interactions

The stopping power $S(E)$ only accounts for Coulomb interactions. While those are certainly the majority, some protons also undergo nonelastic nuclear interactions. The latter lead to the production of secondary particles (mainly protons, neutrons and alpha particles, Paganetti 2002) and a reduction of the primary proton fluence with depth (cf figure 2.1 and Lee et al. 1993, Bortfeld 1997). While the dose due to secondary neutrons is very low (Agosteo et al. 1998, Schneider et al. 2002), secondary protons and alpha particles can contribute considerably to the dose, especially in the entrance region (Paganetti 2002). A useful application of nuclear interactions are the positron emission tomography (PET) measurements of β^+ activity produced by protons interacting with light elements like carbon, nitrogen and oxygen (e.g. Oelfke et al. 1996, Parodi et al. 2002), which can in principle be used to monitor the dose delivery process.

2.2 Delivery techniques for proton beams

2.2.1 Spread-out Bragg peaks

One single Bragg peak alone is in most cases not suitable for tumour treatments, simply because the spatial dimensions of the high dose region are too small. To irradiate larger targets, one has to superimpose several pristine peaks in a suitable way to obtain a homogeneous dose distributions in the planning target volume (PTV, cf ICRU 1999). The classical way to accomplish this for a single beam direction are the so-called spread-out Bragg peaks (SOBPs). Here several pristine peaks from the same incident beam angle are modulated in energy, i.e. their range in the tissue is shifted individually. By using appro-

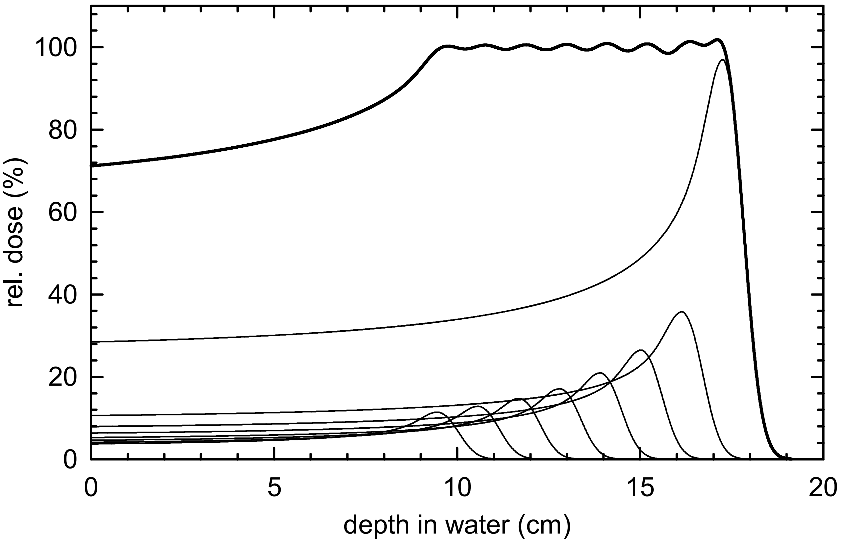

Figure 2.2: *Dose distribution in a spread-out Bragg peak (SOBP, thick line) with a modulation width of 9 cm. In this example, the SOBP is the sum of eight constituent pristine peaks with different positions and intensities (thin lines).*

priate weights for every peak, a homogeneous high dose region can be achieved (figure 2.2). The weights are usually obtained by an optimization algorithm (e.g. Gardey et al. 1999), so that the range and the modulation width (usually the distance between the proximal and distal 90% isodose) match the desired values.

In practice, SOBPs are mostly generated by rotating modulator wheels in the beam line, although in principle it could be done with active energy variation as well. Upstream of the modulator wheel, the beam is spread-out laterally, e.g. by a double scattering system (Koehler et al. 1977). Before the beam enters the patient, the field can be shaped to the lateral dimensions of the PTV by a brass collimator, and to the distal PTV edge by an acrylic compensator, as it is for example routinely done in the Northeast Proton Therapy Center (NPTC) in Boston (cf Bussière and Adams 2003).

This technique of SOBPs in conjunction with passive field shaping gives a homogeneous dose in the PTV for a single beam direction, and can of course be applied to several successive beam ports with different incident beam angles. However, this technique does not fully exploit all possible degrees of freedom, and intensity modulated proton therapy can be expected to yield superior dose distributions. The scanning techniques employed in IMPT will be discussed in the following section.

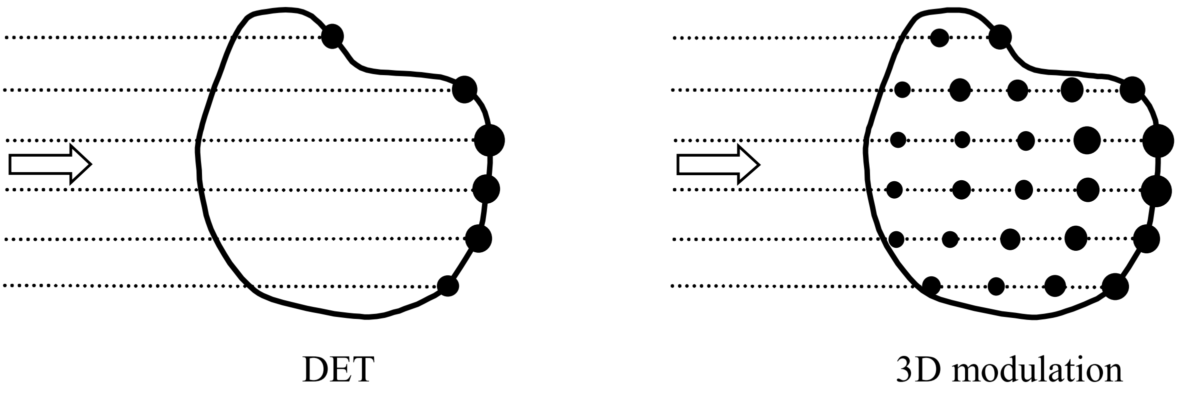

Figure 2.3: *Illustration of two spot scanning techniques for one of potentially many beam directions: the distal edge tracking technique (left) places the beam spots at the distal edge of the PTV (solid line) only, while beam spots are distributed all over the PTV for the 3D modulation technique (right).*

2.2.2 Scanning techniques

Lomax (1999) described four methods of intensity modulation for proton therapy. Based on the degrees of freedom for the modulation, they were named two-dimensional (2D), 2.5D and 3D modulation, while the fourth method was already called distal edge tracking (Deasy et al. 1997). The 2D and 2.5D techniques both work with narrow SOBPs, which are scanned across the field while their intensity is modulated in the two lateral dimensions. This can be done either using SOBPs of fixed extent (2D modulation), or by simultaneously varying the modulation width of the SOBP in order to match the respective dimensions of the planning target volume (2.5D modulation). For the two other techniques (DET and 3D modulation), narrow beam spots consisting of a single Bragg peak rather than SOBPs are placed in the PTV, and their individual weights are optimized to achieve the desired dose distribution.

For the purpose of this work, the latter approaches (DET and 3D modulation) seem to be more interesting, as we do not only want to calculate three-dimensional distributions of the relative biological effectiveness or RBE (which would be useful for all techniques), but we rather want to include the RBE in the optimization loop to obtain the optimal treatment plan in terms of the biological effect instead of the physical dose. This means that the physical dose in the PTV will not necessarily be homogeneous, which renders pre-defined SOBPs not very useful in this context. Only by optimizing the weights of all Bragg peaks individually, one can fully exploit all possible degrees of freedom. Therefore, I will concentrate in the following on the DET and 3D modulation techniques and will describe only them in more detail.

	DET	**3D modulation**
integral dose	⊕	⊖
optimization effort	⊕	⊖
delivery effort	⊕	⊖
delivery uncertainties	⊖	⊕
required number of beam ports	⊖	⊕
RBE effects	⊖ ?	⊕ ?

Table 2.1: *Summary of advantages and disadvantages of the DET and 3D modulation techniques. While DET is superior in terms of integral dose and the effort for optimization and delivery, it causes higher uncertainties in the delivery, can require more beam ports and might show unfavourable biological effects. The latter will be investigated in more detail in chapter 5.*

The distal edge tracking technique was proposed by Deasy et al. (1997). For every beam port, it uses single Bragg peaks that are placed only at the distal edge of the planning target volume. For one beam direction, this is illustrated in figure 2.3. The modulation is achieved by assigning individual weights to every beam spot. For a sufficient number of beam angles, this technique can yield a homogeneous dose in the PTV. The ratio of “energy deposited inside the target” and “energy deposited outside the target” can be maximized for the DET technique (Deasy et al. 1997), which leads to better sparing of the normal tissue surrounding the PTV and a reduced integral dose. This was also confirmed in theoretical studies by Oelfke and Bortfeld (2000) for centrally located targets in rotation therapy, especially for small target volumes.

On the other hand, the 3D modulation technique (sometimes also called 3D scanning) employs much more beam spots. They are placed all over the PTV, and their weights are varied independently (figure 2.3). The greater number of beam spots makes the whole technique more complex and increases the effort required in computing and optimization as well as for the delivery (Nill 2001). However, potential errors in the delivery process are reduced compared to DET, since 3D modulation is less sensitive to organ movements or to range uncertainties, which can for example be caused by errors in the calibration of the X-ray computed tomography (CT) scanner used. The 3D modulation has more degrees of freedom than DET and is therefore the most flexible technique. Especially when only a small number of beam ports is used, the 3D modulation becomes superior to DET, since it can achieve homogeneous dose distributions even for one single field (Lomax 1999).

Table 2.1 summarizes the advantages and disadvantages of the two techniques. One of the aims of this work is to answer the interesting question about the potential effects of a variable RBE in the two cases. Elevated RBE values can be expected at the distal edge of every single beam spot (e.g. Paganetti and Schmitz 1996, Paganetti et al. 2002). For DET, this may lead to higher RBE values at the border of the PTV than in its centre, while a more homogeneous RBE distribution is expected for 3D modulation (Nill 2001, p 70). This effect will be investigated in detail in chapter 5, and we will see whether such unfavourable effects can be compensated for by appropriate modifications in the optimization process.

For the actual delivery of narrow proton beams in a scanning pattern, several technical realizations have been developed over the last years. High energy proton beams are usually produced in cyclotrons or synchrotrons, and a beam line system is used to deliver the beam to the treatment room and to the patient. While only fixed beam lines were employed in the beginning of proton therapy, gantry systems that allow the irradiation of the patient from many beam ports were constructed later to provide more degrees of freedom. To direct the beam towards the patient, the gantries have to be equipped with bending magnets with large magnetic fields. This leads to an enormous size: the gantry at the Paul Scherrer Institute (Villigen) has a diameter of 4 m (Pedroni et al. 1995), which is even relatively small compared to other installations. The actual beam scanning in the two lateral directions is accomplished by magnetic deflection systems (e.g. Kanai et al. 1980). This can be done either using two sweeping magnets (Lorin et al. 2000), or by combining one sweeping magnet with a moveable patient couch to cover the second direction (Pedroni et al. 1995). One can distinguish between spot scanning and raster scanning methods. While the beam is only switched on at discrete positions in spot scanning, raster scanning involves the continuous scanning of the beam along a predefined trajectory. Ideally, the treatment planning software should account for the properties of the specific scanning system at the planning stage, although it is possible to convert discrete intensity maps into continuous scanning patterns later on (Trofimov and Bortfeld 2003).

2.3 Dose calculation and optimization

For the dose calculation in proton therapy a number of methods and algorithms are available (e.g. Hong et al. 1996, Carlsson et al. 1997, Deasy 1998, Russell et al. 2000; for an overview see Oelfke 2002). They are either based on broad beam or pencil beam models, or they rely on Monte Carlo techniques. Although more time consuming, Monte Carlo simulations are superior if inhomogeneities in the patient geometry have to be taken into account. A promising compromise are methods that involve two-dimensional scaling of pencil beams (Szymanowski and Oelfke 2002, 2003).

Due to the increased degrees of freedom for scanning techniques, inverse treatment planning is required in IMPT. This means that the individual weights of all beam spots have to be optimized by a computer program using appropriate optimization algorithms. In this work, a research version of the inverse planning tool *KonRad* is employed, which provides an option for IMPT with discrete spot scanning techniques (Nill et al. 2000, Nill 2001, Nill et al. 2004). The dose calculation in *KonRad* is done by a finite pencil beam algorithm using the concept of the D_{ij} matrix (see below and Nill 2001).

2.3.1 The concept of the D_{ij} matrix

The D_{ij} matrix (sometimes also called influence matrix) is a computational method to separate the dose calculation from the optimization. Let us consider a set of N beam spots that irradiate a patient or a phantom. At a certain voxel i, several of these beam spots will contribute to the dose D_i. Now D_{ij} shall denote the dose contribution of beam spot j in voxel i per unit fluence of beam spot j. The total dose D_i in voxel i is then given by

$$D_i = \sum_{j=1}^{N} D_{ij} w_j, \tag{2.4}$$

where w_j denotes the relative fluence weight of beam spot j.

The elements of the D_{ij} matrix can be filled by any desired dose calculation algorithm. Even complicated or time consuming methods like Monte Carlo could be used, since the D_{ij} matrix has to be calculated only once for a given treatment situation. During the iterations of the optimization loop, where the weights $\boldsymbol{w} = \{w_j\}$ are determined, the actual dose distribution can be updated easily and very fast by equation (2.4), which does not need any complicated computational procedures. Another advantage of the precalculated D_{ij} matrix approach is the possibility for multi-modality treatment planning, since subsets of the beam spots can utilize different radiation modalities, and the respective D_{ij} elements can be calculated by different algorithms (Nill 2001).

2.3.2 Optimization strategies

The aim of the optimization is to find a set of weights $\boldsymbol{w}$ so that the resulting dose distribution best matches the desired clinical objectives. The latter are usually given as constraints in terms of the physical dose, e.g. minimum and maximum dose levels for the PTV ($D_{\mathrm{min}}^{\mathrm{PTV}}$ and $D_{\mathrm{max}}^{\mathrm{PTV}}$) to ensure a homogeneous dose in the PTV, and maximum doses for organs at risk ($D_{\mathrm{max}}^{\mathrm{OAR}}$). Mathematically, the optimization is done by minimizing a so-called objective function by iterative algorithms. These algorithms can be either deterministic (e.g. the Newton gradient technique, which is implemented in *KonRad*), or stochastic methods like simulated annealing. An overview of optimization techniques can be found in Webb (2001, chap. 5.5), and a comparison of three algorithms using Newton's method in Holmes and Mackie (1994).

A typical example of an objective function for one PTV and one organ at risk is

$$F(\boldsymbol{w}) = F^{\mathrm{PTV}}(\boldsymbol{w}) + F^{\mathrm{OAR}}(\boldsymbol{w}) \tag{2.5a}$$

with

$$F^{\mathrm{PTV}}(\boldsymbol{w}) = \nu_{\mathrm{min}}^{\mathrm{PTV}} \sum_{i \in \mathrm{PTV}} \left[C_+(D_{\mathrm{min}}^{\mathrm{PTV}} - D_i(\boldsymbol{w}))\right]^2 + \nu_{\mathrm{max}}^{\mathrm{PTV}} \sum_{i \in \mathrm{PTV}} \left[C_+(D_i(\boldsymbol{w}) - D_{\mathrm{max}}^{\mathrm{PTV}})\right]^2 \tag{2.5b}$$

and

$$F^{\mathrm{OAR}}(\boldsymbol{w}) = \nu_{\mathrm{max}}^{\mathrm{OAR}} \sum_{i \in \mathrm{OAR}} \left[C_+(D_i(\boldsymbol{w}) - D_{\mathrm{max}}^{\mathrm{OAR}})\right]^2 , \tag{2.5c}$$

which is called the standard quadratic objective function. The user-defined penalty factors ν specify the relative importance of the respective dose constraints, and the C_+ operator selects only those voxels that violate the given constraint, i.e. $C_+(x) = x$ for $x > 0$ and $C_+(x) = 0$ otherwise (Oelfke and Bortfeld 2001, Oelfke 2002). This objective function can easily be extended to more complex situations, e.g. with more than one organ at risk.

Chapter 3

Three-Dimensional LET Calculations

3.1 Introduction

Besides other parameters like dose, tissue type and the biological endpoint, the RBE depends on the local energy spectrum (e.g. Belli et al. 1989, Skarsgard 1998, Kraft 2000). The latter is often referred to as “radiation quality” and can be characterized in first order by the linear energy transfer LET (ICRU 1970). Thus it is of interest to provide three-dimensional LET distributions in addition to the dose distributions. They can help to localize high LET regions, where the greatest variations of RBE are expected, or they can serve as input for the estimation of three-dimensional RBE distributions (see chapter 4). Additionally, the LET calculations also have potential applications for predicting the response of LET dependent dosimeters, e.g. in gel dosimetry (cf Bäck et al. 1999, Heufelder et al. 2003) or alanine detectors (cf Palmans 2003).

While the LET for monoenergetic protons is easily obtained from tables (ICRU 1993), the calculation of the mean local LET for realistic proton spectra, e.g. in spread-out Bragg peaks, is a more complicated task. This can in principle be accomplished by Monte Carlo simulations (Seltzer 1993, Berger 1993, Wouters et al. 1996). However, these simulations are still very time consuming and not well suited to iterative treatment planning, where LET distributions have to be calculated several times until the optimum treatment plan is found (cf chapter 5). A fast method for three-dimensional LET calculations is therefore presented in this work. It is based on an analytical model for the LET distribution along the central axis of broad proton beams in water and allows fast calculations of LET with simple parameters, namely the beam energy and the width of the initial energy spectrum.

This chapter is organized as follows: first, I will recall some definitions of LET (section 3.1.1), explain how LET distributions can be superimposed (section 3.1.2) and motivate the use of the dose averaged LET (section 3.1.3). In section 3.2, I will then describe the methods for three-dimensional LET calculations, before some results are presented (section 3.3) and discussed (section 3.4).

3.1.1 Definitions of LET

The term "linear energy transfer," which is in this work applied to protons only, is widely used to describe radiation quality. There are currently several definitions of LET in use, so I will first give an overview of some of these concepts.

All LET definitions are based on the stopping power. The total linear stopping power S for a given material is the sum of the linear collision stopping power S_{col} and the linear radiative stopping power S_{rad}. As the latter can be neglected for therapeutic protons (ICRU 1993), we get

$$S = S_{\text{col}} = \left(\frac{\mathrm{d}E}{\mathrm{d}l}\right)_{\text{col}}, \tag{3.1}$$

where $\mathrm{d}E$ is the energy lost by a proton in traversing a distance $\mathrm{d}l$ (ICRU 1998). Sometimes S_{col} denotes the electronic collision stopping power S_{el} only, i.e. the stopping power due to Coulomb interactions with electrons (ICRU 1993). In our context S shall always include the stopping power due to Coulomb interactions with nuclei (sometimes termed S_{nuc}), i.e. $S = S_{\text{el}} + S_{\text{nuc}}$.

ICRU report 60 (1998) defines the linear energy transfer as the restricted linear electronic stopping power L_{Δ}, where electrons released with kinetic energies greater than Δ are treated separately. The unrestricted linear energy transfer L_{∞} equals again S_{el}.

Besides that, the term LET is also employed to describe a mean value of the stopping power. This mean can be calculated either along the track of a single particle (ICRU 1970, Hall 2000) or by averaging the stopping powers of all particles at a certain point in a radiation field (ICRU 1970, Berger 1993). The latter approach will be used in this work: LET is here defined as a local mean of the stopping power S to quantify the local radiation quality.

Let us consider a point $\boldsymbol{x}$ in a radiation field. The protons contributing to the fluence at $\boldsymbol{x}$ will usually not be monoenergetic and will therefore have different stopping powers. In this situation it is useful to define an average stopping power or LET. As usual, average values can be defined in several ways. The two most common implementations are the track averaged LET and the dose averaged LET. The track averaged LET is the mean value of S weighted by fluence (or particle tracks, hence the name), i.e. it is the arithmetic mean of S for all protons present. For the dose averaged LET the stopping power of each individual proton is weighted by its contribution to the local dose.

The situation is further complicated, if several different species of charged particles are present at the point $\boldsymbol{x}$. In proton therapy this is almost always the case, as secondary particles produced in nonelastic nuclear interactions include charged particles that are heavier than protons (e.g. He ions). One can then calculate a mean LET for each particle type separately, using the respective stopping powers and energy spectra, and average them to get a total LET (Seltzer 1993, Berger 1993). However, as a simplification only the “pure” proton LET will be considered in this work, i.e. the LET contributions of all charged particles other than protons will be disregarded.

As shown above, the track and dose averaged LET depend on the local energy spectrum at the point $\boldsymbol{x}$. In the following, the spectrum will be described in terms of the particle’s residual range rather than its energy. This is possible because there is a unique relation between the energy and the residual range (cf equation (2.2)) in the continuous slowing down approximation (CSDA). A respective range-energy table was published in ICRU report 49 (1993).

Let r denote the residual range of an individual proton at a point $\boldsymbol{x}$, and $\varphi_r(\boldsymbol{x})$ the local particle spectrum at this point, i.e. $\varphi_r(\boldsymbol{x})\mathrm{d}r$ gives the fluence of protons at $\boldsymbol{x}$ with residual ranges between r and $r + \mathrm{d}r$. The total particle fluence at $\boldsymbol{x}$ will be $\int_0^\infty \varphi_r(\boldsymbol{x})\mathrm{d}r$. The track averaged linear energy transfer $L_\mathrm{t}(\boldsymbol{x})$ at $\boldsymbol{x}$ is then given by

$$L_\mathrm{t}(\boldsymbol{x}) = \frac{\displaystyle\int_0^\infty \varphi_r(\boldsymbol{x})S(r)\mathrm{d}r}{\displaystyle\int_0^\infty \varphi_r(\boldsymbol{x})\mathrm{d}r}, \tag{3.2}$$

where $S(r)$ is the stopping power of protons with residual range r. Similar to the notation used by Berger (1993), the dose averaged linear energy transfer $L_\mathrm{d}(\boldsymbol{x})$ at $\boldsymbol{x}$ is defined as

$$L_\mathrm{d}(\boldsymbol{x}) = \frac{\displaystyle\int_0^\infty \varphi_r(\boldsymbol{x})S^2(r)\mathrm{d}r}{\displaystyle\int_0^\infty \varphi_r(\boldsymbol{x})S(r)\mathrm{d}r}. \tag{3.3}$$

For monoenergetic protons both the track averaged and the dose averaged LET equal the stopping power S.

3.1.2 Superposition of LET distributions

For spread-out Bragg peaks and/or beams from more than one direction the LET distributions for the superposition of several beam spots or beams have to be computed. Let us therefore consider n beams or beam spots with local spectra $\varphi_{r,j}(\boldsymbol{x})$ $(j = 1 \ldots n)$ at a point $\boldsymbol{x}$. The total spectrum $\varphi_r(\boldsymbol{x})$ will just be the sum of $\varphi_{r,j}(\boldsymbol{x})$ for all beams. As the summation and the integration can be permuted, equations (3.2) and (3.3) become

$$L_\mathrm{t}(\boldsymbol{x}) = \frac{\displaystyle\sum_{j=1}^{n} \int_0^\infty \varphi_{r,j}(\boldsymbol{x}) S(r) \mathrm{d}r}{\displaystyle\sum_{j=1}^{n} \int_0^\infty \varphi_{r,j}(\boldsymbol{x}) \mathrm{d}r} \tag{3.4}$$

and

$$L_\mathrm{d}(\boldsymbol{x}) = \frac{\displaystyle\sum_{j=1}^{n} \int_0^\infty \varphi_{r,j}(\boldsymbol{x}) S^2(r) \mathrm{d}r}{\displaystyle\sum_{j=1}^{n} \int_0^\infty \varphi_{r,j}(\boldsymbol{x}) S(r) \mathrm{d}r}. \tag{3.5}$$

This means that one can calculate the numerator and denominator in equations (3.2) and (3.3) separately for each beam and add them up before performing the final division.

Let us now denote the individual LETs of all beam spots by $L_{\mathrm{t},j}(\boldsymbol{x})$ and $L_{\mathrm{d},j}(\boldsymbol{x})$ and their contribution to the total absorbed dose $D(\boldsymbol{x})$ by $D_j(\boldsymbol{x})$. The individual fluences are then given by $\Phi_j(\boldsymbol{x}) = \rho D_j(\boldsymbol{x}) / L_{\mathrm{t},j}(\boldsymbol{x})$ (cf equation (2.3)). Thus one can express the track averaged and dose averaged LET by

$$L_\mathrm{t}(\boldsymbol{x}) = \frac{\displaystyle\sum_{j=1}^{n} L_{\mathrm{t},j}(\boldsymbol{x}) \Phi_j(\boldsymbol{x})}{\displaystyle\sum_{j=1}^{n} \Phi_j(\boldsymbol{x})} = \frac{\rho}{\Phi(\boldsymbol{x})} \sum_{j=1}^{n} D_j(\boldsymbol{x}) \tag{3.6}$$

and

$$L_\mathrm{d}(\boldsymbol{x}) = \frac{\displaystyle\sum_{j=1}^{n} L_{\mathrm{d},j}(\boldsymbol{x}) D_j(\boldsymbol{x})}{\displaystyle\sum_{j=1}^{n} D_j(\boldsymbol{x})} = \frac{1}{D(\boldsymbol{x})} \sum_{j=1}^{n} L_{\mathrm{d},j}(\boldsymbol{x}) D_j(\boldsymbol{x}). \tag{3.7}$$

So for every point $\boldsymbol{x}$ the dose averaged LET is the mean of the individual LETs $L_{\mathrm{d},j}(\boldsymbol{x})$ of all beam spots, weighted by their contributions $D_j(\boldsymbol{x})$ to the total absorbed dose at $\boldsymbol{x}$.

D_1 (Gy)	D_2 (Gy)	$D = D_1 + D_2$ (Gy)	Φ_1 (10^9/cm^2)	Φ_2 (10^9/cm^2)	L_t (keV/μm)	L_d (keV/μm)
1	1	2	0.62	0.042	1.9	8.0
10	1	11	6.2	0.042	1.1	2.3
1	10	11	0.62	0.42	6.6	13.7

Table 3.1: *Comparison of track averaged and dose averaged LETs for mixed irradiation with two different stopping powers ($S_1 = 1$ keV/μm and $S_2 = 15$ keV/μm) for three ratios of the respective doses D_1 and D_2.*

3.1.3 Motivation for the use of the dose averaged LET

In the previous sections, two LETs were introduced: the track averaged and the dose averaged LET. Although both of them are currently in use, the question arises which one of the two should be used in our context, i.e. for the estimation of RBE distributions.

For monoenergetic protons, $L_t(\boldsymbol{x})$ and $L_d(\boldsymbol{x})$ equal each other. Differences occur a) if the local energy spectrum of the protons becomes broader (as it is the case in every realistic proton beam), and b) if the protons at $\boldsymbol{x}$ come from several beam spots with different energies (e.g. for SOBPs or scanning techniques) either from the same direction or from multiple beam angles. We are now looking for a reasonable way to define a mean stopping power or LET that resembles the overall situation at that point. In other words: what is the mean stopping power $\langle S(\boldsymbol{x})\rangle$ so that a dose $D(\boldsymbol{x})$ of monoenergetic protons with $\langle S(\boldsymbol{x})\rangle$ has the same biological effect as the initial set of polyenergetic protons with a total dose of $D(\boldsymbol{x})$?

Let us consider a brief example: a certain voxel of water (density $\rho = 1$ g/cm^3) shall be irradiated by two proton beams with stopping powers of $S_1 = 1$ keV/μm and $S_2 = 15$ keV/μm, respectively. We assume that these values do not change within the voxel. Table 3.1 shows the resulting LETs for three scenarios with different dose weighting. The corresponding fluences $\Phi_1 = \rho D_1/S_1$ (cf equation (2.3)) and Φ_2 as well as the total fluence Φ are also given. Obviously, in all cases L_t and L_d lie between S_1 and S_2. For equal doses ($D_1 = D_2$), one would intuitively expect $\langle S\rangle$ to be more or less in the middle between S_1 and S_2, which is fulfilled by L_d, but not by L_t. For $D_1 = 10 \times D_2$, the situation is dominated by the low LET radiation, so $\langle S\rangle$ should be similar to S_1. This condition is satisfied by both L_t and L_d. In the third case, where $D_2 = 10 \times D_1$, $\langle S\rangle$ should be close to S_2; this is only true for the dose averaged LET (table 3.1). Intuitively, the dose averaged LET therefore seems to be more appropriate for our purpose. This is supported by the fact that the dose (rather than the fluence) is used in radiotherapy as the primary indicator of the biological effect, which makes dose weighting also reasonable for second order effects.

Another more important argument will become apparent in section 4.2.3 when the RBE model is explained, and shall be discussed here only briefly. When the linear-quadratic (LQ) model (Kellerer and Rossi 1978) is applied to mixed irradiations with different LET, it is reasonable to use the dose averaged mean of the α parameter (Zaider and Rossi 1980). In chapter 4, I will express α as a *linear* function of LET, and under that restriction the dose averaged mean of α is equivalent to α calculated as a function of the dose averaged LET.

So in this work, I will concentrate on the dose averaged LET, although I will also provide some formulas for the track averaged LET for the sake of completeness. For the RBE calculations in this work (chapters 4 and 5), only the dose averaged LET is used.

3.2 Methods

I will now derive an algorithm for three-dimensional LET calculations (Wilkens and Oelfke 2004) for realistic treatment plans and patient geometries, i.e. based on computed tomography (CT) data sets. In order to obtain the LET distribution in analogy to dose calculations, we will need i) a model for the LET on the central axis for a single beam spot or Bragg peak in a water phantom (section 3.2.1, see also Wilkens and Oelfke 2003), ii) lateral LET distributions to get off-axis values (section 3.2.2), and iii) a rule for scaling the LET with the radiological depth to account for tissue inhomogeneities (section 3.2.3). The implementation of this algorithm in the treatment planning software *KonRad* is described in section 3.2.4.

3.2.1 LET along the central axis

In this section, I will present an analytical model for the LET distribution along the central axis of proton beams (section 3.2.1.1). After that, I will describe the Monte Carlo simulations that were performed to validate the analytical model (section 3.2.1.2).

3.2.1.1 The analytical LET model

Protons in matter undergo Coulomb interactions (with electrons and nuclei) and nonelastic nuclear interactions, leading to target fragmentation and secondary particles. For the analytical LET model only Coulomb interactions of primary protons as the most frequent interaction process are considered. Especially around the peak and at the distal edge of the Bragg curve, where the largest increase in LET is expected, the absorbed dose is dominated by Coulomb interactions. The dose due to secondary particles can be neglected at or behind the Bragg peak (Paganetti 2002). Nonelastic nuclear interactions occur mostly in the entrance region of the Bragg curve, where the LET is generally low and varies only slightly. However, secondary particles such as alpha particles may have high stopping powers and therefore high LET contributions. Hence they might influence the biological effect (Paganetti 2002), albeit experimental evidence has not yet been firmly established.

Let us now consider a single broad beam of protons in a water phantom. The derivation of a model for the LET along the central axis (Wilkens and Oelfke 2003) can be done in very close analogy to studies presented by Bortfeld (1997), where an analytical approximation for the proton depth dose curve was developed. Let $\varphi_r(z)$ denote the local proton spectrum in residual range r at depth z. To calculate the LET values according to (3.2) and (3.3) we will have to evaluate the following three integrals:

$$\begin{aligned} \Phi_z &:= \int_0^\infty \varphi_r(z)\mathrm{d}r, \\ \langle S\rangle_z &:= \int_0^\infty \varphi_r(z)S(r)\mathrm{d}r \qquad \text{and} \\ \langle S^2\rangle_z &:= \int_0^\infty \varphi_r(z)S^2(r)\mathrm{d}r. \end{aligned} \tag{3.8}$$

The track averaged and dose averaged LET can then be calculated by

$$L_\mathrm{t}(z) = \frac{\langle S\rangle_z}{\Phi_z} \qquad \text{and} \qquad L_\mathrm{d}(z) = \frac{\langle S^2\rangle_z}{\langle S\rangle_z}. \tag{3.9}$$

Before solving these three integrals, we will have a closer look at the spectrum $\varphi_r(z)$ and the stopping power $S(r)$.

Local proton spectra First an expression for the local proton spectrum $\varphi_r(z)$ with respect to residual range r is derived. Let R_0 be the mean initial range of the protons entering the water phantom with a fluence Φ_0 at the phantom surface ($z = 0$). At depth $z \geq 0$, we will assume a Gaussian spectrum with standard deviation $\sigma(z)$ around the mean residual range $R_0 - z$:

$$\varphi_r(z) = \frac{\Phi_0}{\sqrt{2\pi}\sigma(z)}\mathrm{e}^{-(r-(R_0-z))^2/2\sigma^2(z)}. \tag{3.10}$$

The total fluence $\int_0^\infty \varphi_r(z)\mathrm{d}r$ at depth z will be Φ_0 at $z = 0$, $\frac{1}{2}\Phi_0$ at $z = R_0$, and 0 for $z \gg R_0$. There are two contributions to $\sigma(z)$: the range straggling width $\sigma_\mathrm{mono}(z)$ for monoenergetic protons and the machine dependent width of the initial energy spectrum of the incident protons, which is usually not monoenergetic, but has a certain width σ_E. The latter is usually given in MeV but can be translated into a standard deviation of range by using the range-energy relationship.

Although the range straggling width $\sigma_{\text{mono}}(z)$ strongly depends on z, as straggling increases with depth, it is a good approximation to use a constant σ instead of $\sigma(z)$ (Bortfeld 1997). Then (3.10) becomes

$$\varphi_r(z) = \frac{\Phi_0}{\sqrt{2\pi}\sigma} \mathrm{e}^{-(r-R_0+z)^2/2\sigma^2}. \tag{3.11}$$

For σ_{mono}, Bortfeld (1997) derived the expression $0.012 \cdot R_0^{0.935}$, where σ and R_0 are given in cm. To transform σ_E from energy to range, he linearized the range-energy relationship $r = \alpha E^p$ (2.2) around the mean initial energy E_0. This yields

$$\sigma_r = \sigma_E \left.\frac{\mathrm{d}r}{\mathrm{d}E}\right|_{E=E_0} = \sigma_E \alpha p E_0^{p-1} = \sigma_E \alpha^{1/p} p R_0^{1-1/p}. \tag{3.12}$$

The total σ can then be calculated from σ_{mono} and σ_r:

$$\sigma^2 = \sigma_{\text{mono}}^2 + \sigma_r^2. \tag{3.13}$$

A more precise model of the initial energy spectrum would not only consider the main peak but also the so-called tail towards lower energies, which can be found in many treatment machines. This relatively small tail is neglected because the protons of the tail will not reach the depth of R_0 due to their lower energy, i.e. they only affect the entrance region of the Bragg curve, where LET variations are small. However, they will increase the LET in this region slightly without influencing it at or behind the Bragg peak.

Fluence reduction Equation (3.10) does not take into account any absorption of protons. But the proton fluence decreases with increasing depth due to nonelastic nuclear interactions. As one can assume a linear reduction with depth (Lee et al. 1993, Bortfeld 1997), a better approximation for the local proton spectra than (3.10) would be

$$\varphi_r(z) = \frac{\Phi_0}{\sqrt{2\pi}\sigma} \frac{1+\beta r}{1+\beta R_0} \, \mathrm{e}^{-(r-(R_0-z))^2/2\sigma^2}, \tag{3.14}$$

with $\beta = 0.012 \text{ cm}^{-1}$.

The analytical LET calculations can be performed with these improved spectra without extraordinary mathematical effort. However, it turned out that β did not have any relevant

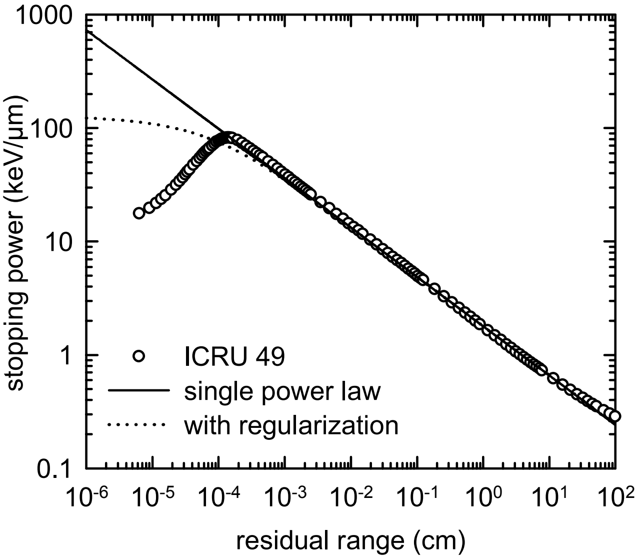

Figure 3.1: *Proton stopping powers in water as a function of residual range. The circles represent the values published in ICRU report 49 (1993). The solid and dotted lines are the basic parametrization by Bortfeld (1997) using a single power law and the result of the regularization with* $R = 2\ \mu m$*, respectively.*

impact on the resulting LET distributions. This can be understood by the mathematical structure of equations (3.2) and (3.3): due to the definitions of LET as a ratio the absolute number of particles is not very important but rather the relative spectra. Although the β terms do not completely cancel mathematically, it is obvious that reducing the number of particles will not affect the LET values much. Therefore β was neglected in all other LET calculations presented in this work.

Stopping power Proton stopping powers were published in ICRU report 49 (1993). The total stopping power due to Coulomb interactions with electrons and with nuclei is plotted in figure 3.1. According to a fit by Bortfeld (1997), a simple power law can be used as an analytical expression for the stopping power:

$$\tilde{S}(r) = \frac{1}{p\alpha^{1/p}} r^{1/p-1}, \tag{3.15}$$

with $p = 1.77$ and $\alpha = 0.0022$ cm·MeV^{-p} (cf section 2.1.1).

This is a good fit for residual ranges between approximately 2 μm and 50 cm (see figure 3.1). Ranges above 50 cm in water are not needed in radiation therapy, but the deviations below 2 μm can become important for LET calculations. As protons with ranges around 2 μm and smaller (corresponding to energies well below 1 MeV) do not contribute much to the absorbed dose, this fit works well for dose calculations. However, such low-energy protons have an impact on the LET calculations, especially due to the singularity of $\tilde{S}(r)$ at $r \to 0$, which has no physical counterpart in reality. To avoid this singularity, the stopping powers for low ranges have to be modeled more precisely. To keep the formula simple and in the mathematical form of power laws, a regularization is performed: $\tilde{S}(r)$ is substituted by $\overline{S}_R(r)$, which is the mean stopping power along the last bit of length R of the path, i.e. the mean of $\tilde{S}$ in the interval $[r, r+R]$:

$$\overline{S}_R(r) = \frac{1}{R}\int_r^{r+R} \tilde{S}(r')\mathrm{d}r' = \frac{1}{R\alpha^{1/p}}\left[(r+R)^{1/p} - r^{1/p}\right]. \tag{3.16}$$

The result for $R = 2$ μm is shown in figure 3.1. The value of R was adjusted by comparing our analytical model to Monte Carlo simulations (see section 3.3.1.2). For $S^2(r)$, which is needed for the calculation of the dose averaged LET, a similar regularization is performed:

$$\overline{S^2_R}(r) = \frac{1}{R}\int_r^{r+R} \tilde{S}^2(r')\mathrm{d}r' = \frac{1}{R\alpha^{2/p}p(2-p)}\left[(r+R)^{2/p-1} - r^{2/p-1}\right]. \tag{3.17}$$

For the following calculations, $\overline{S}_R(r)$ and $\overline{S^2_R}(r)$ are used for $S(r)$ and $S^2(r)$.

Calculation of LET By employing our expressions for $\varphi_r(z)$ and the stopping power in (3.8), a short calculation presented in appendix A leads to the following results:

$$\begin{aligned}
\Phi_z &= \frac{\Phi_0}{\sqrt{2\pi}}\mathrm{e}^{-\zeta^2/4}\mathcal{D}_{-1}(\zeta), \\
\langle S\rangle_z &= \frac{\Phi_0}{\sqrt{2\pi}\sigma R\alpha^{1/p}}\left[\sigma^{1+1/p}\Gamma(1+\tfrac{1}{p})\tilde{\mathcal{D}}_{1+1/p}(\xi,\zeta) - R(\tfrac{1}{2}R)^{1/p}\mathrm{e}^{-(\zeta+\xi)^2/8}\right], \\
\langle S^2\rangle_z &= \frac{\Phi_0}{\sqrt{2\pi}\sigma R\alpha^{2/p}p(2-p)}\left[\sigma^{2/p}\Gamma(\tfrac{2}{p})\tilde{\mathcal{D}}_{2/p}(\xi,\zeta) - 2(\tfrac{1}{2}R)^{2/p}\mathrm{e}^{-(\zeta+\xi)^2/8}\right],
\end{aligned} \tag{3.18}$$

with $\tilde{\mathcal{D}}_\nu(\xi,\zeta) = \mathrm{e}^{-\xi^2/4}\mathcal{D}_{-\nu}(\xi) - \mathrm{e}^{-\zeta^2/4}\mathcal{D}_{-\nu}(\zeta)$ and $\zeta = (z - R_0)/\sigma$, $\xi = (z - R_0 - R)/\sigma$. Here $\Gamma(x)$ is the gamma function and $\mathcal{D}_\nu(x)$ are the parabolic cylinder functions (Gradshteyn and Ryzhik 1994). These functions are tabulated (Abramowitz and Stegun 1972) or can be easily computed by computer programs. The track averaged and dose averaged LET can now be calculated by inserting these results into (3.9). If z, R_0, R and σ are given in cm, L_t and L_d will have units of MeV/cm. Multiplying these values by 0.1 yields units of keV/μm.

Although the introduction of the parabolic cylinder functions seems to be quite elegant from a mathematical point of view, it must be noted that this is certainly not the only way to approach these integrals. They can as well be evaluated numerically, which would allow for even more complicated integrands, as they were no longer restricted to power laws.

The calculations presented above can be performed similarly without the regularization of $\tilde{S}(r)$, i.e. by using $\tilde{S}(r)$ and $\tilde{S}^2(r)$ in (3.8) instead of $\overline{S}_R(r)$ and $\overline{S^2_R}(r)$. For the dose averaged LET, this would yield

$$L_\mathrm{d}(z) = \frac{\sigma^{1/p-1}\Gamma(\frac{2}{p}-1)\mathcal{D}_{1-2/p}(\zeta)}{p\alpha^{1/p}\Gamma(\frac{1}{p})\mathcal{D}_{-1/p}(\zeta)}. \tag{3.19}$$

However, this simplified approach would significantly overestimate the LET (see section 3.3.1.2) and can therefore not be used for LET calculations.

3.2.1.2 Monte Carlo simulations of LET

Although LET and related quantities can be measured by microdosimetric procedures (ICRU 1983, Coutrakon et al. 1997), Monte Carlo simulations are used in this work for the evaluation of the proposed analytical model. They offer a simple way to obtain local energy spectra in a given geometry, which can then be used to calculate LET distributions. The Monte Carlo code GEANT 3.21 (CERN 1994) and the hadron generator FLUKA (Fassò et al. 1993, 1994) are well suited for this problem (Gottschalk et al. 1999, Paganetti and Gottschalk 2003).

A broad beam of protons with a field size of 5×5 cm^2 was simulated in a homogeneous water phantom (20×20×50 cm^3). The initial energy spectrum of the protons was Gaussian with a mean of E_0 and a standard deviation of σ_E. The initial momentum of the protons was perpendicular to the phantom surface. Further studies were performed with different field sizes, even down to an infinitely thin pencil beam.

Electronic and hadronic interactions were considered, and all secondary particles produced in primary and subsequent interactions were tracked. All protons (regardless whether they were primary protons or produced in any nuclear reaction) were scored for the local proton spectra. An important parameter for the Monte Carlo simulations was the cutoff energy for protons, as the low-energy protons have a significant influence on the LET due to their high stopping powers. Especially with a cutoff of 1 MeV, which is sufficient in dose calculation (Szymanowski and Oelfke 2002), the LET is underestimated compared to simulations with lower cutoffs. Several values were tested and it turned out that a reduction of the cutoff energy further than 0.25 MeV did not cause any further changes in the LET. Therefore a cutoff energy of 0.25 MeV was used for the comparison of LET values with the analytical model. To obtain the local energy spectrum at depth z on the central axis of the beam, the energies of all those protons were registered that traversed a plane of 1×1 cm^2 perpendicular to the central axis at depth z. For the pencil beam, this scoring area was reduced to 1×1 mm^2. The resolution of the energy bins was 0.25 MeV.

If $\phi_i(z)$ denotes the number of protons in energy bin i ($i = 1 \ldots N$) and the stopping powers S_i (corresponding to the mean energy of bin i) are taken from ICRU report 49 (1993), the track averaged and dose averaged LET are calculated by

$$L_{\mathrm{t}}^{\mathrm{MC}}(z) = \frac{\sum_{i=1}^{N} \phi_i(z) S_i}{\sum_{i=1}^{N} \phi_i(z)} \quad \text{and} \quad L_{\mathrm{d}}^{\mathrm{MC}}(z) = \frac{\sum_{i=1}^{N} \phi_i(z) S_i^2}{\sum_{i=1}^{N} \phi_i(z) S_i}. \tag{3.20}$$

3.2.2 Lateral LET distributions

In general, the LET increases at the field border because there are more scattered protons that have less energy and therefore higher stopping powers than the protons on the central axis. To quantify this effect, Monte Carlo simulations were done in the same geometry as described in the last section. Now protons were also scored at off-axis positions in a 1 mm grid, and proton spectra were obtained to get lateral LET distributions. This was also done for different field sizes, i.e. for broad beams and for pencil beams. As expected, both the track averaged and the dose averaged LET increased outside of the field with increasing lateral distance to the central axis. These results are shown in section 3.3.2 and in Wilkens and Oelfke (2004).

It was found that this increase is relatively small compared to the steep rise of LET along the central axis. As it was seen in cell survival experiments (e.g. Belli et al. 1993, Wouters et al. 1996), small variations in LET are not expected to affect the RBE significantly. The important effect that has to be considered in treatment planning is certainly the steep rise of LET along the central axis, while the lateral variations might be neglected. Therefore it is a good approximation to use a laterally constant LET, i.e. to assume that the LET in water (L^{w}) at depth z and lateral distance d to the central axis depends only on the depth:

$$L^{\mathrm{w}}(z, d) = L^{\mathrm{w}}_{\mathrm{cax}}(z). \tag{3.21}$$

This approximation can be made for the track averaged as well as for the dose averaged LET, and it makes three-dimensional LET calculations very simple (cf section 3.2.4).

3.2.3 LET in inhomogeneous media

The LET calculations described above are valid for water phantoms only. In the next step we will therefore consider tissue inhomogeneities given by CT data sets. For a single beam, the LET at a given voxel in the CT cube can be obtained from the LET in water by substituting the depth with the water equivalent depth $\eta(z)$, i.e. the radiological path length. The latter is computed by a raytracing algorithm through the CT cube. This requires the relative stopping powers S_{rel} for each voxel, which can be obtained from CT Hounsfield units by appropriate calibration curves (Schneider et al. 1996, Schaffner and Pedroni 1998). Together with (3.21) we then get

$$L(z,d) = L^{\text{w}}_{\text{cax}}(\eta(z)). \tag{3.22}$$

Note that this is still "LET in water" and not "LET in medium", corresponding to the dose which is usually reported as dose to water rather than dose to medium (Liu et al. 2002). However, while dose to water and dose to medium are fairly similar for biological tissues, LET in water and LET in medium can differ significantly. LET in medium can be calculated from $L(z,d)$ by multiplying with S_{rel} for the respective voxel media (as long as S_{rel} is assumed to be independent of the energy).

The greatest deviations between LET in water and LET in medium will be in high density materials, i.e. in bone. But the RBE of protons in bone has not been investigated much yet, and we are primarily interested in more water-like tissues like most tumours and organs at risk. For those tissues, LET in water and LET in medium are more similar. Therefore it is justifiable to use only LET in water, as long as we keep in mind that we underestimate the LET in high density tissues. Consequently, only LET in water will be used throughout this work in analogy to the common practice for the dose.

3.2.4 Integration into *KonRad*

The combination of all aspects mentioned in the sections above yields a fast algorithm for three-dimensional LET calculations, which is very similar to currently implemented finite pencil beam dose calculation algorithms. This LET calculation algorithm was integrated into a research version of the inverse treatment planning tool *KonRad*, which already provided an option for intensity modulated proton therapy (Nill et al. 2000, Nill 2001, Oelfke and Bortfeld 2001). In the following, I will describe how the dose averaged LET is calculated in *KonRad*. The track averaged LET was also implemented in a similar way.

Energy (MeV)	**Range R_0** (cm)	**Initial width σ_E of energy spectrum** (MeV)
160	17.63	0.0
200	26.2	2.0
250	37.9	1.0

Table 3.2: *Parameters for the analytical LET model (range R_0 and width σ_E of the initial energy spectrum) that were used to obtain the LET distributions for three proton energies as input data for KonRad. All calculations were done with the regularization of the stopping power using $R = 2$ μm.*

For the LET calculations, a matrix named L_{ij} is used in analogy to the influence matrix D_{ij} for the dose (see section 2.3.1, and Nill 2001, p 7). The values in the L_{ij} matrix represent the LET that one would see in voxel i if only the j-th beam spot were present. To calculate the entries in the L_{ij} matrix (section 3.2.4.2), look-up tables for the LET are required that correspond to the given depth dose curves for the dose (section 3.2.4.1). The three-dimensional LET distribution (i.e. L_i for every voxel i) can then be obtained from L_{ij} using the weights w_j of all beam spots (and the D_{ij} matrix, see below in section 3.2.4.3).

Finally, the LET cube is written to a file (in analogy to the dose cube files), and a normalization value is given to translate the numbers in the file into units of keV/μm. The LET cube can be further processed as desired, e.g. to get "LET-volume-histograms" (like dose-volume-histograms, cf Webb 1993, pp 17–20).

3.2.4.1 Input data for *KonRad*

The dose calculation in *KonRad* is a finite pencil beam algorithm (Nill 2001, p 30), which uses precalculated depth-dose curves for various proton energies. For every depth-dose curve, a corresponding curve for the LET along the central axis in water ($L^{\mathrm{w}}_{\mathrm{cax}}(z)$) is now read into *KonRad*. In principle, the results for $L^{\mathrm{w}}_{\mathrm{cax}}(z)$ from either the analytical model or Monte Carlo simulations can be used as input data. In the current work, LET distributions computed with the analytical model are used. The respective parameters for the range and the width of the initial energy spectrum are given in table 3.2. They were obtained by fitting the dose from the analytical model (cf Bortfeld 1997) to the existing depth-dose curves in *KonRad*. One has to note that this set of input data does not correspond to any existing proton accelerator in particular. It just resembles a fictitious machine with three energies (160, 200 and 250 MeV) and a continuous range shifter. For each beam spot, *KonRad* chooses the best energy to match the desired range.

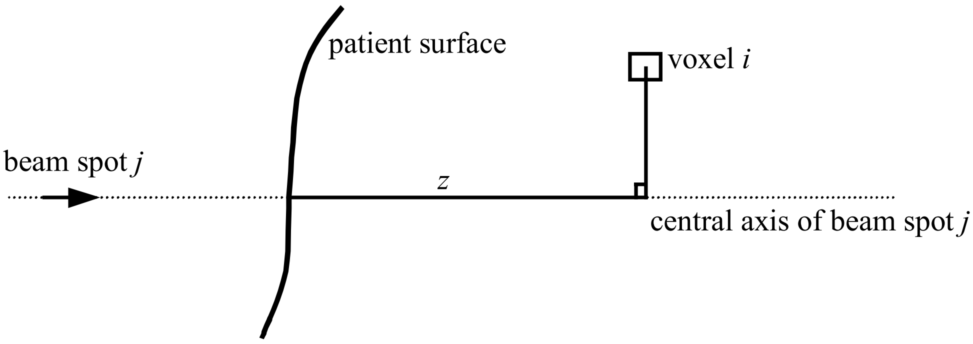

Figure 3.2: *Geometric setup for LET calculations: The LET from beam spot j at voxel i (L_{ij}) is computed using the radiological path length $\eta(z)$ along the central axis of the beam spot j at the geometric depth z.*

3.2.4.2 Calculation of the L_{ij} matrix

The L_{ij} matrix is calculated and stored exactly parallel to the D_{ij} matrix. This saves time, as many computational procedures like the raytracing through the CT cube have to be done only once for both matrices. The following steps must be performed for every voxel i and beam spot j to calculate L_{ij}:

- Calculate D_{ij} as usual (see section 2.3.1, and Nill 2001, p 34). During this process, the radiological path length $\eta(z)$ along the central axis at the geometric depth z is already computed (figure 3.2, cf section 3.2.3).
- If $D_{ij} > 0$, then $L_{ij} = L^{\mathrm{w}}_{\mathrm{cax}}(\eta(z))$. This is done by interpolating the LET values of the input data (section 3.2.4.1) for the energy of beam spot j, taking the range shifter setting for beam spot j into account. This formula is so simple because of the assumption of a laterally constant LET.
- If $D_{ij} = 0$, then $L_{ij} = 0$, i.e. the L_{ij} matrix is only calculated for non-zero D_{ij} elements.

To save memory space, the L_{ij} matrix is stored as a compact matrix $\tilde{L}_{ij}$. The two matrices are connected by

$$L_{ij} = l \cdot \tilde{L}_{ij}, \tag{3.23}$$

where l is a calibration factor, which is set to 0.01 keV/μm. The entries of $\tilde{L}_{ij}$ are stored as two byte variables (range 0–32 767). This corresponds to LET values from 0 to 328 keV/μm with a resolution of 0.01 keV/μm. As the D_{ij} matrix needs six bytes per entry (four for the voxel index and two for a similarly compressed dose value, Nill 2001, p 15), the introduction of the L_{ij} matrix requires only 33% more memory space than the D_{ij} matrix alone. Modern personal computers can easily handle that requirement.

3.2.4.3 Calculation of the three-dimensional LET distribution

Once the weights w_j of the beam spot are established in the optimization process, three-dimensional LET calculations can be made. Let $\mathcal{L}_i$ denote the product of the dose averaged LET (L_i) and the dose (D_i) at voxel i. According to equation (3.7), $\mathcal{L}_i$ can be written as

$$\mathcal{L}_i = \sum_j L_{ij} D_{ij} w_j. \tag{3.24}$$

This sum can be computed easily in the same way as the dose distribution $D_i = \sum_j D_{ij} w_j$ (cf equation (2.4)). Due to the precalculated values of L_{ij} and D_{ij}, this operation can be done very fast, which will be useful when LET calculations are integrated into the optimization loop in chapter 5. There one will often need only the product of LET and dose, which is now easily accessible as $\mathcal{L}_i$. If the actual LET distribution is desired, L_i can be obtained as

$$L_i = \begin{cases} \mathcal{L}_i / D_i & \text{for } D_i > 0, \\ 0 & \text{for } D_i = 0. \end{cases} \tag{3.25}$$

3.3 Results

Now analytical LET distributions for several beam configurations are presented and compared to Monte Carlo simulations, first on the central axis and later also for lateral LET distributions. After that, I will compare three-dimensional LET distributions for spot scanning techniques in IMPT, in particular for the full 3D modulation and for the distal edge tracking (DET).

3.3.1 LET along the central axis

The analytical LET model was compared with the results of the Monte Carlo simulations for a variety of cases, including energies up to 250 MeV. In the following, I will show the results for several exemplary proton energies (mostly 160 MeV and 70 MeV), and the impact of the width of the initial energy spectrum is investigated. Eventually, LET distributions will also be calculated for a spread-out Bragg peak.

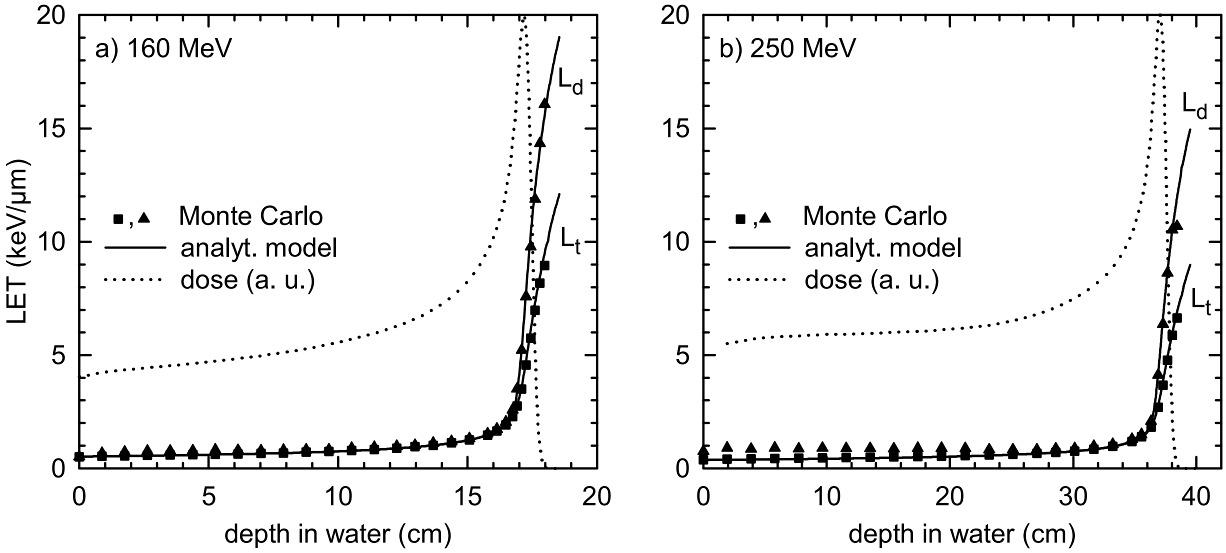

Figure 3.3: *LET distributions for broad beams of 160 MeV (a) and 250 MeV (b) protons in water. Track averaged and dose averaged LET obtained by Monte Carlo simulations (squares and triangles) are compared with the analytical model (lower and upper solid lines, respectively). The relative dose distributions are given in arbitrary units (dotted lines).*

3.3.1.1 LET for high energy beams

First some results for high energy proton beams with initial energies of 160 and 250 MeV are presented, as those are typical values for the treatment of deep seated tumours. Figure 3.3a shows the depth dependence of the track averaged and dose averaged LET along the central axis of a broad proton beam (160 MeV) in a water phantom, both calculated with the analytical model as well as with Monte Carlo simulations (with 3.2×10^7 simulated incident protons). The energy spectrum at the phantom surface was Gaussian with a width of $\sigma_E = 0.5$ MeV around the mean energy of 160 MeV. The Monte Carlo simulations for this energy yielded a mean range (given by the 80% dose at the distal edge) of 17.36 cm, which does not agree exactly with the range of 17.65 cm given in ICRU report 49 (1993). This is due to the fact that GEANT 3.21 uses slightly different stopping powers than those in ICRU report 49 (Szymanowski and Oelfke 2002). To be in accordance with the Monte Carlo simulations, a value of $R_0 = 17.36$ cm was used in the analytical model instead of 17.65 cm. The relative dose distribution obtained by Monte Carlo simulations is given by the dotted line in arbitrary units. In figure 3.3b, the same situation is shown for a 250 MeV proton beam ($R_0 = 37.4$ cm, $\sigma_E = 0.5$ MeV, simulation with 2×10^7 incident protons).

As expected the LET increases very slowly in the entrance region of the beam, but rises steeply at the end of the range. In the entrance region the track averaged and dose averaged LET are almost equal, but at greater depths the dose averaged LET exceeds the track averaged LET considerably. The analytical model agrees well with the Monte Carlo simulations. The maximum deviations were around 0.5 keV/μm.

Let us have a closer look at the entrance region of the 160 MeV beam: In the first 10 cm of depth, where the LETs range between 0.5 and 1.0 keV/μm, the dose averaged LET obtained by the Monte Carlo method was slightly higher than the predictions of the analytical model (up to 0.2 keV/μm). This is due to a high LET contribution from secondary protons produced by nonelastic nuclear interactions, which are included in the Monte Carlo simulations but neglected in the analytical model: by switching off the production of secondary particles in the Monte Carlo code, these differences completely vanished. Consequently, this effect is more pronounced for higher energies (differences up to 0.5 keV/μm were observed for a 250 MeV beam, figure 3.3b), whereas it is reduced for smaller energies (cf section 3.3.1.3).

In figure 3.3 and in all following figures, the Monte Carlo LET is given only at depths where the dose is at least 0.1% of the maximum dose. Further beyond the peak, the number of particles becomes so small that Monte Carlo simulations need an enormous amount of incident protons to yield sufficient statistics. However, in some of the figures one can still see deviations due to poor statistics at the last two or three data points, although the dose is above 0.1% of the peak value. The analytical model is in principle able to calculate LET at any depth, and the analytical LET is therefore plotted up to slightly greater depths than the last Monte Carlo points. For practical purposes this will probably never be needed, as the number of particles at depths far beyond the peak reaches almost zero, and the term LET becomes meaningless for practical applications.

3.3.1.2 Impact of the regularization

The LET distributions in figure 3.3 were calculated with $R = 2\ \mu$m. To illustrate the impact of this parameter in the regularization of $\tilde{S}(r)$ described in section 3.2.1.1 (cf equations (3.16) and (3.17)), dose averaged LET distributions for several values of R are shown in figure 3.4 in comparison to the Monte Carlo simulations with an initial energy of 160 MeV, $R_0 = 17.36$ cm and $\sigma_E = 0.5$ MeV as above.

The dotted line shows the LET one would get without the regularization, i.e. by using $\tilde{S}(r)$ from (3.15) directly for the LET calculations. The derivation of the analytical LET becomes then a bit easier than with the regularization, but leads to similar formulas with different indices of the parabolic cylinder functions (equation (3.19)). However one would significantly overestimate the LET at the distal edge as compared with the Monte Carlo

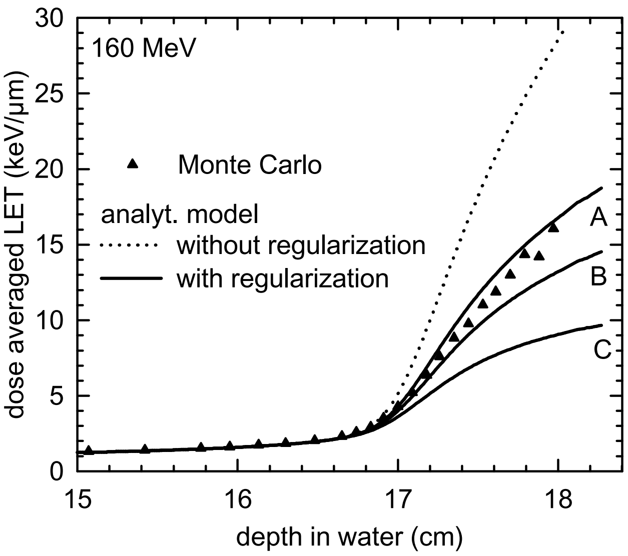

Figure 3.4: *Influence of the parameter R of the regularization of the power law fit for the stopping power: analytical distributions for the dose averaged LET for 160 MeV protons without regularization (dotted line) and with $R = 1$ µm, 10 µm and 100 µm (solid lines A, B and C) in comparison to the Monte Carlo simulations (triangles).*

simulations (figure 3.4), because of the purely mathematical singularity of $\tilde{S}(r)$ at very low residual ranges.

By introducing the regularization, the stopping power is modeled more precisely to correspond to the "real" stopping powers given in ICRU report 49. For increasing values of R the increase in LET at the distal dose edge becomes less and less pronounced. This behaviour is shown in figure 3.4 for $R = 1$ μm, 10 μm and 100 μm. For depths smaller than about 16.5 cm, the regularization does not have any effects on the LET. It turned out that a value of $R = 2$ μm agreed best with the Monte Carlo simulations, both for the dose averaged and for the track averaged LET. Such a "range cutoff" of 2 μm corresponds to a proton energy of 0.13 MeV, which is fairly similar to the Monte Carlo cutoff of 0.25 MeV. Still having in mind that the first fit $\tilde{S}(r)$ agreed with ICRU 49 for residual ranges down to approximately 2 μm (see section 3.2.1.1), the use of $R = 2$ μm seems to be reasonable.

3.3.1.3 LET for low energy beams

In figure 3.5 LET distributions for a proton beam with an initial energy of 70 MeV are shown, which is a typical energy used for the treatment of intraocular tumours. The LET is calculated in water with $R = 2$ μm and $\sigma_E = 0.5$ MeV. R_0 was set to 4.02 cm to fit the mean range of protons in the Monte Carlo simulations, which were done for 2×10^7 incident

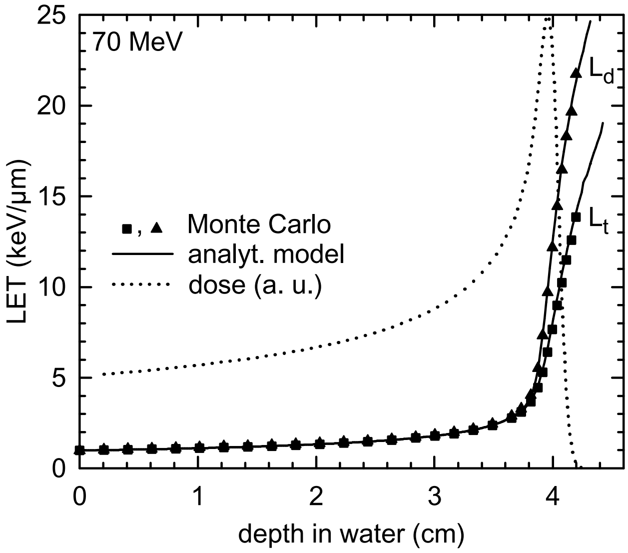

Figure 3.5: *LET distributions for a broad beam of 70 MeV protons in water* ($\sigma_E = 0.5$ *MeV). Track averaged and dose averaged LET obtained by Monte Carlo simulations (squares and triangles) are compared with the analytical model (lower and upper solid line, respectively). The relative dose distribution is given in arbitrary units (dotted line).*

protons in this case. The general behaviour of the LETs is quite similar to the LETs for 160 MeV. However, the absolute LET values at the distal edge are higher compared to the 160 MeV beam. The deviations between the analytical model and the Monte Carlo simulations in the entrance region, which were discussed for 160 MeV, are much smaller for 70 MeV, as secondary protons are less important at lower energies. The maximum deviations were around 0.5 keV/μm at depths greater than 4 cm.

3.3.1.4 Variation of the initial energy spectrum

Next we will investigate the impact of the width σ_E of the initial energy spectrum. We will use the situation of the 70 MeV beam above ($\sigma_E = 0.5$ MeV), and compare it with two other values of σ_E: 0 and 2 MeV. These LET distributions are shown in figure 3.6. Again the relative dose distributions are shown in arbitrary units. As σ_E gets larger, the shape of the Bragg peak becomes broader and the maximum is shifted towards smaller depths. The range, i.e. the 80% dose at the distal edge, was always 4.02 cm. The dose averaged LETs for all three values of σ_E are displayed together in figure 3.7. The LETs are the same at depths smaller than 3 cm and agree well with the Monte Carlo simulations, therefore these depths were not included in figures 3.6 and 3.7. The higher σ_E, the lower the maximum LET values become, and the less steep is its increase at the end of the range. However, the

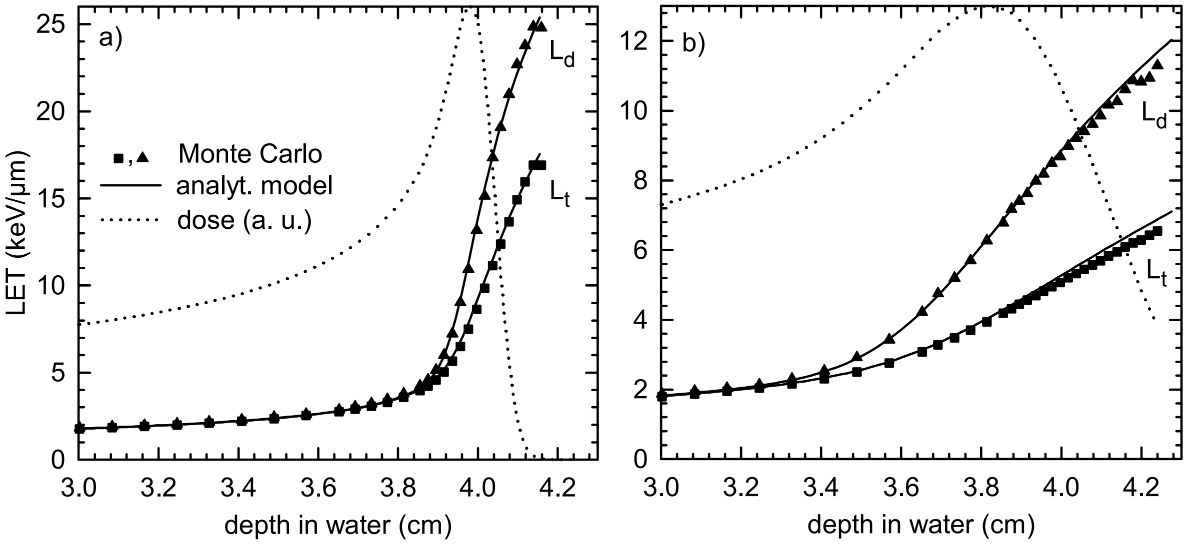

Figure 3.6: *LET distributions for 70 MeV protons in water with $\sigma_E = 0$ MeV (a) and $\sigma_E = 2$ MeV (b). Track averaged and dose averaged LET obtained by Monte Carlo simulations (squares and triangles) are compared with the analytical model (lower and upper solid lines, respectively). The relative dose distributions are given in arbitrary units (dotted lines).*

increase starts earlier, so the region with an LET higher than 5 keV/μm is considerably bigger for $\sigma_E = 2$ MeV than for 0 or 0.5 MeV. Nevertheless the monoenergetic limit $\sigma_E = 0$ can be used to estimate the maximum LET for a given beam energy.

3.3.1.5 LET for a spread-out Bragg peak

As soon as the analytical model was established and validated for a single Bragg peak, it is easy to superimpose several Bragg peaks for more complex situations. In figure 3.8 an example for a 6 cm spread-out Bragg peak (SOBP) is given, which consists of 13 single peaks of 160 MeV that were modulated by a passive range shifter. The positions of the peaks (i.e. the maxima of the dose) are indicated by small vertical lines. The weights of the peaks were obtained by an optimization algorithm presented by Gardey et al. (1999). The dose was computed with the analytical model developed by Bortfeld (1997). The LET distributions for every peak were calculated with the analytical LET model ($R = 2$ μm) and the final LET distributions are obtained according to equations (3.4) and (3.5).

The dose averaged LET is again always greater than the track averaged LET, as it was observed for single beams. At the beginning of the SOBP plateau at around 7 cm depth, there is an increase of the dose averaged LET due to slow protons originating from the Bragg peak at 7.2 cm. On the other hand the track averaged LET does not show

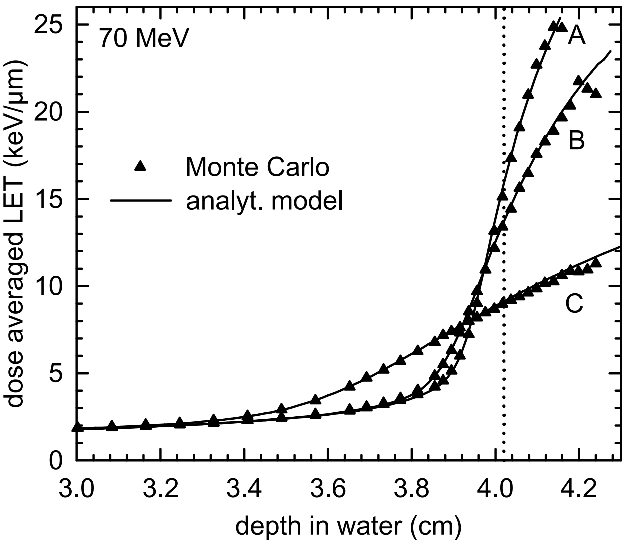

Figure 3.7: *Dose averaged LET calculated with the analytical model (solid lines) in comparison to Monte Carlo simulations (triangles) for 70 MeV beams in water with varying width of the initial energy spectrum (σ_E = 0, 0.5 and 2 MeV for curves A, B and C, respectively). The range (4.02 cm) is indicated by the vertical line.*

a significant increase at the beginning of the plateau. Along the SOBP plateau, both track averaged and dose averaged LET keep increasing, because the fraction of low-energy protons with high stopping powers rises. At the distal edge of the SOBP the LET shows a similar behaviour as for a single peak, because this region is dominated by the protons of the peak at 13.2 cm only.

3.3.1.6 LET dependence on field size

Additional Monte Carlo simulations were performed for different field sizes, and in particular for an infinitely narrow pencil beam. In the Bragg peak region, no significant deviations of the LET on the central axis as a function of the field size were seen. While the track averaged LET did not change in the entrance region either, there were small but systematic differences in the dose averaged LET in that region. Here L_d was slightly lower (within ±0.5 keV/μm) for the pencil beam than for broad beams (cf exemplary data for L_cax in table 3.3). This is again (cf section 3.3.1.1) an effect due to secondary protons. These low energy secondaries are less frequent on the central axis of the pencil beam, because they are scattered away in different directions. In broad beams, this is compensated by secondaries that are scattered onto the central axis from neighbouring parts of the field. Therefore the dose averaged LET on the central axis is slightly higher for broad beams

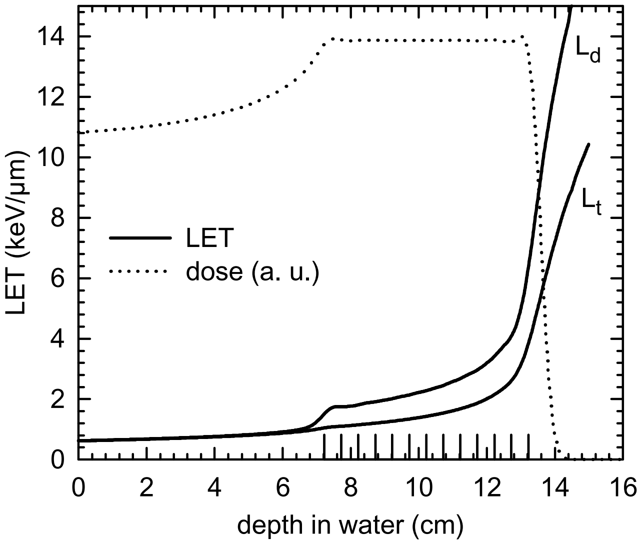

Figure 3.8: *LET distributions for a spread-out Bragg peak, which consists of 13 single peaks. The positions of the peaks are indicated by the small vertical lines. The track averaged and dose averaged LET (lower and upper solid line, respectively) are calculated with the analytical LET model. The dotted line shows the dose distribution in arbitrary units.*

than for the pencil beam. In total, the LET distribution along the central axis was more or less independent of the field size (within ±0.5 keV/μm), even for pencil beams. The analytical LET model can therefore be used for beam spots of any size, i.e. for SOBPs as well as for scanning techniques with narrow beams.

3.3.2 Lateral LET distributions

In further Monte Carlo studies, lateral LET distributions for proton beams with different field sizes in water were obtained. Within the treatment field, a constant LET was observed (figure 3.9). This is in agreement with a study by Paganetti (1998), where no lateral RBE variations within a spread-out Bragg peak field for the treatment of ocular tumours were found (beam energy 68 MeV). The LET increases outside of the field, because there are more scattered and therefore slower protons with higher stopping powers. However, this increase is very moderate in terms of absolute values: table 3.3a gives numbers for the dose averaged LET on the central axis (L_{cax}) and at the lateral positions of 50%, 20% and 5% of the central axis dose (L_{50}, L_{20} and L_5, respectively) for a broad 160 MeV beam (peak position at 17.2 cm depth, beam width 5 cm). The difference between L_5 and L_{cax} was well below 2 keV/μm for all depths. Again, this behaviour was investigated for different field sizes, and no qualitative differences as a function of the field size were found. Even for a

Depth (cm)	a) Broad beam L_{cax}	L_{50} (keV/μm)	L_{20}	L_5	b) Pencil beam L_{cax}	L_{50} (keV/μm)	L_{20}	L_5
5.0	0.8	0.9	1.0	2.1	0.6	0.7	0.7	0.7
10.0	0.9	0.9	1.0	1.2	0.8	0.8	0.8	0.9
17.0	4.3	4.3	4.7	5.9	3.9	4.0	4.1	4.7
17.5	10.7	10.7	11.1	11.3	10.4	10.6	10.9	11.0

Table 3.3: *Lateral values of the dose averaged LET at several depths for a broad beam (a) and a pencil beam (b) of 160 MeV protons, obtained by Monte Carlo simulations (2×10^8 incident protons each). LET values are given for the central axis (L_{cax}) and for the lateral positions of 50%, 20% and 5% of the central axis dose.*

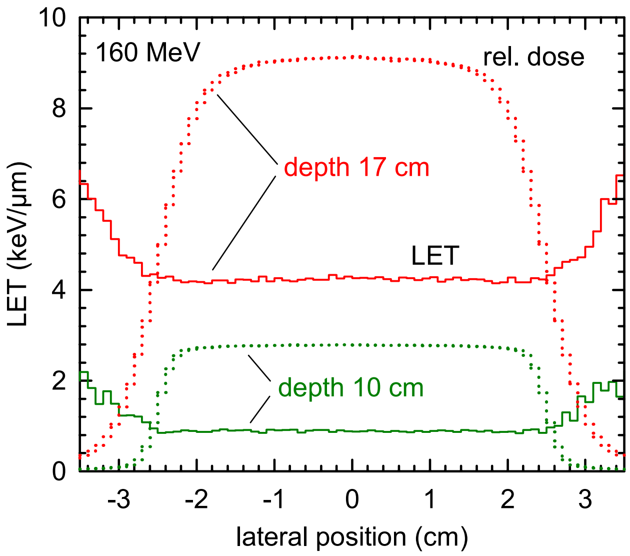

Figure 3.9: *Lateral LET profiles (solid lines) for a broad 160 MeV proton beam of 5 cm width in water. The relative dose profiles (dotted lines) are given in arbitrary units for comparison. Both LET and dose were obtained by Monte Carlo simulations (with 2×10^8 incident protons) and are given for depths of z = 10 cm (green) and z = 17 cm (red) slightly before the Bragg peak at 17.2 cm.*

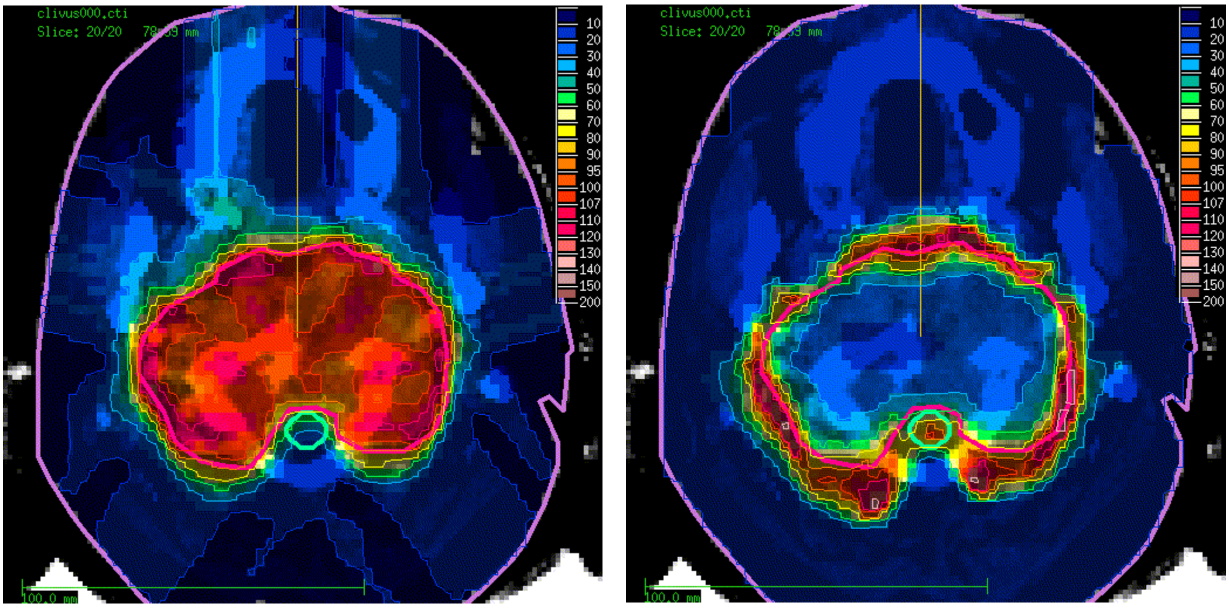

Figure 3.10: *Distributions of dose (left) and LET (right) in a transversal slice through the isocentre for distal edge tracking. The colour scales are normalized to the median PTV dose (100%) and to* $100\% = 5$ *keV/μm, respectively.*

pencil beam (table 3.3b), the increase at the field border was very similar or even smaller than for broad beams. This means that only small errors are introduced if a laterally constant LET is used instead of the "real" lateral LET distributions as seen in the Monte Carlo studies. This justifies the assumption of a laterally constant LET, which was made in section 3.2.2.

3.3.3 Three-dimensional LET distributions

Three-dimensional LET distributions were calculated for a variety of clinical cases and for different dose delivery techniques (Wilkens and Oelfke 2004). Here the focus will be on the comparison of LET distributions for two spot scanning techniques for intensity modulated proton therapy: the 3D modulation, where beam spots are placed over the entire target volume, and distal edge tracking (DET), where only beam spots whose Bragg peak is positioned directly on the distal edge of the target are considered (Lomax 1999). Due to the substantially reduced number of beam spots, the DET technique offers advantages in both computing time and delivery effort compared to the 3D modulation (Nill 2001, Nill et al. 2004).

As an example of the LET calculations, two treatment plans are shown for a patient with a clivus chordoma. The patient geometry and the optimization constraints are described in more detail in chapter 5, where an extensive study on this case including RBE calculations

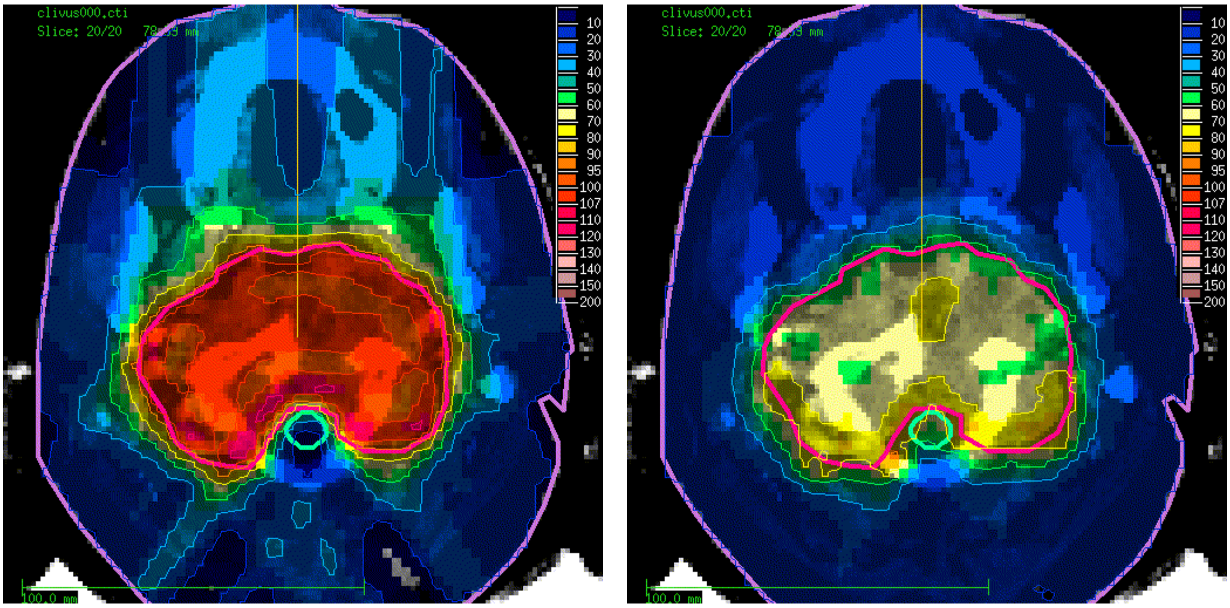

Figure 3.11: *Dose (left) and LET distribution (right) in a transversal slice through the isocentre for the full 3D modulation technique. The colour scales are normalized to the median PTV dose (100%) and to* $100\% = 5$ *keV/μm, respectively.*

is presented. Here, I will just demonstrate the LET algorithm and the differences in LET for the two scanning techniques, i.e. for distal edge tracking (figure 3.10) and for the 3D modulation (figure 3.11). In both cases five coplanar beams were chosen for the treatment of the planning target volume (PTV, thick red line). For every field, beam spots with initial energies up to 200 MeV were placed with a lateral distance of 6 mm. Their individual weights were optimized with the inverse planning tool *KonRad* using its standard quadratic objective function and an iterative gradient method. The objectives were to deliver a homogeneous dose to the PTV, and to spare the brainstem (thick green line) as the most important organ at risk as much as possible. The physical dose distributions (left side in figures 3.10 and 3.11) were very similar for both techniques. The high dose region was highly conformal to the PTV, while the brainstem was mostly spared from dose.

The corresponding distributions of the dose averaged LET are shown on the right sides of figures 3.10 and 3.11 (colour scales normalized to $100\% = 5$ keV/μm). The LET values within the PTV varied considerably for DET, with high LET regions at the border of the PTV. The highest values were even outside of the PTV in the normal tissue. For the 3D modulation technique, a more homogeneous distribution on a higher LET level was found. This is also apparent in the LET-volume-histograms (figure 3.12, in analogy to dose-volume-histograms). The mean LET in the PTV was 2.1 keV/μm for DET and 3.5 keV/μm for the 3D modulation, with a maximum LET in the PTV of 7.3 keV/μm and

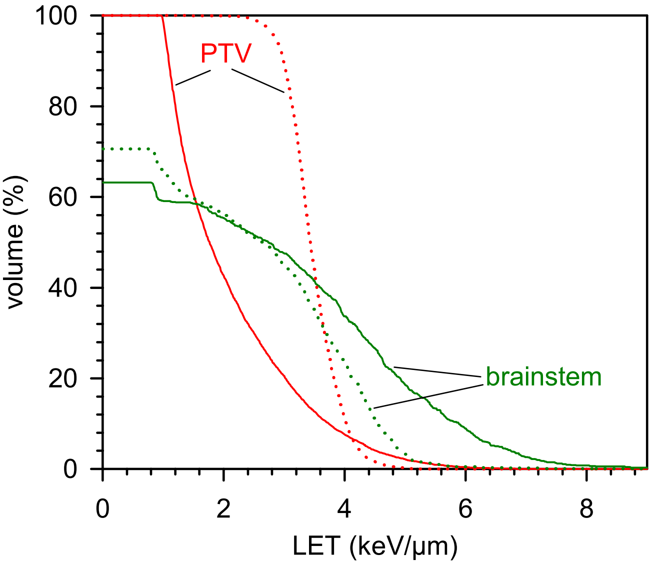

Figure 3.12: *LET-volume-histograms for PTV (red) and brainstem (green) for the two treatment plans shown in figures 3.10 and 3.11, i.e. for the DET technique (solid lines) and for 3D modulation (dotted lines).*

5.1 keV/μm, respectively. The brainstem as the primary organ at risk received substantially higher LET values for DET compared to the 3D modulation (figure 3.12).

3.4 Discussion

3.4.1 LET along the central axis

The presented analytical model for the proton LET along the central axis is able to calculate LET distributions for clinical proton energies, taking range straggling and the machine dependent initial energy spectrum into account. The predictions of the model agree within ±0.5 keV/μm with the Monte Carlo simulations. The main assumptions of the model were thereby justified, particularly the restriction to Coulomb interactions, the neglect of the fluence reduction, and the use of a depth independent σ. The Gaussian approximation of the proton spectra was successful even at depths greater than the CSDA range.

The observed LET distributions showed a slow increase along the entrance region of the beam, and then a very steep increase at the Bragg peak. As expected (ICRU 1970), the dose averaged LET always exceeded the track averaged LET. The absolute LET values at the distal edge were higher for 70 MeV than for 160 MeV, so one would expect a greater effect of this high LET region for the low energy beams, as it was already pointed out by other authors (Paganetti and Schmitz 1996, Skarsgard 1998). The narrower the initial energy spectrum, the higher LET values were observed at the distal edge. However, for broader spectra the increase of LET starts at smaller depths, resulting in an extended region of increased LET.

With the analytical model it was further possible to calculate LET distributions for spread-out Bragg peaks. The LET increases along the SOBP plateau, leading to an increased relative biological effectiveness at the end of the SOBP, which was found in experimental and theoretical studies (Wouters et al. 1996, Paganetti and Schmitz 1996, Biaggi et al. 1999, Paganetti and Goitein 2000). Dose averaged LET distributions for SOBPs were also calculated by Seltzer (1993) using Monte Carlo techniques, giving separate curves for "primary-protons-only" and "primaries-plus-nuclear-secondaries." While the former agreed very well with our LET model as well as with Monte Carlo simulations by Wouters et al. (1996), there were significant differences compared to the latter, namely in the entrance region and in the SOBP plateau, where the total LET including all secondary particles was considerably higher than the LET of primary protons only.

One has to note that the LET distributions presented in this work do not fully account for secondary particles due to nonelastic nuclear interactions. These are completely neglected in the analytical model, and even in the Monte Carlo simulations only secondary protons (which have the highest contribution to the dose of all secondaries) are taken into account. Heavier secondary particles like He ions are not considered, although they can have considerably higher stopping powers than protons. However, these secondaries are most important in the entrance region, where the energy is high enough to produce a significant number of nonelastic nuclear interactions. At or behind the Bragg peak, secondary particles can be neglected (Paganetti 2002). The role of these secondaries in assessing the biological effect is a question of the respective RBE model rather than LET — and for exact RBE calculations alpha particles might have to be included.

Furthermore, the tail of the initial energy spectrum towards low energies was considered neither in the analytical model nor in the Monte Carlo simulations. This might affect the LET in the entrance region as well, but not the LET around the peak, as the protons of the tail have smaller ranges. The LET distributions calculated with the analytical model should therefore correspond well to the reality in the region around the Bragg peak, whereas the LET in the entrance region might be underestimated.

3.4.2 Three-dimensional LET calculations

By combining the analytical model for the LET along the central axis and our studies to lateral LET distributions, a method for fast three-dimensional LET calculations on CT data sets has been developed. It accounts for tissue inhomogeneities and can be applied to state-of-the-art proton dose delivery techniques, as it works for broad beams as well as for thin pencil beams. However, one must be aware that due to the assumption of a laterally constant LET, the LET distributions might be slightly underestimated.

In particular, the LET algorithm was used to compare LET distributions for distal edge tracking (DET) and for the full 3D modulation in intensity modulated proton therapy. While very similar dose distributions can be accomplished with both techniques, considerable differences in the LET distributions were observed. Whereas the 3D modulation yielded more or less homogeneous LET distributions in the PTV, elevated LET values were found at the border of the PTV for DET.

From cell survival experiments it is known that the RBE for protons increases with LET up to an LET value around 30 keV/μm, and decreases for higher LETs (see chapter 4). As the maximum LET values found in our study were around 15 keV/μm, we are in the increasing branch only and can therefore expect elevated RBE values in the high LET regions. For distal edge tracking, this might result in an inhomogeneous biological effect in the PTV as well as in increased damage to organs at risk or normal tissue outside of the PTV. From this point of view, DET seems to be unfavourable compared to the full 3D modulation. However, in chapter 5 optimization methods that compensate this effect will be presented.

At the current point it is still under investigation whether the observed differences in LET are clinically significant, i.e. whether the potential variations in RBE are big enough to be observable in clinical studies. One has to keep in mind that even extreme LET values in normal tissue or organs at risk may be meaningless on the scale of clinical observations, especially if the dose is very low. Moreover, the RBE is certainly not a function of LET alone, but depends as well on other parameters like the dose and the tissue type. Finally it is the product of RBE and dose that matters, so high RBE values might be tolerated well as long as the corresponding dose values are relatively small. With the RBE model that will be described in chapter 4, we can address this question again in chapter 5.

Nevertheless, the choice of the dose delivery technique obviously influences the LET distribution and therefore the expected biological effect. Thus, the physical dose should not be the only criterion for comparing treatment plans or different spot scanning techniques in proton therapy. For this purpose, our algorithm for LET calculations is a useful tool to locate regions of high or low LET, which might in particular help to avoid the exposure of organs at risk to high LET values. The application of three-dimensional LET distributions for fast RBE calculations and even for the optimization of the biological effect will be discussed in the following chapters.

Chapter 4

The Phenomenological RBE Model

4.1 Introduction

While the physical properties of therapeutic proton beams are well known (cf chapter 2), there are still some unsolved questions regarding the biological effect of protons, which is often expressed in terms of the so-called relative biological effectiveness (RBE). Today, most clinical centres use a constant RBE of 1.1 although there is experimental evidence that the RBE is not constant, but depends on dose and on the radiation quality, i.e. the local proton energy distribution. This is very obvious for *in vitro* experiments with cell cultures (e.g. Belli et al. 1993, Wouters et al. 1996, Skarsgard 1998). On the other hand, the observed RBE variations for *in vivo* systems are much smaller, and in most cases a constant RBE of 1.1 seems to be clinically acceptable (Paganetti et al. 2002). But even *in vivo* there is an increase in RBE at the end of the proton range (Gueulette et al. 2001) that should be accounted for in treatment planning (Paganetti et al. 2002).

In this thesis, the potential clinical impact of a variable RBE for different treatment techniques in intensity modulated proton therapy is investigated. This requires a reliable RBE model that is simple enough to allow very fast calculations of three-dimensional RBE distributions. Especially for the integration of the RBE model into the optimization loop, the calculation speed becomes a very important issue. Existing RBE models based on track structure theory (Butts and Katz 1967, Katz et al. 1971, Scholz and Kraft 1994, Scholz et al. 1997, Paganetti and Goitein 2001) are quite elaborate and need long computing times, which renders them not particularly well suited for inverse planning. The aim of this work is therefore to develop a simple and fast method for approximative RBE calculations, which can still reproduce the basic effects of a variable RBE as observed in radiobiological experiments.

It is not our goal to design a new mechanistic theory of RBE, since such theories can still only be a crude approximation to the whole complexity of the radiobiological effects of ionizing radiation. At the current point, we therefore see our only chance in using a phenomenological model based on experimental results, mainly from *in vitro* studies with cell cultures. Thus we propose a simplified RBE model based on the linear-quadratic model, which describes the RBE as a function of dose, linear energy transfer (LET) and phenomenological tissue parameters. In its current form, the model is intended only for protons and not for heavier charged particles. For the latter, the radiobiology becomes more complex and it will thus be more difficult to find a simple phenomenological approach (see chapter 6).

In this work I will concentrate — as an example — on *in vitro* experiments for V79 Chinese hamster fibroblasts, as there are many data available in the literature for this cell line. After the presentation of the RBE model (section 4.2), RBE values obtained with the new model will be compared to published results (section 4.3) and implications for the shape of spread-out Bragg peaks (SOBPs) will be discussed.

4.2 Methods

The most important dependencies of the RBE of proton beams are those on depth, dose and tissue type or cell line, which have been investigated experimentally and theoretically by many authors (e.g. Hall et al. 1978, Bettega et al. 1979, Blomquist et al. 1993, Wouters et al. 1996, Denekamp et al. 1997, Tang et al. 1997, Paganetti 1998, Gerweck and Kozin 1999, Kraft 2000). For the dependence on depth it is of course not the depth itself that matters, but rather the energy or the energy spectrum of the protons, which changes with depth. This is often described with the term "radiation quality" and quantified by the linear energy transfer (LET). Accordingly, the LET will be used in addition to the dose to characterize the radiation field. Methods for three-dimensional calculations of the dose averaged LET were already presented in chapter 3. Goodhead et al. (1992) showed that in general the radiation quality cannot be described by the LET alone, as they found different RBE values for protons and alpha particles with the same LET. However, since we consider only protons, the LET concept can be used for our purpose. While the dose dependency of RBE is clearly seen *in vitro* (e.g. Hall et al. 1978, Wouters et al. 1996), it seems to be less pronounced *in vivo* (e.g. Tepper et al. 1977, Gueulette et al. 2001). Among other reasons, this might be due to the fact that most *in vivo* studies were done at low LET (e.g. in the entrance region or in mid SOBP), whereas the greatest effects of the dose dependency (and of a variable RBE in general) can be expected for higher LET values, i.e.

in the distal dose falloff. The RBE further depends on the choice of the reference radiation (section 4.2.2.3) and on the biological endpoint (e.g. cell survival). Therefore the endpoint needs to be specified when tissue specific parameters for the RBE model are derived.

4.2.1 The relevant LET range in proton therapy

A brief overview over LET definitions and methods for three-dimensional LET calculations were given in chapter 3. Since the RBE model has to cover only therapeutically relevant LET values, this range in LET will now be specified. Protons of 250 MeV (the highest energy used in therapy) have a stopping power of 0.39 keV/μm, and for decreasing energy the stopping power rises to a maximum of 83 keV/μm at 0.08 MeV, before it drops down again (ICRU 1993). However, in therapeutic beams one will rarely find voxels exposed to monoenergetic protons of 0.08 MeV only, as range straggling broadens the spectrum even for initially monoenergetic beams. For $E_0 = 70$ MeV and $\sigma_{\mathrm{E}} = 0$, data in figure 3.7 show that the dose averaged LET does not exceed 30 keV/μm, at least for those depths where the dose is above 0.1% of the maximum dose. And this is even an extreme case: the LET values at the distal edge decrease for higher initial energies (due to increased range straggling), as well as for greater values of σ_{E} (cf section 3.3). Of course there are single protons with higher stopping powers, but they do not contribute much to the dose averaged LET. Since a laterally constant LET is assumed (cf section 3.2.2), the off-axis LET values will not be higher than on the central axis. For therapeutic proton fields with initial beam energies between ~70–250 MeV, we can safely restrict our RBE model to dose averaged LETs in the range 0.3–30 keV/μm.

4.2.2 The phenomenological RBE model

The biological response to radiation is often described by the linear-quadratic (LQ) model (Kellerer and Rossi 1978), which characterizes the biological system by two parameters α and β. The surviving fraction SF of cells at a certain dose D is then given by

$$SF = \exp(-\alpha D - \beta D^2). \tag{4.1}$$

There are other models as well, but in many cases the LQ model reproduces the experimental results fairly well. It is therefore reasonable to use the LQ model, at least in a phenomenological rather than in a mechanistic way. Let us now consider two survival curves as a function of dose for the same biological system, but for two different radiations: a reference radiation with parameters α_{x} and β_{x}, and a proton beam with α_{p} and β_{p}. The

RBE can then be calculated easily, as RBE is just defined as the ratio of the doses required to yield the same survival level. The RBE at a certain proton dose D_p is then given by

$$\mathrm{RBE}(D_\mathrm{p}, \alpha_\mathrm{x}, \beta_\mathrm{x}, \alpha_\mathrm{p}, \beta_\mathrm{p}) = \frac{\sqrt{\alpha_\mathrm{x}^2 + 4\beta_\mathrm{x} D_\mathrm{p}(\alpha_\mathrm{p} + \beta_\mathrm{p} D_\mathrm{p})} - \alpha_\mathrm{x}}{2\beta_\mathrm{x} D_\mathrm{p}}. \tag{4.2}$$

In the limits of very low and very high doses, this can be simplified to

$$\lim_{D_\mathrm{p}\to 0} \mathrm{RBE}(D_\mathrm{p}, \alpha_\mathrm{x}, \beta_\mathrm{x}, \alpha_\mathrm{p}, \beta_\mathrm{p}) = \frac{\alpha_\mathrm{p}}{\alpha_\mathrm{x}} \quad \text{and} \quad \lim_{D_\mathrm{p}\to \infty} \mathrm{RBE}(D_\mathrm{p}, \alpha_\mathrm{x}, \beta_\mathrm{x}, \alpha_\mathrm{p}, \beta_\mathrm{p}) = \sqrt{\frac{\beta_\mathrm{p}}{\beta_\mathrm{x}}}. \tag{4.3}$$

Of course one can also express the RBE as a function of the reference dose D_x or the corresponding biological effect (i.e. SF) instead of the proton dose D_p. These formulas are all equivalent and can be used as desired. Similar expressions were also presented by other authors (e.g. Joiner and Field 1988, Hawkins 1998, Dale and Jones 1999). The RBE in (4.2) depends on dose, which has to be the dose per fraction in a multifraction regime. The tissue and endpoint dependence is determined by the α and β parameters for the reference radiation and for protons. However, the values of α_p and β_p are not fixed, but they depend on the radiation quality or LET of the respective proton beam. This was investigated in many experiments, so we can now look at the dependencies of α_p and β_p on LET.

4.2.2.1 The dependence of α_p on LET

Figure 4.1 shows data for α_p as a function of the dose averaged LET for the survival of V79 Chinese hamster cells *in vitro* from many different experiments with protons. Up to ~30 keV/μm, α_p increases with LET, and decreases for higher LETs. But as LET values above 30 keV/μm are not needed for practical purposes in clinical proton therapy (cf section 4.2.1), we can concentrate on the low LET region and assume a linear dependence of α_p on the LET L:

$$\alpha_\mathrm{p}(L) = \alpha_0 + \lambda L. \tag{4.4}$$

Fur further simplification, one could even set $\alpha_0 := \alpha_\mathrm{x}$, although we do not employ this restriction at this point. Unfortunately, there are no studies in the low LET region below ~3 keV/μm that report both α_p and the LET at the point of the measurement. The best fit to the data for V79 cells was obtained for $\alpha_0 = 0.1$ Gy^{-1} and $\lambda = 0.02$ μm keV^{-1} Gy^{-1}.

If — for any reason — the LET region above 30 keV/μm also had to be modeled, one solution could be to use the linear function below the maximum at L_max, and a $1/L$ de-

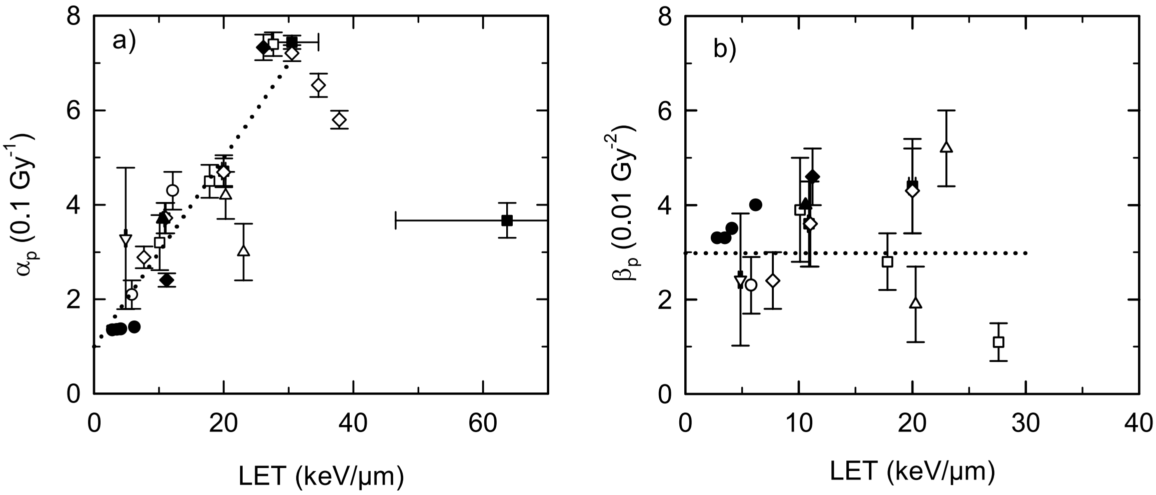

Figure 4.1: *Experimental results for the LQ parameters* α_p *and* β_p *as a function of LET for the survival of V79 Chinese hamster cells in vitro: (a)* α_p *vs. LET, (b)* β_p *vs. LET (○ Perris et al. 1986; △ Goodhead et al. 1992; ▽ Blomquist et al. 1993; ■ Belli et al. 1993; □ Folkard et al. 1996; ● Wouters et al. 1996; ▲ Waheed et al. 1997; ◇ Belli et al. 1998; ◆ Schettino et al. 2001). Error bars in LET are included as far as they were reported. In (a), a linear fit according to equation (4.4) with* $\alpha_0 = 0.1$ *Gy*$^{-1}$ *and* $\lambda = 0.02$ *µm keV*$^{-1}$ *Gy*$^{-1}$ *was added, while the dotted line in (b) corresponds to a constant* β_p *according to equation (4.6) using* $\beta_\mathrm{x} = 0.0298$ *Gy*$^{-2}$ *(Tilly et al. 1999).*

pendence above L_max, corresponding to a constant value of the "inactivation cross section" $\alpha_\mathrm{p}(L) \times L$:

$$\alpha_\mathrm{p}(L) = \begin{cases} \alpha_0 + \lambda L & \text{for } L \le L_\mathrm{max}, \\ (\alpha_0 + \lambda L_\mathrm{max}) L_\mathrm{max}/L & \text{for } L > L_\mathrm{max}. \end{cases} \tag{4.5}$$

Hawkins (1998) also suggested a linear dependence like in (4.4), and found good agreement with experimental data for several cell lines in the LET region below 50 keV/μm (Hawkins 2003). Tilly et al. (2002) used a similar expression for tissues with $\alpha_\mathrm{x}/\beta_\mathrm{x}$ below 5 Gy, and an exponential dependence of α_p on LET for higher $\alpha_\mathrm{x}/\beta_\mathrm{x}$. A linear dependence on LET was also predicted and discussed by Neary (1965) and Schmid et al. (1997) for chromosome aberrations. Tang et al. (1997) reported an increasing α_p with depth and therefore with LET for the survival of CHO cells in a 65 MeV SOBP. Chapman et al. (1977) also saw an increasing α_p with LET for V79 cells under irradiation with heavier ions (He, C, Ne, Ar).

4.2.2.2 The dependence of β_p on LET

The LET dependence of β_p (figure 4.1b) is not as clear as the situation for α_p. While Belli et al. (1998) found an increasing β_p for LET from 7.7 to 20 keV/μm, Folkard et al.

(1996) reported decreasing values. Also for other experimental situations, many different opinions on this question can be found in the literature: Courdi et al. (1994) saw an increasing β_p with LET for human melanoma cells, and Chapman et al. (1977) reported a slightly increasing β_p for increasing LET with heavy ions. Barendsen performed extensive studies on the LET dependence of the LQ parameters (1994, 1997) and finally suggested a value of approximately 1.5–2.0$\times\beta_\mathrm{x}$ for β_p at high LET (2000). On the other hand, Tang et al. (1997) did not see an increase of β_p with LET in their study, and a constant β_p is frequently discussed (Neary 1965, ICRP 1989, Hawkins 1998, Dale and Jones 1999, Jones and Dale 2003). Tilly et al. (2002) used a constant β_p for $L \leq 20$ keV/μm, and a linear decrease for higher LETs. No significant variations in β_p at $L \leq 6$ keV/μm were observed for chromosome aberrations (Schmid et al. 1997).

Unfortunately, there are not much data for β_p at high LET values (above ~20 keV/μm). This is because the measured survival data at these LET values usually do not show a distinct shoulder, so many authors fitted the survival data just to a pure exponential curve ($\exp(-\alpha D)$). However, this does not necessarily mean that β_p is zero. At these high LET values, where α_p is large, one would need to go to very high doses (even above 10 Gy) to determine a small β_p component accurately. But at these doses, the number of surviving cells becomes very small, which makes measurements of β_p at high LET extremely difficult.

But this also means that β_p has not much influence at high LET, especially at therapeutic levels for the dose per fraction (well below 10 Gy), where the variations in α_p are much more important. We therefore think that it is justified to use a constant β_p, which for simplicity shall be the β_x of the reference radiation, i.e.

$$\beta_\mathrm{p}(L) := \beta_\mathrm{x}. \tag{4.6}$$

At least at low LET, this seems to be in agreement with the data in figure 4.1.

By inserting equations (4.4) and (4.6) into (4.2) we finally get

$$\mathrm{RBE}(D_\mathrm{p}, L, \alpha_0, \lambda, \alpha_\mathrm{x}, \beta_\mathrm{x}) = \frac{\sqrt{\alpha_\mathrm{x}^2 + 4\beta_\mathrm{x} D_\mathrm{p}(\alpha_0 + \lambda L + \beta_\mathrm{x} D_\mathrm{p})} - \alpha_\mathrm{x}}{2\beta_\mathrm{x} D_\mathrm{p}}. \tag{4.7}$$

Again, similar formulas can be obtained for RBE as a function of D_x or of the biological effect rather than D_p. In particular, the RBE for a given surviving fraction SF is

$$\mathrm{RBE}(SF, L, \alpha_0, \lambda, \alpha_\mathrm{x}, \beta_\mathrm{x}) = \frac{\sqrt{\alpha_\mathrm{x}^2 - 4\beta_\mathrm{x} \ln SF} - \alpha_\mathrm{x}}{\sqrt{(\alpha_0 + \lambda L)^2 - 4\beta_\mathrm{x} \ln SF} - \alpha_0 - \lambda L}. \tag{4.8}$$

4.2.2.3 Reference radiation

The RBE obviously depends on the choice of the reference radiation. Cell experiments for the determination of RBE values were mostly done either with 200 or 250 kVp X-rays, or with ^{60}Co gamma-rays as reference. In the following, I will give all RBE values relative to ^{60}Co gamma-rays, since they are similar to high energy photons from clinical linear accelerators, which are commonly used in conventional radiation therapy. For V79 cells, we will therefore use $\alpha_\mathrm{x} = 0.112$ Gy^{-1} and $\beta_\mathrm{x} = 0.0298$ Gy^{-2} (Tilly et al. 1999). However, one must be aware that errors in α_x and β_x lead to considerable uncertainties in the RBE values, although the biological effect in terms of the surviving fraction SF in a proton beam is determined by α_0, λ, β_p, D and L only.

4.2.3 Mixed LET irradiations

Most of the data in figure 4.1 are for monoenergetic protons (apart from Blomquist et al. 1993 and Wouters et al. 1996). However, in clinical practice of proton therapy, one will almost always find polyenergetic beams (as in SOBPs) and/or the superposition of different beam spots from different directions. This makes mixed irradiation experiments very interesting in this context. Tilly et al. (1999) compared several cell survival models for a mixed LET experiment with V79 cells irradiated with nitrogen ions and ^{60}Co gamma-rays. They found that the track structure model (Katz et al. 1971), the microdosimetric (LQ) model (Kellerer and Rossi 1978, Zaider and Rossi 1980) and the lesion additivity model (Lam 1987) could all predict the experimental results within the uncertainties of the measurement. The approach of Zaider and Rossi (1980) was also used by Belli et al. (1997) for protons and was successfully applied to carbon beams (e.g. Kanai et al. 1997, Schaffner et al. 2000). It describes the effect of two (or more) irradiations with different LET by "dose averaged" means of the respective α and $\sqrt{\beta}$ values. In the region below 30 keV/μm, this is equivalent to our model, where the total α_p is calculated as a linear function of the dose averaged LET. This indicates that mixed irradiation effects for protons of different LET are reasonably modeled in our approach.

4.3 Results

4.3.1 Comparison with experimental RBE values

In figure 4.2, RBE values for the survival of V79 cells calculated with our model are compared to experimental data from the literature (Blomquist et al. 1993, Folkard et al. 1996,

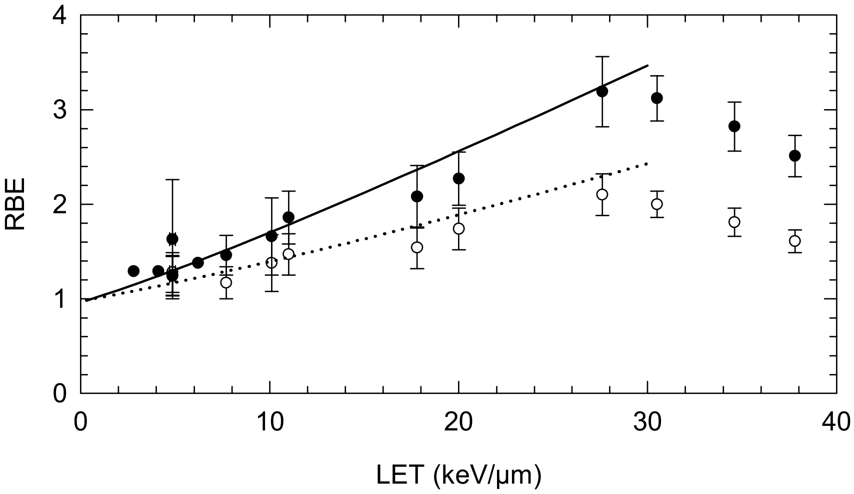

Figure 4.2: *RBE values (relative to ^{60}Co) for the survival of V79 cells, irradiated with protons of different LET. The experimental data for two survival levels (○ 10%, ● 50%) are from Blomquist et al. (1993), Folkard et al. (1996), Wouters et al. (1996) and Belli et al. (1998). RBE values that were reported relative to 200 kVp (Belli et al. 1998) or 240 kVp X-rays (Folkard et al. 1996) were corrected to ^{60}Co by applying a dose independent factor of 1.1 (Spadinger and Palcic 1992). The RBE values from equation (4.8) for the 10% and 50% survival level are given by the dotted and solid lines, respectively.*

Wouters et al. 1996, Belli et al. 1998) for two survival levels (10% and 50%), corresponding to doses of 7.1 and 3.3 Gy ^{60}Co gamma-rays. For the phenomenological RBE model, the values for α_{x}, β_{x}, α_0 and λ that were given in the previous section were employed. The experimental data are either as stated in the original publications, or they were derived from the α and β values for protons and the reference radiation given in the respective papers. Where no error bars for the RBE were reported, they were calculated from the errors in α and β, as far as those were given. For LETs below 30 keV/μm, the RBE increases with LET for a given survival level. Independently of LET, the RBE is higher for higher survival levels, i.e. for lower doses.

4.3.2 Application of the RBE model to SOBPs

The RBE model was applied to two SOBPs with maximum energies of 70 MeV and 160 MeV (figure 4.3). Both SOBPs consisted of 15 weighted pristine peaks that were shifted by different thicknesses of absorbing material. The pristine peaks had an initial energy spread σ_{E} of 0.5 MeV in both cases. The ranges were 4.02 cm (70 MeV) and 17.6 cm (160 MeV), and the modulation widths (measured between the 90% dose levels) were 2.2 cm and 7.8 cm, respectively. The physical dose distributions along the central axis (with 2 Gy

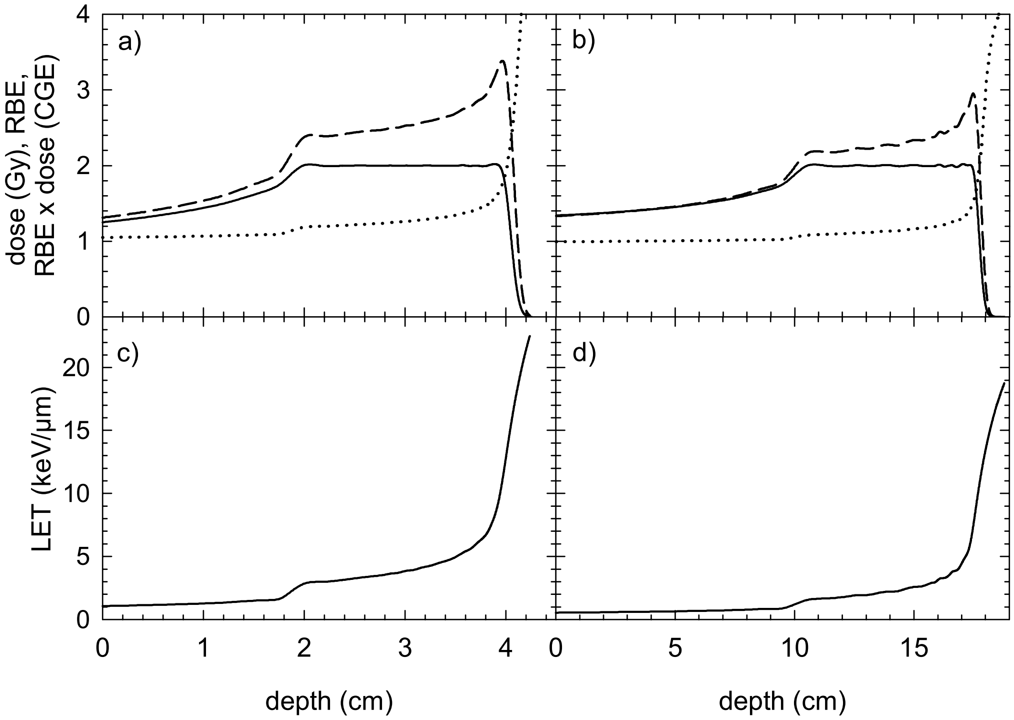

Figure 4.3: *(a): Dose (——), RBE (······) and RBE× dose (– – –) for a SOBP with a maximum energy of 70 MeV (range 4.02 cm), with the corresponding LET in (c). In panels (b) and (d) on the right, the same distributions are given for a 160 MeV SOBP with a range of 17.6 cm. RBE values (relative to ^{60}Co) are for the survival of V79 cells and were calculated with the RBE model described in section 4.2.2.*

in the SOBP) are shown in figure 4.3a and b, and the corresponding distributions of the dose averaged LET in figure 4.3c and d. The LET is low in the entrance region, rises along the SOBP plateau and increases very steeply at the distal edge. In the 160 MeV beam, the LET values are lower than for the 70 MeV beam. This is due to the lower stopping power at high energies in the entrance region, and to increased range straggling in the SOBP region, which broadens the energy spectrum of the beam, leading to lower values of the dose averaged LET (cf chapter 3). At every depth, the RBE for the survival of V79 cells relative to ^{60}Co was calculated according to equation (4.7), using the actual dose and LET values and the cell parameters (α_0, λ, α_x and β_x) given in section 4.2.2. The RBE and the product of RBE and dose are shown in figure 4.3a and b for both SOBPs. For RBE × dose, units of "Cobalt Gray Equivalent" (CGE) were used to indicate that it is a proton dose which has already been multiplied by the RBE relative to ^{60}Co. The RBE starts around 1 at the beam entrance, increases slowly along the SOBP, and shows a steep increase at the distal edge. This means that RBE × dose is not flat in the SOBP plateau, but it is

SOBP dose (Gy)	70 MeV			160 MeV		
	RBE proximal	RBE distal	Distal shift (mm)	RBE proximal	RBE distal	Distal shift (mm)
1	1.24±0.14	1.93±0.18	0.90±0.06	1.11±0.13	1.60±0.16	2.2±0.2
2	1.18±0.10	1.75±0.13	0.83±0.06	1.08±0.10	1.44±0.11	1.9±0.2
4	1.12±0.07	1.46±0.09	0.70±0.07	1.05±0.06	1.29±0.08	1.6±0.2
8	1.07±0.04	1.28±0.06	0.53±0.06	1.03±0.04	1.18±0.05	1.1±0.2

Table 4.1: *RBE values (survival of V79 cells relative to ^{60}Co) at the proximal and distal edge of the SOBPs shown in figure 4.3 for several dose levels of the SOBP plateau. The resulting shift in depth of the distal edge between the physical dose and RBE × dose is also given (evaluated at 80% of the physical dose). The error intervals account for uncertainties in the parameters α_0 and λ.*

inclined and shows a clear region of increased effectiveness at the distal edge. Moreover, the "high dose" region of RBE × dose is extended to slightly greater depths compared to the physical dose.

The main features of the RBE × dose curve, i.e. the incline of the SOBP and the shift of the distal edge, were further evaluated for several dose levels (table 4.1). For doses of 1, 2, 4 and 8 Gy, RBE values are given at the proximal and distal edge of the SOBP (at depths of 1.98 and 3.94 cm for the 70 MeV beam and at 10.5 and 17.4 cm for 160 MeV). For both energies, the RBE values decrease with increasing dose, and the values at the distal edge are higher than at the proximal edge. Due to the higher LET values in the low energy beam, the RBE values are generally higher in that case.

Table 4.1 also quantifies the extension of the high dose region to greater depths, i.e. the shift of the distal edge of RBE × dose compared to the physical dose. The reported values are the distance between the two curves measured at the 80% level of the physical dose given to the SOBP plateau. A constant RBE of 1.1 would result in a dose independent shift of 0.13 mm (70 MeV) and 0.39 mm (160 MeV) and would clearly underestimate the values from table 4.1. The effect becomes smaller for greater doses, as the RBE values decrease with dose. For the 160 MeV case, the absolute values of the shift are more than twice as high as for the 70 MeV beam, despite of the lower LET and RBE values in the high energy beam. This is due to the fact that the distal falloff of the physical dose is much shallower in the 160 MeV beam: the distance between the 80% and 20% levels of the physical dose in the SOBP is 0.98 mm for the 70 MeV beam compared to 2.9 mm in the 160 MeV beam, which is due to increased range straggling in the latter case.

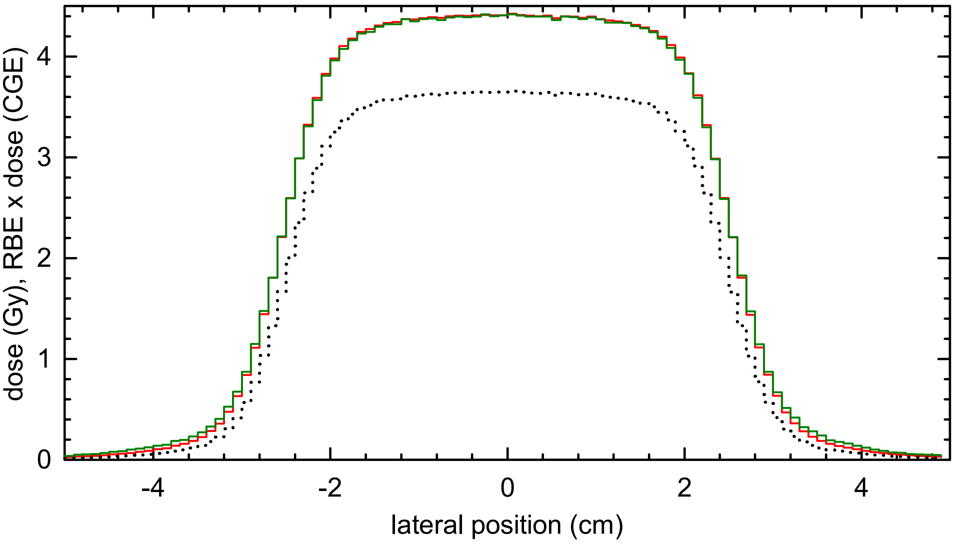

Figure 4.4: *Lateral profiles of RBE × dose for a broad 160 MeV proton beam of 5 cm width at a depth of 17 cm (slightly before the peak at 17.2 cm). The RBE was calculated using a laterally constant LET (red solid line) as well as using the lateral LET distribution obtained by Monte Carlo simulations (green), cf figure 3.9. The physical dose is given by the dotted line.*

To estimate the effects of uncertainties in the tissue parameters, potential errors in α_0 (± 0.02 Gy^{-1}) and λ (± 0.002 μm keV^{-1} Gy^{-1}) were derived from the data in figure 4.1. The consequences of these errors in a worst case scenario are given in table 4.1. However, we did not take any possible errors in dose, LET, α_x and β_x into account, so the real error will be even larger.

4.3.3 Three-dimensional RBE calculations

The phenomenological RBE model described above can be applied to any point in a radiation field as long as the dose, the dose averaged LET and the relevant tissue parameters for that point (or voxel) are known. Since three-dimensional distributions of dose and LET can be calculated (cf section 3.3.3), RBE and RBE × dose can also be obtained in three dimensions. Such distributions will be shown and discussed for realistic planning studies in the next chapter.

Here, I will just present an example of lateral profiles for RBE × dose in order to test the assumption of a laterally constant LET made in section 3.2.2. For a broad beam of 160 MeV (same configuration as described in section 3.3.2, with a peak dose of 4 Gy), lateral distributions of dose and RBE × dose are given in figure 4.4. The RBE was calculated in two ways, using i) a laterally constant LET and ii) the lateral LET values obtained by

Monte Carlo simulations (as shown in figure 3.9). When comparing RBE × dose for the two methods, only small differences can be seen. The greatest deviations are found in the low dose region far away from the central axis, where the biological effect is slightly underestimated when using the constant LET. However, the RBE values at doses below 1 Gy have to be considered with great care since the LQ model might not be valid in that dose region (see discussion below).

4.4 Discussion

RBE values as a function of the LET were calculated with our model and compared to experimental results (figure 4.2). In the LET region below 30 keV/μm, our model agreed with the measurements within the experimental uncertainties. Above ~15 keV/μm we overestimate the experimental values slightly, but this is probably acceptable since LET values below 15 keV/μm are much more common in therapeutic proton beams (cf figure 4.3). One might argue that the good agreement is not surprising, as the experimental data in figure 4.2 are basically from the same studies as the data that were used to fit the tissue parameters (figure 4.1). However, it indicates that the assumptions made in the derivation of the RBE model are reasonable, in particular the use of a linear function for $\alpha_\mathrm{p}(L)$ and a constant β_p.

Paganetti and Goitein (2001) gave a very similar figure to figure 4.2, where they compared the experimental RBE data for V79 cells with the predictions of two track structure models for RBE, namely the Amorphous Track Partition (ATP) model (Butts and Katz 1967, Katz et al. 1971) and the Local Effect Model (LEM, Scholz and Kraft 1994, Scholz et al. 1997). While the LEM significantly overestimated the RBE for low LET values at the 50% survival level, the ATP model underestimated the RBE for almost the entire LET range. For LETs below 30 keV/μm, our model seems to agree better with the experimental values than the LEM or the ATP model. However, both the LEM and the ATP model can predict the decrease of RBE at higher LET values, which is beyond the scope of our model.

Since most of the experimental data in figure 4.2 are from monoenergetic proton beams, our RBE model is also compared to experiments for more realistic situations like SOBPs. The main RBE effects for SOBPs, i.e. the increase of the RBE along the SOBP plateau and the shift of the distal edge, have already been observed by other authors and could be reproduced by our model. The increasing RBE along the plateau was experimentally reported for low energy beams (e.g. Wouters et al. 1996, Tang et al. 1997) and for high energy beams (e.g. Ando et al. 2001), showing a qualitatively similar behaviour to the

RBE in figure 4.3. Experimental values of the shift of the distal falloff to greater depths are ∼1 mm for human tumour cells in a 65 MeV SOBP (Bettega et al. 2000), and ∼2 mm for rat hepatoma H4 cells in a 160 MeV SOBP (Robertson et al. 1975). These values agree well with those given in table 4.1. In a theoretical study, Paganetti and Goitein (2000) calculated RBE distributions for the survival of V79 cells in SOBPs with 70 and 120 MeV beams. For 2 Gy SOBP dose, they found an extension of the SOBP in depth (measured at the 90% dose level) of 1.2 mm in the 120 MeV beam and 0.8 mm for the low energy beam, which again corresponds well to the values in table 4.1. They reported that both the rise of RBE with depth as well as the shift to greater depths is less pronounced for higher doses, which is also consistent with our observations. This indicates that the dose averaged LET could successfully be applied as a measure for the radiation quality in polyenergetic beams. As another test of the RBE model, it would be very interesting to design and evaluate cell survival measurements for simple cases of mixed radiation fields with protons of different LET, e.g. to irradiate cells with two well defined proton beams of high and low LET simultaneously.

As soon as three-dimensional dose and LET distributions are available, the RBE can be computed at any point in the radiation field. Since the differences in RBE for a laterally constant or variable LET were small (figure 4.4), the use of a laterally constant LET is also justified from a radiobiological point of view. However, there is one point that has to be kept in mind when applying the RBE model to realistic patient geometries: compared to water phantoms, the distal falloff of the dose can become shallower in inhomogeneous media due to increased straggling and scattering of the beam when passing through high density materials like bone (cf Urie et al. 1986). This effect is not included in our dose calculations, although it might influence the LET and the RBE in the distal part of the Bragg curve.

It must also be noted that our RBE model has some more limitations. Apart from the restricted LET range (cf section 4.2.1), the dose range of our model is also limited: since it is based on the LQ model, we are confined to the validity of the LQ model, which is about 1–10 Gy. Below 1 Gy, the so-called low dose hypersensitivity (Joiner et al. 2001, Schettino et al. 2001) can cause severe deviations. As typical doses per fraction in proton therapy are above 1 Gy for the target, this effect is not critical, at least for the optimization of the dose in the target volume. For organs at risk, where the dose might well be below 1 Gy, one has to keep this limitation in mind. A special case are treatments of ocular tumours, where the dose per fraction is often higher than 10 Gy. Here the LQ model must be used with great care, and small uncertainties especially in the β parameter can lead to large errors in RBE.

Another important point is the consideration of secondary particles produced in non-elastic nuclear interactions, as they can significantly influence the total RBE due to their high biological effectiveness (Paganetti 2002). Our LET model in its current form can account for primary and secondary protons only (Wilkens and Oelfke 2003), and heavier secondaries like alpha particles are not included. This means we are underestimating the total LET, especially in the entrance region of high energy beams, where most nuclear interactions occur. However, the RBE model can implicitly account for all secondary particles, since these secondaries are certainly present in the cell survival experiments that are used to fit the parameters α_0 and λ, even if only a proton LET is reported. Unfortunately, due to the lack of data for V79 cells in the low LET region below $\sim$3 keV/μm, this does not work satisfactorily for the present parameter set. The RBE in the entrance region of the 160 MeV beam (figure 4.3) is therefore unexpectedly low (below 1.1). On the other hand, secondary particles can be neglected in the Bragg peak region, which is dominated by Coulomb interactions. Both LET and RBE are here determined by primary protons only (Paganetti 2002). In particular, the shift of the distal edge of SOBPs is therefore not affected by secondary particles.

In this work, tissue parameters for our model were only derived for the survival of V79 cells *in vitro*, mainly because there are extensive data in the literature about this cell line. One must be aware that V79 cells often show higher RBE values than other cell lines (Paganetti et al. 2002), which makes them a suitable system to study RBE effects. But this also means that it is difficult to transfer these results to other cell lines or systems, which can show significantly different behaviour. Especially in *in vivo* situations, RBE values closer to 1.1 can be expected. More biological data are therefore required to validate RBE models in *in vivo* systems and for clinically relevant endpoints. For practical applications, great care has to be taken that sufficient and appropriate biological data are used in the derivation of the tissue parameters. For tissue types other than V79 cells, the parameters of our RBE model can be derived directly from measurements, ideally for $\alpha_{\mathrm{p}}(L)$. While such data are easily available for various cell lines *in vitro* (e.g. Bettega et al. 1998, Belli et al. 2000), it becomes more difficult for *in vivo* tissues and endpoints, where often not even the photon response parameters α_{x} and β_{x} are precisely known. Another approach to obtain the tissue parameters is to fit them to simulations with other (e.g. track structure) models, provided the tissue parameters for those models have already been determined (cf the listing in Katz et al. 1994).

In summary, a phenomenological model for the RBE of protons as a function of the dose, the dose averaged LET and tissue specific parameters was proposed. Although it consists only of a few simple formulas, it reproduces the basic dependencies of RBE on dose and LET as observed by *in vitro* experiments. Despite being much simpler, our RBE model was at least comparable to track structure models in the therapeutically relevant LET region below 30 keV/μm.

The main advantage of the model is its ability to calculate three-dimensional RBE distributions extremely fast. All it needs are the tissue parameters and three-dimensional LET calculations, which can be done as fast as common dose calculation algorithms (Wilkens and Oelfke 2004). This makes it a useful tool to study the effects of a variable RBE even in inverse treatment planning, which will be investigated in the following chapter.

On the other hand, the model has several limitations, and it is only a phenomenological way to describe the RBE on the basis of experimental data. More experiments are required to obtain the tissue parameters for more clinical tissue types and endpoints. However, if one considers a constant RBE of 1.1 as the 0th order approximation of the RBE problem, this model can certainly serve as a feasible approach for the derivation of first order effects.

Chapter 5

New Optimization Strategies

5.1 Introduction

We can now take the methods for three-dimensional LET calculations and the phenomenological RBE model, which were developed in chapters 3 and 4, and apply them to the treatment planning process in proton therapy. After calculating both dose and LET distributions, the model for RBE as a function of dose, LET and tissue type allows us to obtain RBE distributions for any given treatment situation. But rather than just executing a final three-dimensional RBE calculation after the optimization of the physical dose, it would be more interesting and useful to use the LET and RBE information during the optimization, to come up with a treatment plan that is optimized in terms of the biological effect instead of the physical dose. For this purpose, new optimization strategies are required that can take these new issues into account.

The optimization is usually done by minimizing a so-called objective function using iterative algorithms (cf section 2.3.2). We will see that we can use the same optimization algorithm as before, although we have to change the objective function and add constraints in terms of LET or the biological effect. These new objective functions and some details on the implementation in *KonRad* are described in section 5.2.

In section 5.3, results for these new optimization strategies are presented. They are first applied to spread-out Bragg peaks in water as a simple example to demonstrate the potential and the limitations of the new objective functions. After that, we will consider realistic patient geometries given by computed tomography data sets, and scanning techniques for intensity modulated proton therapy. Obviously, these studies can be of exemplary nature only, although some general trends can be identified, which are discussed in section 5.4.

5.2 Methods

In inverse treatment planning one usually aims for a homogeneous physical dose in the planning target volume, leading to simple objective functions of the form

$$F_{\mathrm{D}}(\boldsymbol{w}) = \sum_{i \in \mathrm{PTV}} \left(D_i(\boldsymbol{w}) - D_{\mathrm{PTV}}\right)^2 , \tag{5.1}$$

where the quadratic deviations between the actual dose D_i in voxel i and the prescribed dose D_{PTV} are summed up for all voxels of the PTV. In practice, this objective function is often modified to account for minimum and maximum dose constraints in the target and for maximum dose constraints in organs at risk, which are weighted by so-called penalty factors (cf section 2.3.2 and equation (2.5)). In the following, I will describe how this objective function can be modified to account for the LET (section 5.2.1) and (more promising) for the biological effect (section 5.2.2).

5.2.1 Objective function for LET constraints

As the RBE depends on dose, LET and tissue type, one new optimization strategy could be to aim not only for a homogeneous dose, but also for a homogeneous LET distribution in the target, as this would yield a homogeneous biological effect (RBE × dose). The corresponding objective function (which will be called “LET objective function” in the following) would be

$$F_{\mathrm{D,L}}(\boldsymbol{w}) = \nu_{\mathrm{D}} F_{\mathrm{D}}(\boldsymbol{w}) + \nu_{\mathrm{L}} F_{\mathrm{L}}(\boldsymbol{w}) \tag{5.2}$$

with

$$F_{\mathrm{L}}(\boldsymbol{w}) = \sum_{i \in \mathrm{PTV}} \left(L_i(\boldsymbol{w}) - \overline{L}(\boldsymbol{w})\right)^2 , \tag{5.3}$$

where ν_{D} and ν_{L} are penalty factors, L_i is the dose averaged LET at voxel i and $\overline{L}$ is the mean LET in the PTV:

$$\overline{L}(\boldsymbol{w}) = \frac{1}{N_{\mathrm{PTV}}} \sum_{i \in \mathrm{PTV}} L_i(\boldsymbol{w}), \tag{5.4}$$

where N_{PTV} is the number of voxels in the PTV.

Note that we did not prescribe a certain LET value to the target volume (as such a constraint would be extremely difficult to meet in the optimization), but we rather minimize the variance of the LET in the target. However, it is still difficult to satisfy the constraints of homogeneous dose and LET at the same time. To use this LET objective function in a simple gradient optimization algorithm, the first partial derivatives of F_L have to be known. As

$$\frac{\partial D_i(\boldsymbol{w})}{\partial w_k} = \frac{\partial}{\partial w_k} \sum_j w_j D_{ij} = D_{ik} \qquad \text{and} \tag{5.5}$$

$$\frac{\partial L_i(\boldsymbol{w})}{\partial w_k} = \frac{\partial}{\partial w_k} \frac{1}{D_i(\boldsymbol{w})} \sum_j w_j L_{ij} D_{ij} = \frac{D_{ik}}{D_i(\boldsymbol{w})} (L_{ik} - L_i(\boldsymbol{w})), \tag{5.6}$$

they are

$$\frac{\partial F_\mathrm{L}(\boldsymbol{w})}{\partial w_k} = \sum_{i \in \mathrm{PTV}} 2 \cdot (L_i - \overline{L}) \cdot \left[\frac{D_{ik}}{D_i}(L_{ik} - L_i) - \frac{1}{N_\mathrm{PTV}} \sum_{j \in \mathrm{PTV}} \frac{D_{jk}}{D_j}(L_{jk} - L_j) \right]. \tag{5.7}$$

The advantage of this approach would be that there are only physical parameters (dose and LET) involved in the objective function, i.e. no tissue dependent biological parameters have to be determined. But even for homogeneous dose and LET in the PTV, one would still need one global (biological) RBE value for the whole PTV.

Another option for LET based objective functions would be to include maximum LET constraints in organs at risk, which could be done in close analogy to the commonly used maximum dose constraints (cf equation (2.5)). Again, this might be very difficult to accomplish due to the physical properties of the proton depth dose curve, which shows very high LET at low doses in the region behind the Bragg peak. There is probably no reason to penalize high LET values in a voxel that is exposed to very low doses only.

5.2.2 Objective function for the biological effect

A second, more general approach is the direct optimization of the biological outcome (i.e. the product of RBE and dose). This will provide more degrees of freedom than the objective function in the previous section, as dose and LET may vary within the PTV, as long as the biological effect is constant. Rather than explicitly integrating the RBE formula (4.7) from chapter 4 in the objective function, we will use the biological effect $E = -\ln S = \alpha D + \beta D^2$ from the linear quadratic model, as this offers some practical and computational advantages. To get a homogeneous biological effect in the PTV, we just have to change the objective function to

$$F_\mathrm{E}(\boldsymbol{w}) = \sum_{i \in \mathrm{PTV}} (E_i(\boldsymbol{w}) - E_\mathrm{PTV})^2 . \tag{5.8}$$

By applying equations (4.4) and (4.6) for the dependencies of the proton response parameters $\alpha_{\mathrm{p}}^{\mathrm{PTV}}$ and $\beta_{\mathrm{p}}^{\mathrm{PTV}}$ on LET for the tissue of the PTV, we get

$$\begin{aligned} F_{\mathrm{E}}(\boldsymbol{w}) &= \sum_{i\in\mathrm{PTV}} \left(\alpha_{\mathrm{p}}^{\mathrm{PTV}}(L_i(\boldsymbol{w}))D_i(\boldsymbol{w}) + \beta_{\mathrm{p}}^{\mathrm{PTV}} D_i^2(\boldsymbol{w}) - E_{\mathrm{PTV}}\right)^2 \\ &= \sum_{i\in\mathrm{PTV}} \left((\alpha_0^{\mathrm{PTV}} + \lambda^{\mathrm{PTV}} L_i(\boldsymbol{w}))D_i(\boldsymbol{w}) + \beta_{\mathrm{p}}^{\mathrm{PTV}} D_i^2(\boldsymbol{w}) - E_{\mathrm{PTV}}\right)^2 \\ &= \sum_{i\in\mathrm{PTV}} \left(\alpha_0^{\mathrm{PTV}} D_i(\boldsymbol{w}) + \lambda^{\mathrm{PTV}} \mathcal{L}_i(\boldsymbol{w}) + \beta_{\mathrm{p}}^{\mathrm{PTV}} D_i^2(\boldsymbol{w}) - E_{\mathrm{PTV}}\right)^2, \qquad (5.9) \end{aligned}$$

where $\mathcal{L}_i(\boldsymbol{w}) = L_i(\boldsymbol{w})D_i(\boldsymbol{w})$ is the product of LET and dose (cf section 3.2.4.3). Minimizing this objective function will lead to a homogeneous biological effect and therefore to a homogeneous distribution of the product of RBE and dose in the PTV. The “prescribed effect” E_{PTV} can be connected to the prescribed X-ray dose D_{PTV} by $E_{\mathrm{PTV}} = \alpha_{\mathrm{x}} D_{\mathrm{PTV}} + \beta_{\mathrm{x}} D_{\mathrm{PTV}}^2$. In the following, this new objective function will be called “RBE objective function”. In this context I will even speak of “RBE optimization”, although it is certainly not the RBE itself that is optimized, but rather the biological effect or the product of RBE and dose.

In equation (5.9), both D_i and L_i depend on the beam weights $\boldsymbol{w}$, but the Newton gradient method for the optimization still works. For this algorithm, the partial derivatives of $F_{\mathrm{E}}(\boldsymbol{w})$ have to be calculated. As

$$\frac{\partial \mathcal{L}_i(\boldsymbol{w})}{\partial w_k} = \frac{\partial}{\partial w_k} L_i(\boldsymbol{w})D_i(\boldsymbol{w}) = \frac{\partial}{\partial w_k} \sum_j L_{ij} D_{ij} w_j = L_{ik} D_{ik}, \qquad (5.10)$$

we get

$$\begin{aligned} \frac{\partial F_{\mathrm{E}}(\boldsymbol{w})}{\partial w_k} &= \sum_{i\in\mathrm{PTV}} 2\left(\alpha_0^{\mathrm{PTV}} D_i(\boldsymbol{w}) + \lambda^{\mathrm{PTV}} \mathcal{L}_i(\boldsymbol{w}) + \beta_{\mathrm{p}}^{\mathrm{PTV}} D_i^2(\boldsymbol{w}) - E_{\mathrm{PTV}}\right) \\ &\qquad \times \left(\alpha_0^{\mathrm{PTV}} D_{ik} + \lambda^{\mathrm{PTV}} L_{ik} D_{ik} + 2\beta_{\mathrm{p}}^{\mathrm{PTV}} D_i(\boldsymbol{w}) D_{ik}\right). \qquad (5.11) \end{aligned}$$

For the Newton gradient approach as it is implemented in *KonRad* (cf Nill 2001, p 12), the second partial derivatives are also needed:

$$\begin{aligned} \frac{\partial^2 F_{\mathrm{E}}(\boldsymbol{w})}{\partial w_k^2} &= \sum_{i\in\mathrm{PTV}} \Big[4\left(\alpha_0^{\mathrm{PTV}} D_i(\boldsymbol{w}) + \lambda^{\mathrm{PTV}} \mathcal{L}_i(\boldsymbol{w}) + \beta_{\mathrm{p}}^{\mathrm{PTV}} D_i^2(\boldsymbol{w}) - E_{\mathrm{PTV}}\right) \beta_{\mathrm{p}}^{\mathrm{PTV}} D_{ik}^2 \\ &\qquad + 2\left(\alpha_0^{\mathrm{PTV}} D_{ik} + \lambda^{\mathrm{PTV}} L_{ik} D_{ik} + 2\beta_{\mathrm{p}}^{\mathrm{PTV}} D_i(\boldsymbol{w}) D_{ik}\right)^2\Big]. \qquad (5.12) \end{aligned}$$

Note that in equations (5.9), (5.11) and (5.12) the LET L_i never appears “alone”, but only in products with D_i, i.e. as $\mathcal{L}_i$. The latter can be calculated easily as $\sum_j L_{ij} D_{ij} w_j$

(cf section 3.2.4.3), which simplifies the computational effort required for evaluating these equations.

If a minimum and a maximum constraint for the PTV are given ($D^{\text{PTV}}_{\text{min}}$ and $D^{\text{PTV}}_{\text{max}}$), they can be converted to minimum and maximum effect levels by

$$E^{\text{PTV}}_{\text{min}} = \alpha_{\text{x}} D^{\text{PTV}}_{\text{min}} + \beta_{\text{x}} D^{\text{PTV}^2}_{\text{min}} \qquad \text{and} \qquad E^{\text{PTV}}_{\text{max}} = \alpha_{\text{x}} D^{\text{PTV}}_{\text{max}} + \beta_{\text{x}} D^{\text{PTV}^2}_{\text{max}} \tag{5.13}$$

and the corresponding objective function (cf equation (2.5b)) will be

$$\tilde{F}_{\text{E}}(\boldsymbol{w}) = \nu^{\text{PTV}}_{\text{min}} \sum_{i \in \text{PTV}} [C_{+}(E^{\text{PTV}}_{\text{min}} - E_i)]^2 + \nu^{\text{PTV}}_{\text{max}} \sum_{i \in \text{PTV}} [C_{+}(E_i - E^{\text{PTV}}_{\text{max}})]^2. \tag{5.14}$$

This objective function can be extended easily to include maximum effect constraints in organs at risk in the usual way as given in equations (2.5a) – (2.5c). While the respective penalty factors keep the same meaning, all constraints that were given as an X-ray or photon dose have to be translated to constraints in terms of the biological effect using $E = \alpha_{\text{x}} D + \beta_{\text{x}} D^2$. The tissue parameters α_{x}, β_{x}, α_0, λ and β_{p} are then needed for every organ under consideration.

5.2.3 Implementation in *KonRad*

The new objective functions were integrated into our research version of the inverse planning tool *KonRad* (cf section 2.3). However, at the current point the implementation of the LET objective function in *KonRad* is still work in progress, and I will therefore concentrate on the RBE objective function in the following. The methods for calculating and accessing the L_{ij} matrix and for obtaining three-dimensional LET distributions in *KonRad* were already described in section 3.2.4. Now some additional input data are required for the RBE objective function, and I will also describe what kind of output data is produced by *KonRad*.

5.2.3.1 Input data for *KonRad*

Besides the usual functionality of the *KonRad* system (cf Nill 2001), the user can now choose between either the "normal" optimization of the physical dose, or the new optimization of the biological effect, i.e. using objective function (5.9). In any case, the user can request a final calculation of three-dimensional LET or RBE distributions after the optimization to study the LET and RBE effects for the normal optimization of the physical dose as well.

If RBE calculations or the optimization of the biological effect are chosen, it is further necessary to provide the biological tissue parameters α_{x}, β_{x}, α_0, λ and β_{p} for each classified tissue volume or organ (PTV, organs at risk, normal tissue). If more than one organ at risk are given, the parameters have to be specified for every OAR separately. They are read into *KonRad* from a patient-specific configuration file. Internally, *KonRad* assigns a set of tissue parameters to every voxel within the patient, depending on the (unique) organ classification of the respective voxel.

Another point that has to be noted is that RBE calculations have to be done for the dose per fraction rather than the total dose (cf chapter 4). To take this into account, the user has to specify the number of fractions. The constraints for the optimization are given as usual in terms of the total dose and they are then internally converted to doses per fraction by dividing them by the number of fractions.

When optimizing the physical dose, the constraints are interpreted as physical proton doses. In the case of optimizing the biological effect, the constraints specified by the user are considered to be physical photon doses, i.e. they are the same as one would use for a photon optimization. They are then translated internally to constraints in terms of the biological effect as described above.

5.2.3.2 Output data from *KonRad*

After the optimization, the results are written to files: besides the dose cube, three-dimensional distributions of dose averaged LET, RBE, RBE × dose and the surviving fraction can be exported as requested by the user. Additionally, a file providing statistical information of these cubes is created. It states the minimum and maximum values of the respective distributions and the normalization values. These cubes can be further processed and visualized as desired, e.g. to obtain dose-volume-histograms (DVHs) or to compare different plans.

5.3 Results

The new objective functions that were introduced in the last section can be used either in *KonRad* or in any other optimization program, e.g. for spread-out Bragg peaks. As the latter are a simple example for the demonstration of the new optimization strategies, I will first show some results for SOBPs (section 5.3.1). After that, the effects of the new objective functions for several clinical cases with IMPT plans in *KonRad* are presented in section 5.3.2.

Parameter	Value	Unit
α_{x}	0.112	Gy^{-1}
β_{x}	0.0298	Gy^{-2}
α_0	0.1	Gy^{-1}
λ	0.02	$\mu\mathrm{m}\ \mathrm{keV}^{-1}\ \mathrm{Gy}^{-1}$
β_{p}	0.0298	Gy^{-2}

Table 5.1: *Tissue parameters used in all calculations of the biological effect in this work. They are the values for the survival of V79 Chinese hamster cells in vitro as derived in chapter 4.*

For the calculation of the biological effect with the phenomenological RBE model, a set of biological parameters for every tissue under consideration is required. However, it is not the aim of this work to derive exact parameter sets for clinically relevant tissue types. We rather want to investigate the effects of a variable RBE in IMPT in general, and therefore just one set of parameters is used for all organs or tissue types in all following RBE calculations. For simplicity, we will use the values derived in section 4.2.2 for V79 Chinese hamster cells relative to ^{60}Co gamma-rays, which are summarized in table 5.1.

5.3.1 Optimization of spread-out Bragg peaks

Spread-out Bragg peaks were optimized using a simple gradient algorithm and the objective functions given in section 5.2. A predefined number of pristine peaks was placed in equidistant steps along the intended modulation width of the SOBP.

5.3.1.1 LET optimization

Let us first investigate the LET objective function (5.2), which aims at a homogeneous dose and a homogeneous LET simultaneously. The relative importance of these two objectives is given by the penalty factors ν_{D} and ν_{L}. Figure 5.1 shows an example for SOBPs with three different penalty settings ($\nu_{\mathrm{D}} = 1$; $\nu_{\mathrm{L}} = 0$), (0; 1) and (0.5; 0.5), corresponding to “pure dose”, “pure LET” and equally weighted optimization of both. All SOBPs consist of 15 peaks with an initial energy of 70 MeV (range 40 mm), which are modulated in range to cover the depth interval 11–31 mm. This energy in conjunction with SOBPs is typically used for the treatment of ocular tumours.

The configuration given in figure 5.1a is of course just the usual SOBP with a homogeneous dose in the SOBP plateau. But here the LET increases along the plateau, as it was

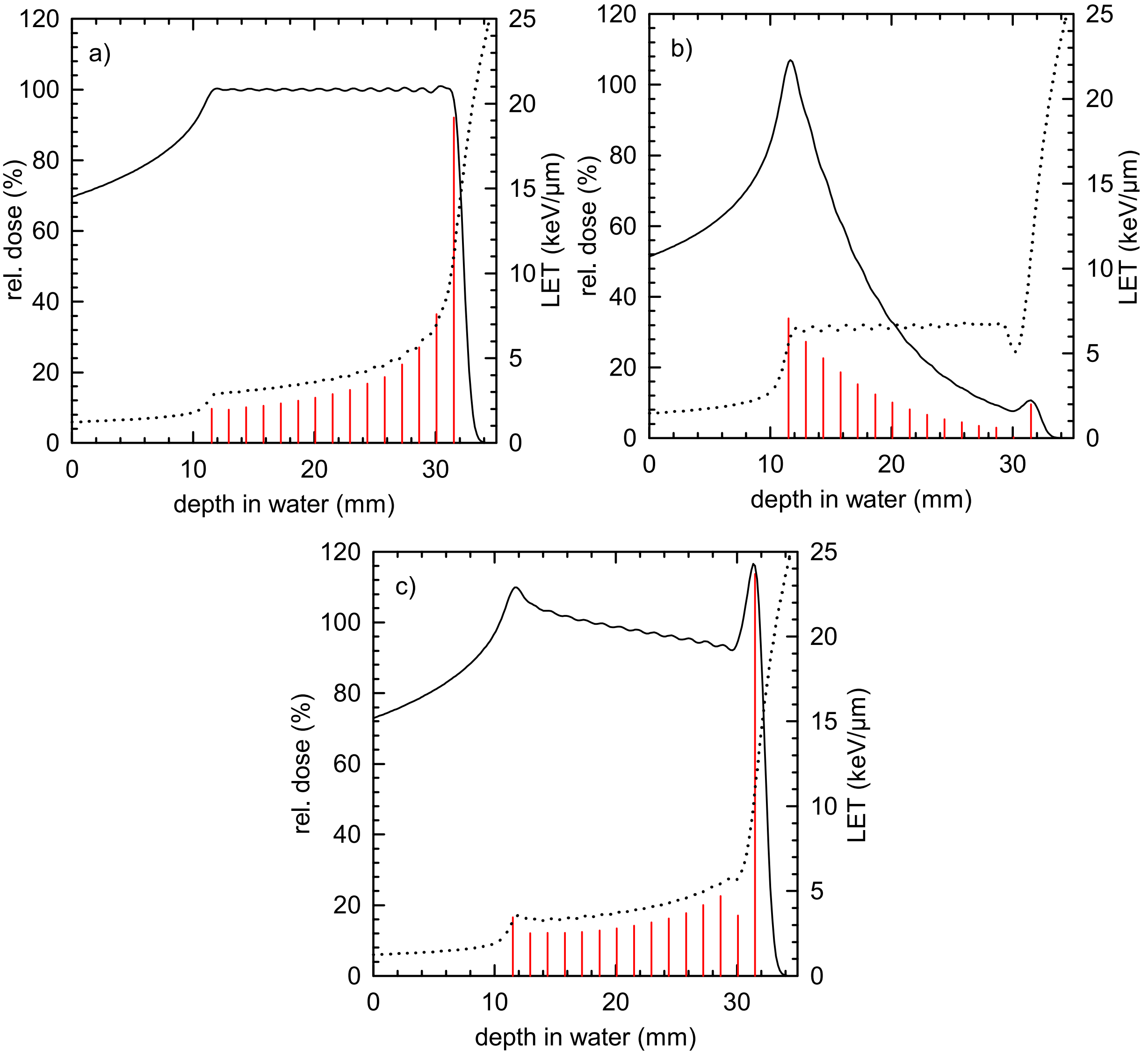

Figure 5.1: *Dose (——) and LET (······, right ordinate) distributions for spread-out Bragg peaks that were optimized for three different penalty settings in the LET objective function: (a) pure dose optimization ($\nu_\mathrm{D} = 1$; $\nu_\mathrm{L} = 0$), (b) pure LET optimization (0; 1) and (c) equal weighting of both objectives (0.5; 0.5). The red vertical lines indicate the positions and the relative weights of the constituent pristine peaks.*

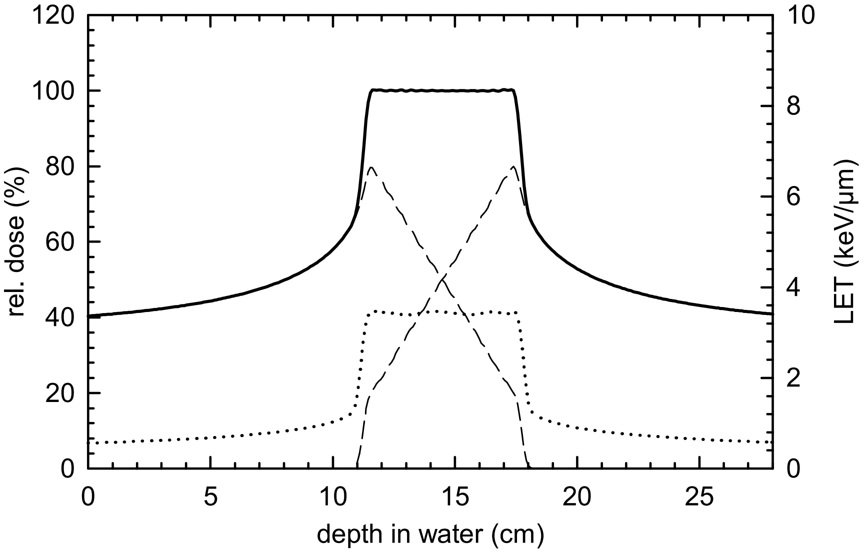

Figure 5.2: *Total dose (——) and LET (······, right ordinate) distributions for two opposing beam ports with a maximum energy of 160 MeV. The weights of the pristine peaks were optimized to yield homogeneous dose and LET distributions in the depth interval 11.5–17.5 cm, using* $\nu_\mathrm{D} = 0.5$ *and* $\nu_\mathrm{L} = 0.5$*. The dose contributions of the two fields are given by the broken lines.*

already pointed out in chapter 3. If one aims for a homogeneous LET only (figure 5.1b), this can be achieved by a modified dose profile: the dose is now much lower in the distal part of the SOBP to compensate the increase in LET. In figure 5.1c, both objectives are weighted equally, which apparently does not lead to a good compromise. While the LET is not much better than in figure 5.1a, the dose distribution is considerably worse. However, these results show that the new objective function works in principle. The unacceptable results of figure 5.1c are due to the physical properties in terms of dose and LET of the pristine Bragg peaks - it is simply not possible to have homogeneous dose and LET simultaneously in a SOBP.

To get flat distributions of both dose and LET, one needs more degrees of freedom in the optimization. This can be accomplished for example by two opposing beams for the treatment of deep seated tumours (figure 5.2). Now there are several possibilities for obtaining a flat total dose, and among them is also a solution that gives a homogeneous LET distribution in the region of interest. For two opposing beam directions, each with 15 pristine peaks with a maximum energy of 160 MeV, the total dose and LET distributions were optimized using $\nu_\mathrm{D} = 0.5$ and $\nu_\mathrm{L} = 0.5$. While the two beam ports both deliver a non-uniform dose, the total dose and LET showed good uniformity in the "target" region (figure 5.2). This means that although the LET optimization did not work satisfactorily

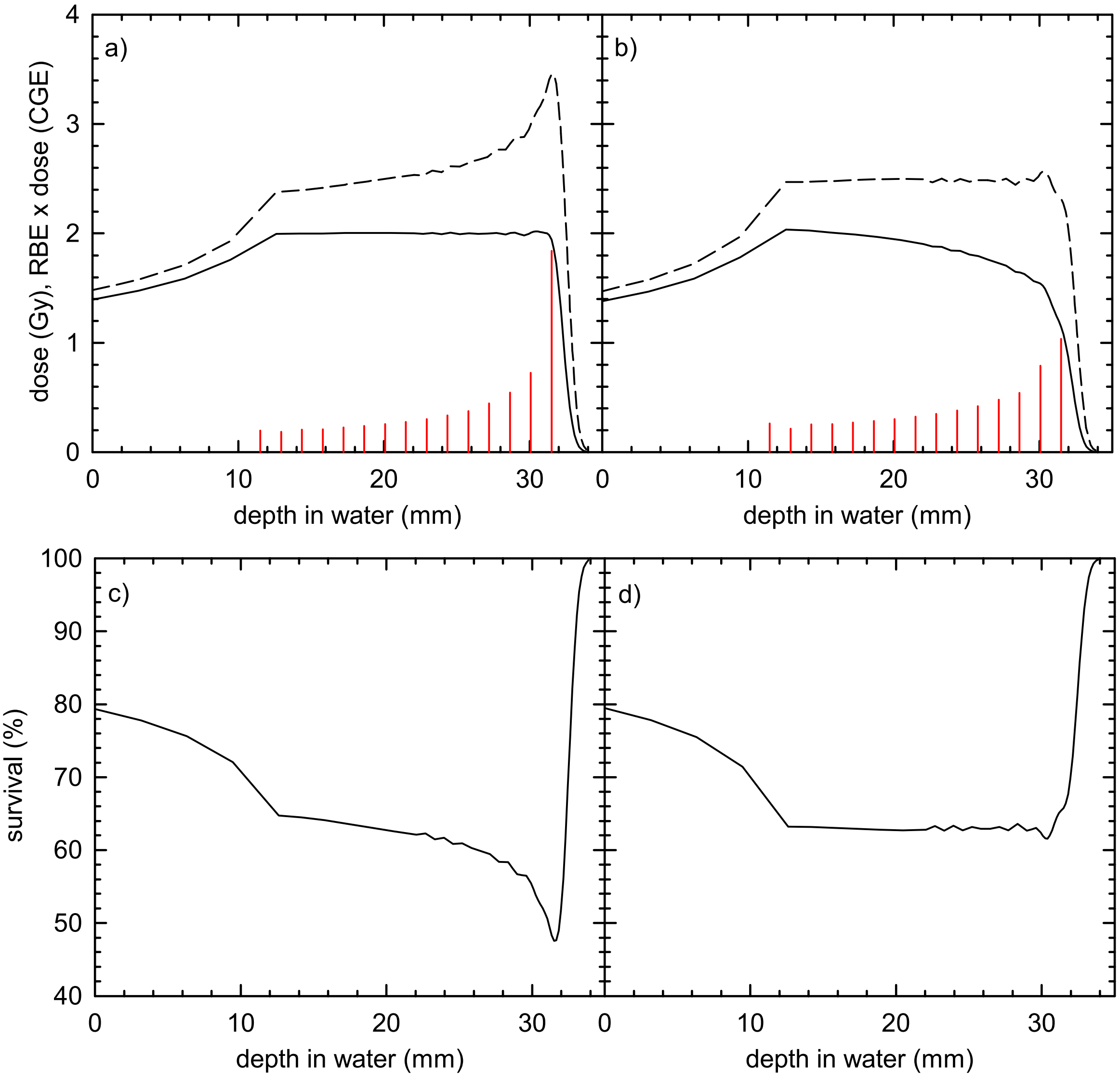

Figure 5.3: *Dose (——) and RBE× dose (– – –) distributions for spread-out Bragg peaks that were optimized to yield a homogeneous dose (left) and a homogeneous biological effect (right) for the survival of V79 cells in vitro relative to* ^{60}*Co. The red vertical lines indicate the positions and the relative weights of the constituent pristine peaks. The corresponding cell survival levels are given in panels (c) and (d).*

for one beam direction, it might have applications for more than one beam port, e.g. in IMPT with the 3D modulation technique. However, this approach will not be pursued any further in this work.

5.3.1.2 Optimization of the biological effect

Next, I will give an example for an SOBP that was optimized with the RBE objective function (5.9). Now dose and LET are allowed to vary within the modulation region, as long as the biological effect (RBE × dose) is uniform in the desired depth interval. Figure 5.3 illustrates a typical result for a SOBP with 15 pristine peaks and a maximum energy of 70 MeV (same configuration as in figure 5.1). On the left hand side (figure 5.3a) is again the usual optimization of the physical dose (with 2 Gy in the SOBP), while the graph on the right hand side (figure 5.3b) corresponds to the new objective function. In both cases, the biological effect in terms of RBE × dose is also given. While RBE × dose did not show a uniform plateau for the dose optimization (cf section 4.3), it became flat for the RBE objective function. This was accomplished by reducing the dose in the distal part of the SOBP and thereby compensating for the increasing RBE. In figures 5.3c and 5.3d, the surviving fraction of V79 cells as a function of depth is given for both cases. For the dose optimization, there is a distinctive dip to smaller survival levels at the distal edge of the SOBP, while this effect almost vanished for the RBE objective function.

5.3.2 Optimization of IMPT

In this section, the effects of a variable RBE for several clinical examples with IMPT scanning techniques will be investigated. However, it is not the aim of this work to present the best clinical plan for these cases, but rather to demonstrate the RBE effects and optimization strategies for scanning techniques using typical patient geometries.

In particular, two cases will be studied in detail: a patient with a clivus chordoma, and a patient with a carcinoma of the prostate. The chordoma was chosen because its concave shape and its close location to the brainstem make it very difficult to treat with conventional photon radiotherapy. It is therefore an ideal candidate for more sophisticated techniques like intensity modulated radiotherapy (IMRT) with photons or IMPT. Furthermore, chordomas are a standard tumour site in clinical proton therapy (e.g. Debus et al. 1997, Noël et al. 2001). Proton therapy is also used for prostate carcinomas (e.g. Rossi 1999), although many of these tumours are treated with different modalities as well. Due to their high rate of incidence, prostate carcinomas are frequently studied, and many people could benefit from therapeutical improvements.

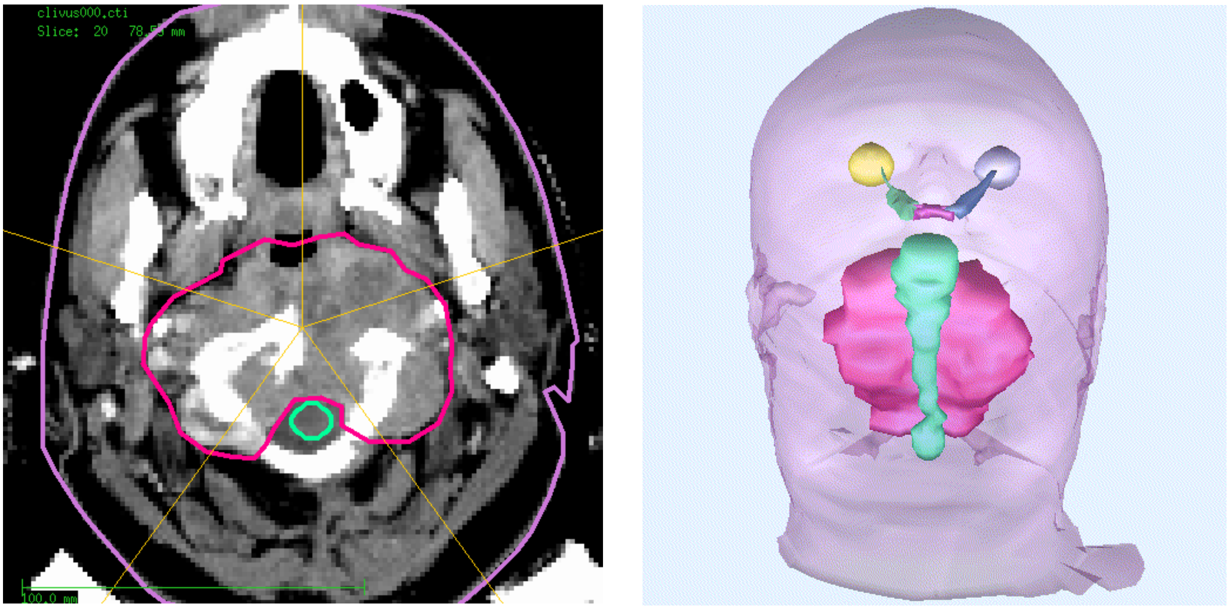

Figure 5.4: *Left: Transversal CT slice through the isocentre for the patient with the clivus chordoma. The planning target volume (PTV) and the brainstem as organ at risk are indicated by the red and green lines, respectively. The five incident beam directions are given by the yellow lines. Right: Three-dimensional view of the PTV (red) and the brainstem (green) as seen from the patient's back. The eyes, the optical nerves and the chiasm are also outlined.*

For every case I will first describe the geometry of the anatomy and the planning objectives. After that, several treatment plans using different scanning techniques (distal edge tracking and 3D modulation) and different objective functions (dose or RBE optimization) will be presented. All plans were optimized in *KonRad* using five coplanar, equally spaced beam ports. For all plans a final calculation of three-dimensional LET and RBE distributions was performed, so that they can be evaluated and compared in terms of dose, LET and RBE × dose.

5.3.2.1 Clinical case 1: clivus chordoma

Anatomy and clinical objectives The anatomy of the patient with the clivus chordoma is shown in figure 5.4. The planning target volume is situated in the centre of the patient's head and wraps closely around the brainstem as the primary organ at risk. The five coplanar, equally spaced beam directions are indicated in figure 5.4. The maximum beam energy used was 200 MeV for the anterior-posterior beam, and 160 MeV for all other beams. The lateral distance between beam spots was set to 6 mm. This led to a

Organ	D_{min}	ν_{min}	D_{max}	ν_{max}
PTV	68 CGE	99	71.5 CGE	20
brainstem	—	—	0 CGE	6
normal tissue	—	—	70 CGE	3

Table 5.2: *Optimization constraints (minimum dose, maximum dose and the respective penalty factors, cf equation (2.5)) for the clivus chordoma case. While the maximum dose constraint for the brainstem is rather tight to spare the brainstem as much as possible, the constraints for the PTV allow for small inhomogeneities in the dose distribution.*

total number of 690 beam spots for distal edge tracking and 10 066 beam spots for 3D modulation.

The objectives of the planning process were to deliver a homogeneous dose of 70 CGE in 35 fractions to the PTV (i.e. with a dose per fraction of 2 CGE), while sparing the brainstem as much as possible. The dose constraints used for the optimization are listed in table 5.2 and were taken from Nill (2001), where an extensive planning comparison for this patient using intensity modulated photon, electron, proton and carbon beams was presented. Besides the brainstem, the “normal tissue” consisting of all patient voxels except the PTV and brainstem was considered as an organ at risk in the optimization. The eyes, the optical nerves and the chiasm were far enough away from the PTV not to be included as separate organs at risk.

Note that the constraints are given here in units of CGE, i.e. in terms of “photon dose”. For the RBE optimization, these values can be used directly to calculate the “prescribed effect” (cf section 5.2.2). To compare the new RBE optimization with treatment plans obtained by the usual optimization of the physical dose, the constraints have to be converted to appropriate proton doses. This was done by dividing the constraints from table 5.2 by the mean RBE in the PTV, which was 1.14 for distal edge tracking and 1.25 for the 3D modulation (see below). This procedure ensured that the final (dose dependent) RBE calculation after the dose optimization was done with the correct values for the proton dose per fraction to yield the desired CGE level.

Treatment plans for distal edge tracking Let us first consider treatment plans using the distal edge tracking technique. For the optimization constraints given above, two plans were generated: the first plan was optimized using the “normal” objective function, i.e. aiming for a homogeneous physical dose in the planning target volume. Dose and LET distributions for this plan were already displayed in figure 3.10. Applying the RBE model

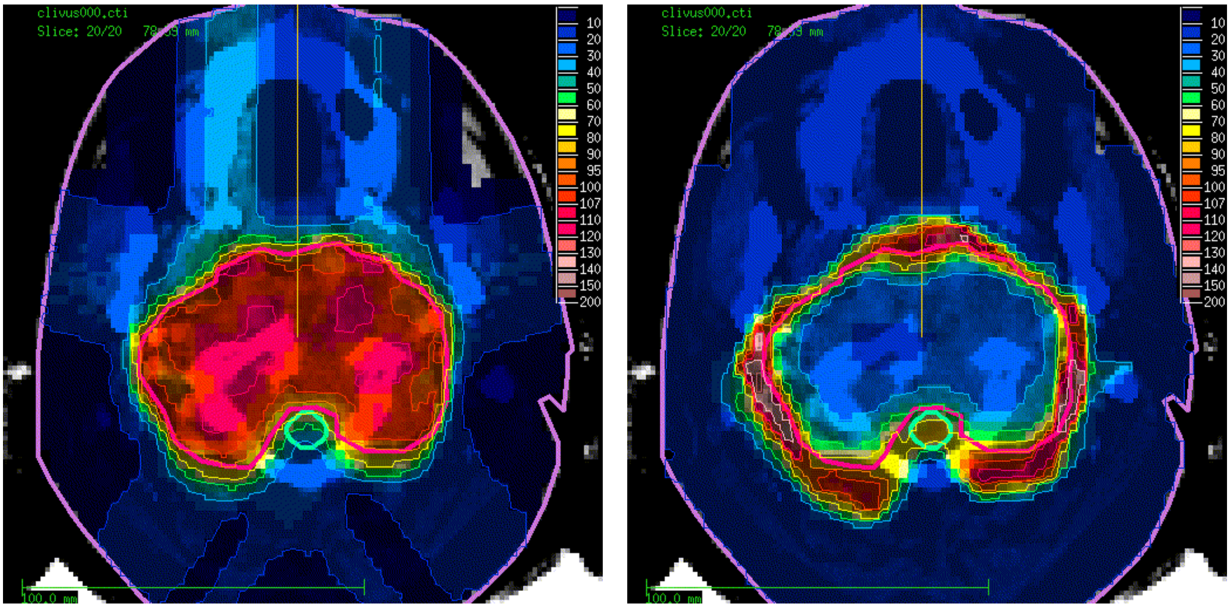

Figure 5.5: *Dose (left) and LET (right) distributions in a transversal slice through the isocentre for the new RBE optimization using the distal edge tracking technique. The colour scales are normalized to* $100\% = 1.75$ *Gy per fraction and* $100\% = 5$ *keV/µm, respectively.*

in a final step after the optimization yielded the distribution of RBE × dose shown on the left side of figure 5.6. For the second plan, the new RBE objective function was employed to obtain a homogeneous biological effect. The corresponding distributions of dose, LET and RBE × dose are given in figure 5.5 and on the right hand side of figure 5.6.

As expected, the dose optimized plan gave a uniform physical dose distribution that was highly conformal to the PTV (left side in figure 3.10). However, as already seen in chapter 3, the LET values were low in the centre of the PTV and much higher at the border and outside of the PTV. This led to an inhomogeneous distribution of the RBE and therefore also of RBE × dose, which becomes apparent in figure 5.6 (left hand side). In particular, there are some regions of considerable overdosage, e.g. at the left and right lateral edges of the PTV in the slice shown in figure 5.6 where RBE × dose exceeds 130% (white isodose line) of the desired 2 CGE. Note that the highest LET values in the normal tissue (e.g. in the region posterior of the PTV) do not have a significant impact on the biological effect, since the dose is very low in this region due to the steep physical dose gradient. This means that although the RBE is high, the product of RBE and dose is still low. For this plan, the RBE in the PTV ranged between 1.0 and 1.6 with a mean of 1.14, which is in agreement with the underlying cell survival experiments. The overall RBE maximum in this plan was 2.8 in the normal tissue surrounding the PTV.

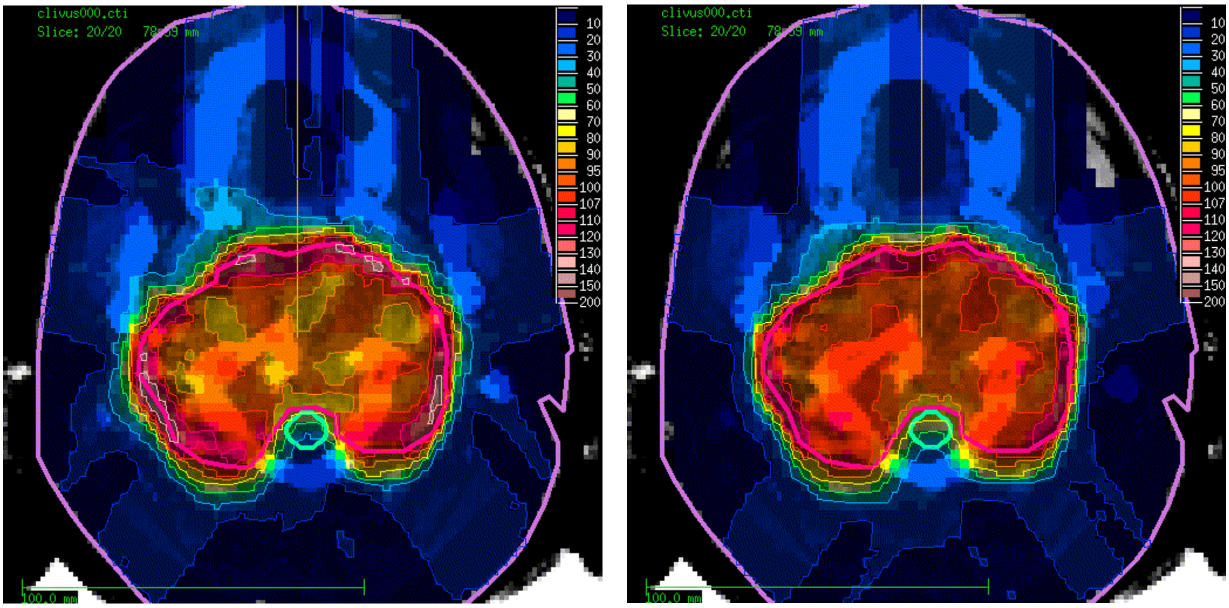

Figure 5.6: *Distributions of the product of RBE and dose in a transversal slice through the isocentre for the normal dose optimization (left) and for the new RBE optimization (right), both for the distal edge tracking technique. The colour scales are normalized to* 100% = 2 *CGE per fraction.*

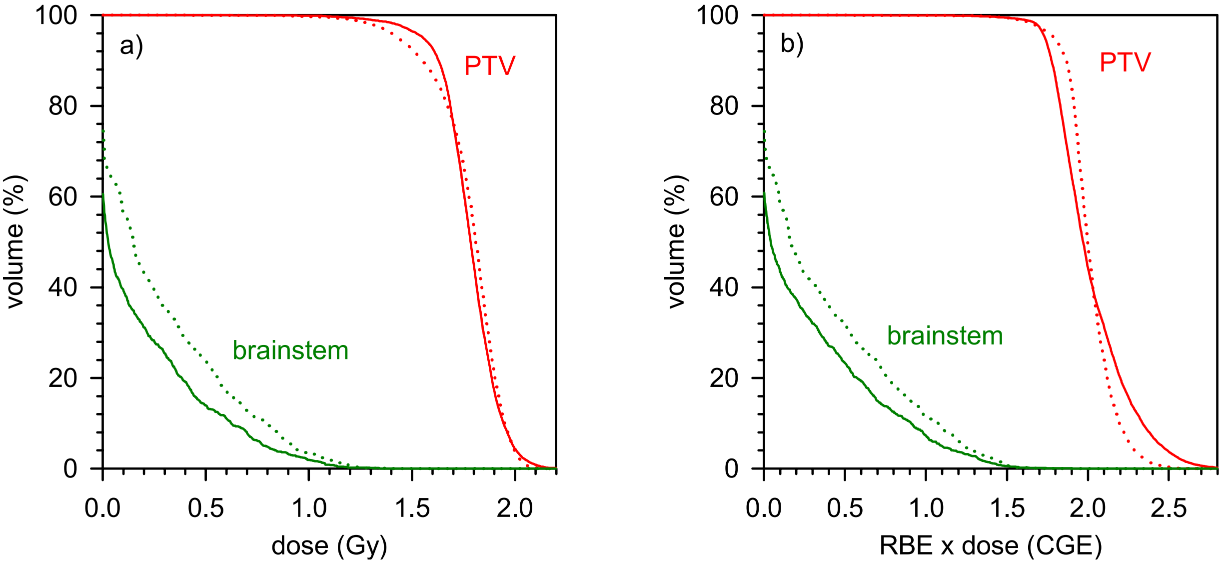

Figure 5.7: *Dose-volume-histograms for the two distal edge tracking plans for the clivus chordoma. The DVHs of the PTV (red) and the brainstem (green) are given for the physical dose (a) and for the product of RBE and dose (b). The solid lines correspond to the dose optimization (optimized to yield 1.75 Gy per fraction), while the dotted lines show the DVHs for the RBE optimization (optimized to 2 CGE per fraction).*

Statistical analysis for the PTV			**Min**	**Max**	**Mean**	$\boldsymbol{\sigma}$
DET	dose	(Gy)	0.63	2.30	1.78	0.14
dose optimized	LET	(keV/μm)	1.0	7.3	2.1	1.1
	RBE × dose	(CGE)	0.73	2.97	2.02	0.23
DET	dose	(Gy)	0.40	2.17	1.78	0.17
RBE optimized	LET	(keV/μm)	1.0	8.3	2.1	1.1
	RBE × dose	(CGE)	0.55	2.77	2.01	0.15
3D	dose	(Gy)	0.53	2.07	1.61	0.11
dose optimized	LET	(keV/μm)	1.4	5.1	3.5	0.4
	RBE × dose	(CGE)	0.84	2.58	2.03	0.14
3D	dose	(Gy)	0.53	1.92	1.58	0.10
RBE optimized	LET	(keV/μm)	1.7	5.3	3.6	0.4
	RBE × dose	(CGE)	0.77	2.47	2.00	0.11

Table 5.3: *Statistical analysis of dose, LET and RBE × dose distributions per fraction in the PTV for four different treatment plans for the clivus chordoma: for both the distal edge tracking technique and the 3D modulation, plans were considered using either the normal dose optimization ("dose optimized") or the optimization of the biological effect ("RBE optimized"). For every case, the minimum and maximum values as well as the mean and the standard deviation are given.*

Let us now look at the RBE optimized plan (figure 5.5 and right hand side in figure 5.6), which was optimized to yield a homogeneous biological effect in the PTV. Indeed, the product of the variable RBE and the dose was now more homogeneous in the PTV (figure 5.6), while the brainstem was mostly spared from dose. As the LET did not change much (cf figures 3.10 and 5.5), this improvement in RBE × dose was achieved by varying the physical dose in the PTV: the dose is higher in the middle of the PTV, where the LET is low, while the dose is lowered in the high LET regions at the PTV border, where the RBE gets higher. While this effect is difficult to see in the "colourwash" displays of figures 3.10 and 5.5, it will become apparent for the prostate case in section 5.3.2.2, where profiles through the dose distributions will be presented. These observations are also evident in the dose-volume-histograms (figure 5.7): the DVH of the PTV for RBE × dose is steeper for the RBE optimization than for the dose optimization, but the physical dose is less homogeneous. A detailed comparison of the two plans is also given in table 5.3, where minimum and maximum values as well as the mean and the standard deviation are listed for physical dose, LET and RBE × dose.

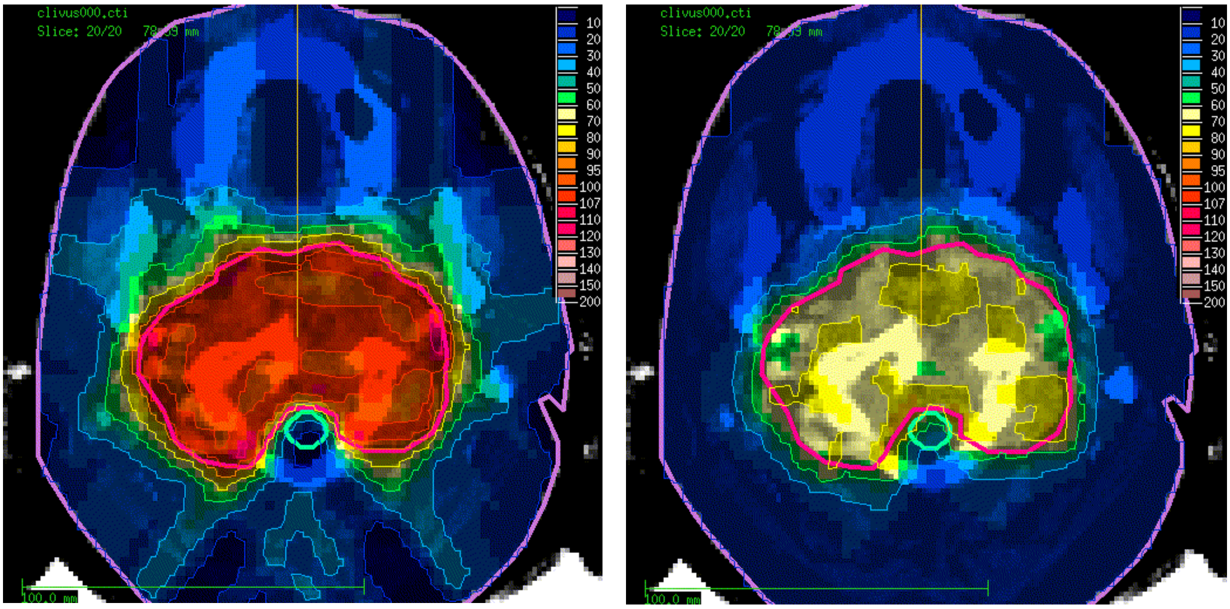

Figure 5.8: *Distributions of dose (left) and LET (right) in a transversal slice through the isocentre for the new RBE optimization using the 3D modulation technique. The colour scales are normalized to* $100\% = 1.6$ *Gy per fraction and* $100\% = 5$ *keV/μm, respectively.*

Treatment plans for 3D modulation I will now present treatment plans for the same patient but with the 3D modulation technique instead of distal edge tracking. Again, one plan was done with the normal dose optimization, and a second plan was obtained using the RBE objective function. Dose and LET distributions for the normal optimization were already displayed in figure 3.11. The corresponding distributions for the RBE optimization are shown in figure 5.8, and the resulting distributions of RBE × dose are shown in figure 5.9.

As we already saw in chapter 3, the 3D modulation technique shows a much more homogeneous LET distribution in the PTV than the distal edge tracking technique. This means that there are not much RBE variations in the PTV, and RBE × dose is more or less uniform, even for the normal optimization of the physical dose (left side in figure 5.9). Here the RBE in the PTV ranged between 1.1 and 1.6 with a mean of 1.25. If the RBE optimization is activated, a slight improvement of the homogeneity of RBE × dose can also be achieved in this case, although it is difficult to see in the colourwash displays (figure 5.9). Only the DVHs reveal that RBE × dose in the PTV is better for the new optimization method (figure 5.10). However, these differences are relatively small for the 3D modulation technique. A numerical analysis of the respective dose, LET and RBE × dose distributions can be found in table 5.3.

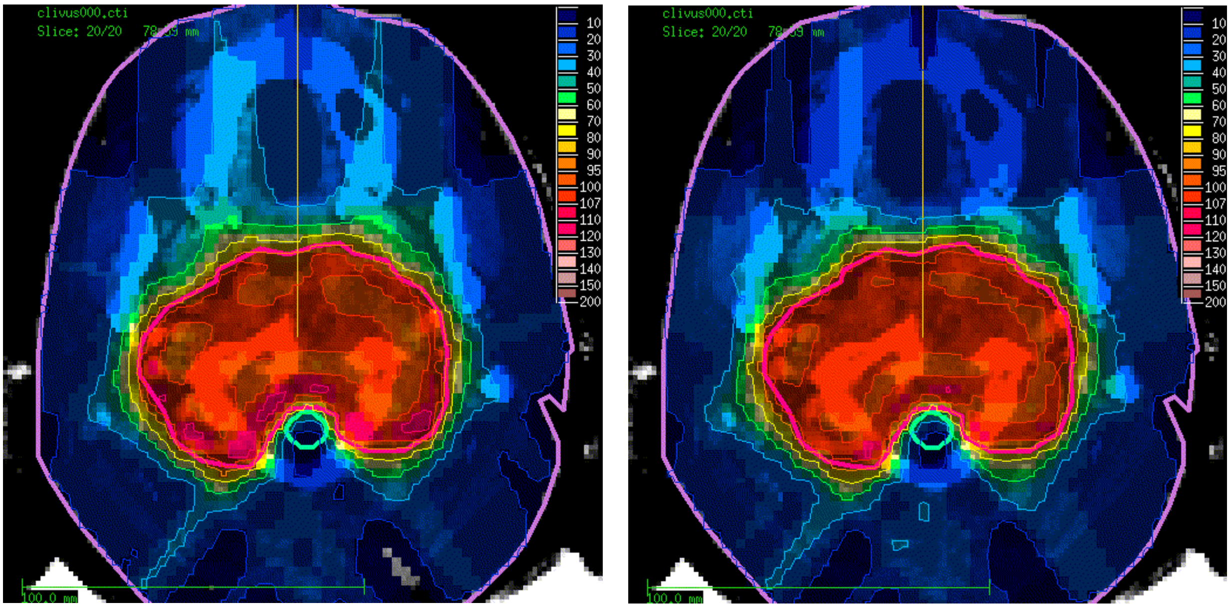

Figure 5.9: *Distributions of the product of RBE and dose in a transversal slice through the isocentre for the normal dose optimization (left) and for the new RBE optimization (right), both for the 3D modulation technique. The colour scales are normalized to* 100% = 2 *CGE per fraction.*

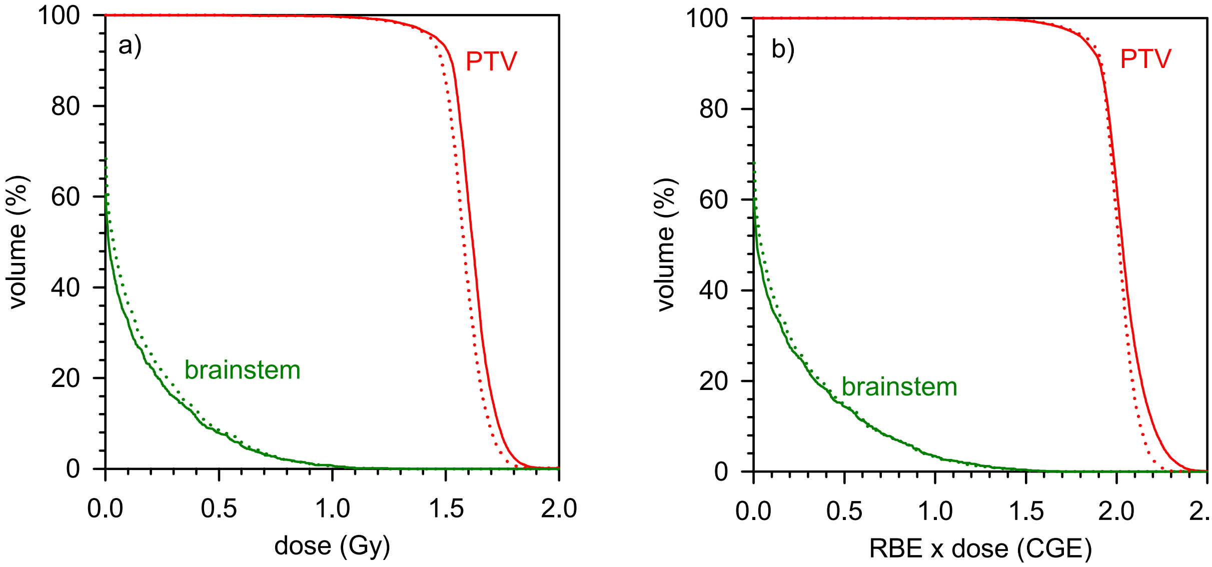

Figure 5.10: *Dose-volume-histograms for the two 3D modulation plans for the clivus chordoma. The DVHs of the PTV (red) and the brainstem (green) are given for the physical dose (a) and for the product of RBE and dose (b). The solid lines correspond to the dose optimization (optimized to yield 1.6 Gy per fraction), while the dotted lines show the DVHs for the RBE optimization (optimized to 2 CGE per fraction).*

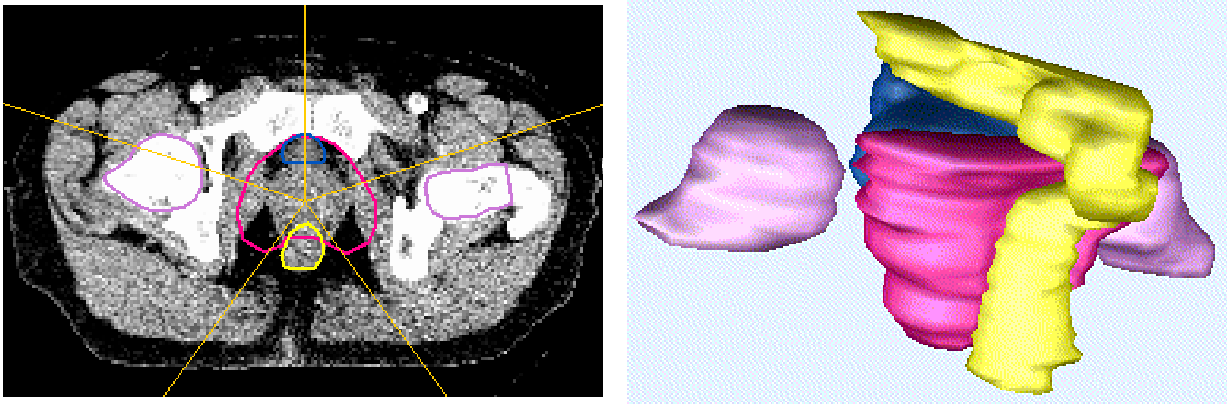

Figure 5.11: *Left: Transversal CT slice through the isocentre for the patient with the prostate carcinoma. The planning target volume (PTV) and the rectum are given by the red and yellow lines, while the bladder and the heads of the femoral bones are outlined in blue and violet, respectively. The five incident beam directions are given by the yellow lines. Right: Three-dimensional view of the PTV (red) and the surrounding organs at risk.*

Organ	$\boldsymbol{D}_{\mathbf{min}}$	$\boldsymbol{\nu}_{\mathbf{min}}$	$\boldsymbol{D}_{\mathbf{max}}$	$\boldsymbol{\nu}_{\mathbf{max}}$
PTV	66 CGE	40	66 CGE	10
rectum	—	—	45 CGE	4
bladder	—	—	45 CGE	4
femoral heads	—	—	30 CGE	2
normal tissue	—	—	35 CGE	3

Table 5.4: *Optimization constraints (minimum dose, maximum dose and the respective penalty factors, cf equation (2.5)) for the prostate carcinoma case.*

5.3.2.2 Clinical case 2: prostate carcinoma

Anatomy and clinical objectives As a second example, I will present a patient with a carcinoma of the prostate. The anatomy of this case is shown in figure 5.11. The planning target volume (PTV) is situated in the pelvis and is closely surrounded by rectum and bladder as the most important organs at risk. The heads of the femoral bones are also outlined as organs at risk. Again, five coplanar equally spaced beam directions were chosen as indicated in figure 5.11. Here the beam energies ranged from 160 MeV up to 250 MeV. Using a lateral distance of 5 mm between the individual beam spots led to a total of 1183 beams spots for the DET technique.

The objectives of the planning process were to deliver a homogeneous dose of 66 CGE in 35 fractions to the PTV (i.e. with a dose per fraction of 1.9 CGE, which is a reasonable value

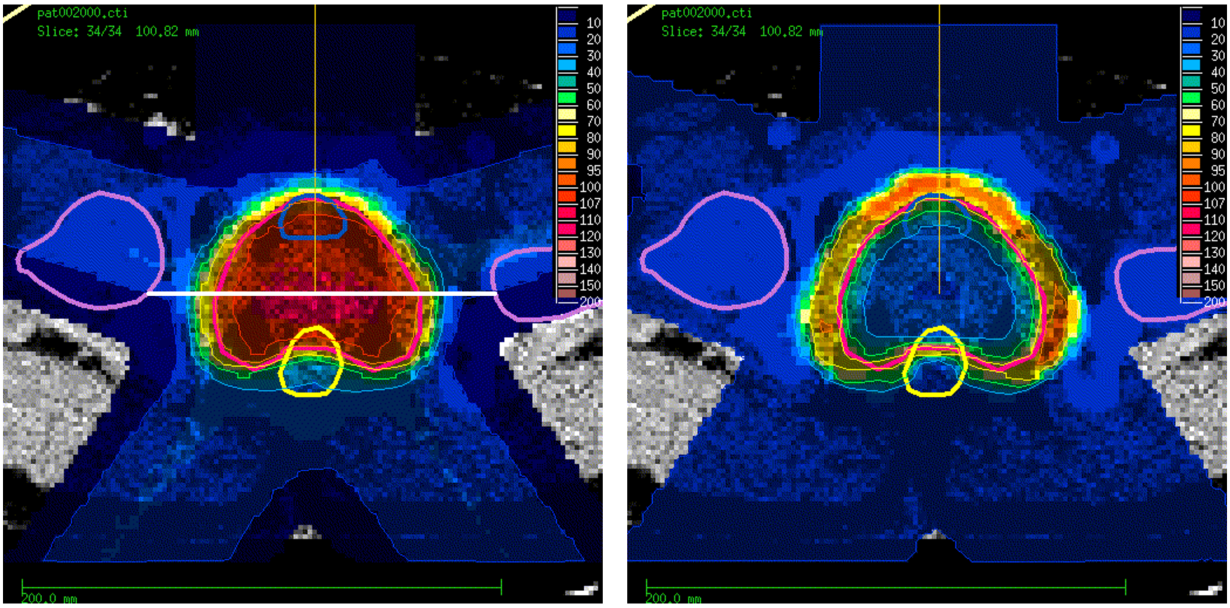

Figure 5.12: *Dose (left) and LET (right) distributions in a transversal slice through the isocentre for the new RBE optimization using the distal edge tracking technique. The colour scales are normalized to* 100% = 1.7 *Gy per fraction and* 100% = 5 *keV/μm, respectively. Profiles along the white horizontal line between the two femoral heads (left side) will be shown in figure 5.15.*

for prostate treatment, cf Rossi 1999). At the same time, the dose to rectum, bladder and femoral heads as well as to the normal tissue had to be limited. In the case of overlapping structures (e.g. PTV and rectum), priority was given to the PTV. The dose constraints used for this case are listed in table 5.4. Again, the constraints are given in units of CGE, i.e. in terms of “photon dose”, which can be directly used for the RBE optimization. For the normal dose optimization, the constraints were converted to proton doses by dividing them by the mean RBE in the PTV, which was in this case 1.11 for distal edge tracking (see below).

As many RBE effects will be similar to those that we already saw for the clivus chordoma case, I will shorten the presentation for the prostate case. In particular, I will show results for the more interesting DET technique only. However, as an additional way of displaying dose, LET and RBE × dose one-dimensional profiles through the three-dimensional cubes will be given, as they are in this case very well suited to elucidate the differences between normal and RBE optimization.

Treatment plans for distal edge tracking Two plans were generated for the optimization constraints given above: one for the normal dose optimization, and a second one

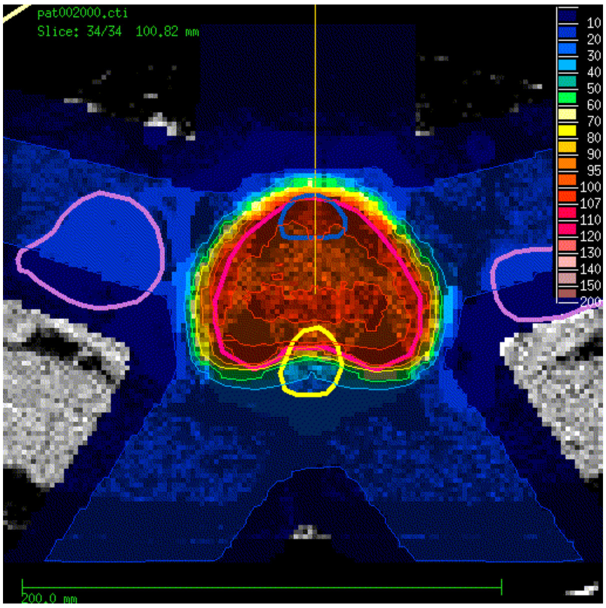

Figure 5.13: *Distribution of RBE × dose in a transversal slice through the isocentre for the new RBE optimization using the distal edge tracking technique. The colour scale is normalized to* 100% = 1.9 *CGE per fraction.*

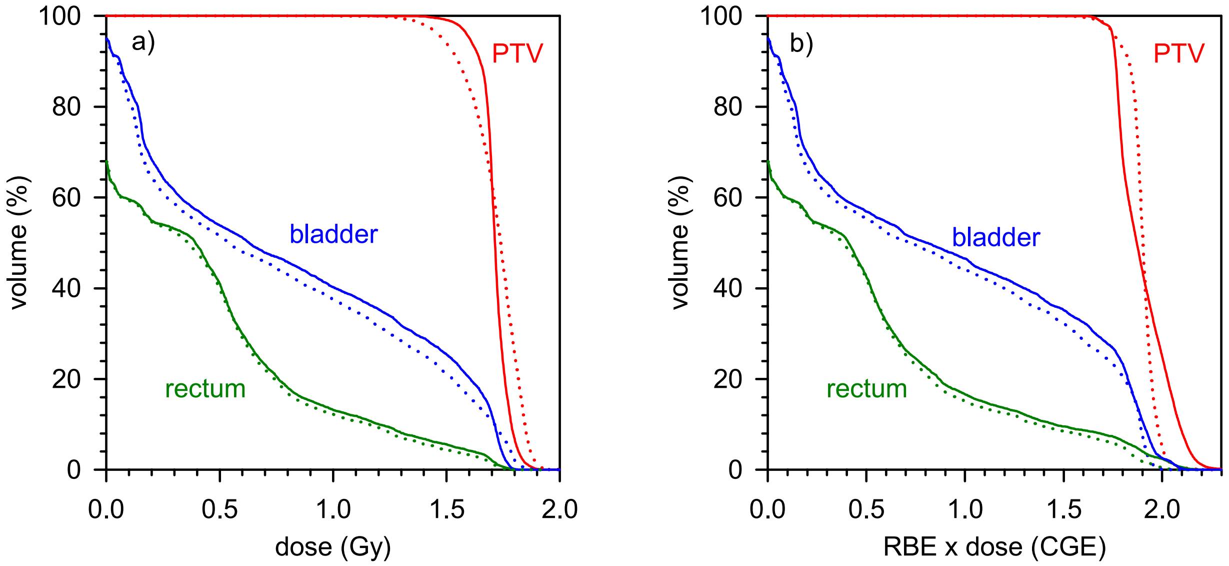

Figure 5.14: *Dose-volume-histograms for the two distal edge tracking plans for the prostate carcinoma. The DVHs of the PTV (red), bladder (blue) and the rectum (green) are given for the physical dose (a) and for the product of RBE and dose (b). The solid lines correspond to the dose optimization (optimized to yield 1.7 Gy per fraction), while the dotted lines show the DVHs for the RBE optimization (optimized to 1.9 CGE per fraction).*

Statistical analysis for the PTV			**Min**	**Max**	**Mean**	$\boldsymbol{\sigma}$
DET dose optimized	dose	(Gy)	1.17	1.97	1.71	0.06
	LET	(keV/μm)	0.9	4.8	1.8	0.8
	RBE × dose	(CGE)	1.42	2.39	1.90	0.13
DET RBE optimized	dose	(Gy)	1.01	1.97	1.71	0.12
	LET	(keV/μm)	0.9	5.3	1.8	0.8
	RBE × dose	(CGE)	1.31	2.26	1.90	0.07

Table 5.5: *Statistical analysis of dose, LET and RBE × dose distributions per fraction in the PTV for the two treatment plans for the prostate carcinoma. For every case, the minimum and maximum values as well as the mean and the standard deviation are given.*

for the RBE optimization. Two-dimensional distributions of dose, LET and RBE × dose are given in figures 5.12 and 5.13 for the RBE optimization only. The respective distributions for the normal dose optimization look very similar on colourwash displays and are therefore not shown separately. The differences between the two plans can be observed better in dose-volume-histograms and in one-dimensional profiles (see below).

As already seen for the clivus chordoma case, the LET distribution for the DET technique shows low LET values in the middle of the PTV and higher LET values at the edges and outside of the PTV (right hand side in figure 5.12). This behaviour does not change much if one uses either normal or RBE optimization. The distribution of RBE × dose (figure 5.13) was homogeneous in the PTV and well shaped to its contour. The mean RBE in the PTV was 1.11 in this case.

By comparing the dose optimized and the RBE optimized plans in dose-volume-histograms (figure 5.14), it becomes apparent that RBE × dose in the PTV is more homogeneous for the RBE optimization than for the dose optimization, as is was also observed in the clivus chordoma case. The DVHs for RBE × dose of bladder and rectum are also slightly better for the RBE optimization (figure 5.14b). On the other hand, the physical dose distribution in the PTV becomes less uniform (figure 5.14a), because the RBE optimization algorithm gives more dose in the middle of the PTV, where LET and RBE are low, and less dose at the PTV edge, where LET and RBE increase. This can be clearly seen in the dose profiles through the PTV given in figures 5.15a and 5.15c. It leads to a more homogeneous profile of RBE × dose and survival as depicted in figures 5.15b and 5.15d. A further comparison of the two plans can be found in table 5.5, where minimum and maximum values as well as the mean and the standard deviation are given for physical dose, LET and RBE × dose.

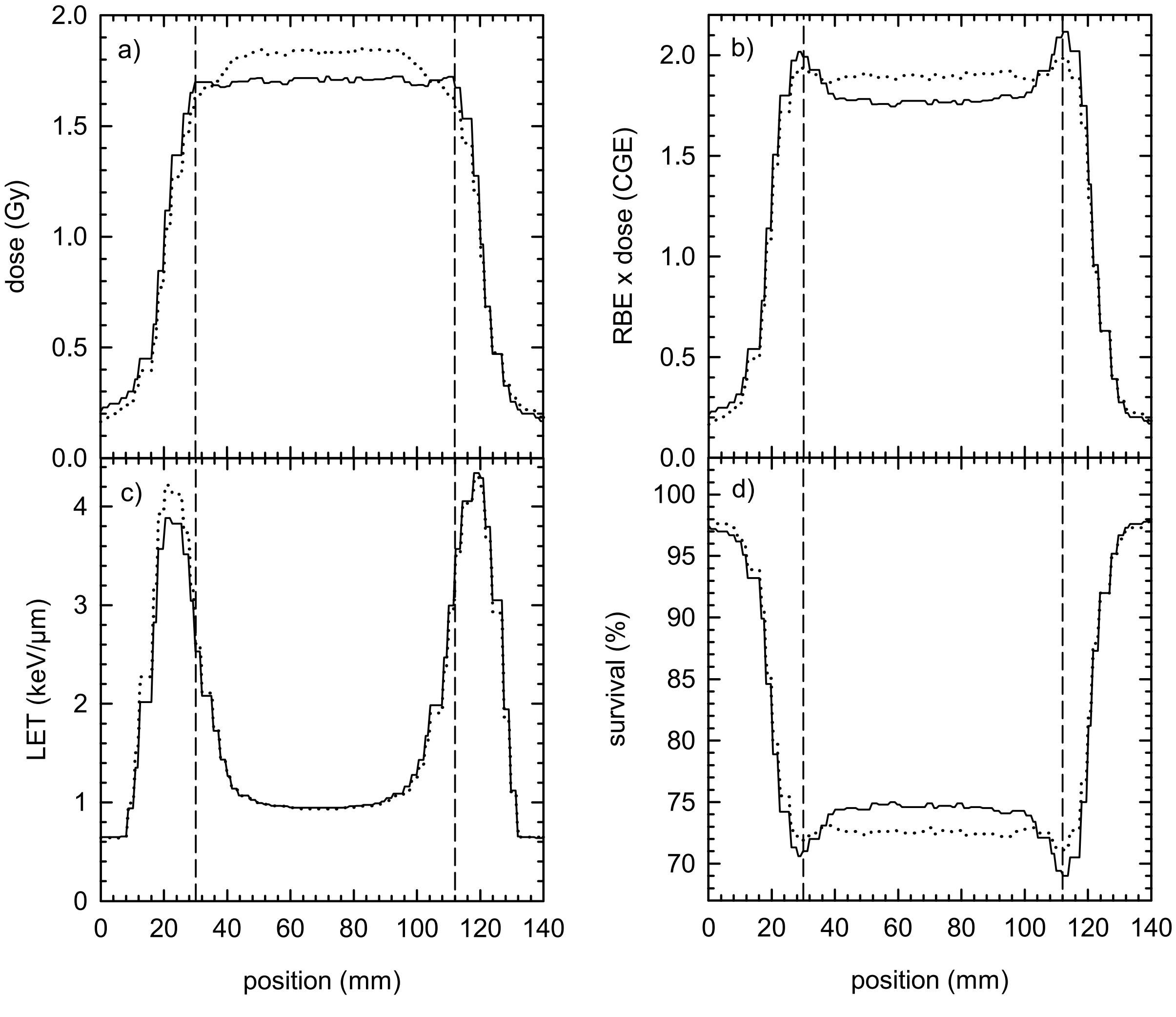

Figure 5.15: *One-dimensional profiles of dose (a), RBE × dose (b), LET (c) and the surviving fraction (d) for the normal dose optimization (——) and the RBE optimization (······). The profiles were measured along the white line indicated in figure 5.12; the position of the PTV is marked by the dashed vertical lines. All values are given per fraction.*

Technique	**Objective function**	**Optimization time** clivus chordoma	 prostate carcinoma
DET	normal dose optimization	170 s	320 s
DET	RBE optimization	370 s	870 s
3D	normal dose optimization	930 s	—
3D	RBE optimization	2600 s	—

Table 5.6: *Optimization times for all treatment plans for the clivus chordoma case and the prostate carcinoma case presented in the previous sections. The calculations were done on a DEC Alpha workstation (500 MHz).*

5.3.2.3 Calculation times

Table 5.6 gives the calculation times that were needed for the optimization of the treatment plans given in the previous sections. All calculations were done on a DEC Alpha workstation (500 MHz) and will be faster on modern GHz computers. These times are for the pure optimization, i.e. excluding the time needed to create and fill the D_{ij} and L_{ij} matrices. This took another 50 (940) seconds for the DET (3D modulation) plans for the clivus chordoma, and 250 seconds for the prostate DET plans. Depending on the case and the scanning technique, the RBE optimization therefore takes roughly a factor of 2–3 longer than the conventional dose optimization.

5.4 Discussion

In this chapter, new objective functions were developed that can account for LET and RBE effects in the optimization process. They were applied to the optimization of SOBPs, and to inverse planning for intensity modulated proton therapy with scanning techniques. The proposed method for "RBE optimization" allows simultaneous multi-field optimization of the biological effect, i.e. of the product of a variable RBE and dose in a reasonable time, and is therefore well suited for studying the influence of a variable RBE in IMPT.

5.4.1 The effects of a variable RBE in SOBPs and IMPT

For the chosen tissue parameters (i.e. for cell survival *in vitro*), the RBE strongly depends on the LET. The most important differences between dose and RBE × dose were therefore found in regions that were exposed to a) high LET (leading to elevated RBE values) and at the same time to b) high or at least intermediate doses (as otherwise the product of RBE and dose would still be low). These conditions can be found in the distal parts of SOBPs, and for scanning techniques at the PTV border and in the region of the dose gradient surrounding the PTV. To compensate for this effect, it is in most cases not possible to change the LET distributions for a given irradiation technique, as the LET of a single beam spot does not (unlike the dose) depend on its weight. It is therefore the physical dose that has to be modified if a uniform biological effect is desired.

5.4.1.1 Optimization of spread-out Bragg peaks

While homogeneous dose and LET distributions simultaneously can be achieved for two opposing SOBPs (figure 5.2), this is not possible for a single SOBP (cf figure 5.1). However, the biological effect in a single SOBP can be made uniform by lowering the dose in the distal part of the SOBP, as shown in figure 5.3. This effect has been known for a long time (e.g. Blakely 1994, Paganetti and Schmitz 1996, Paganetti 1998), although in most clinical applications it is only exploited for heavier charged particles (e.g. Chen et al. 1979, Kanai et al. 1999, Schaffner et al. 2000, Krämer and Scholz 2000). The RBE model and the objective function presented in this work provide for an easy method to obtain these isoeffective SOBPs for protons.

5.4.1.2 Optimization of IMPT

It was found that the effects of a variable RBE in IMPT depend on the type of scanning technique used. As it was expected from the different LET distributions (cf chapter 3), the impact of a variable RBE is much smaller for 3D modulation than for the DET technique.

The 3D modulation technique shows a more or less homogeneous LET within the PTV, which leads to a relatively uniform RBE distribution. Applying the new RBE optimization instead of the dose optimization can still improve the homogeneity of RBE × dose slightly (figure 5.10). On the other hand, the LET distribution for DET is far less homogeneous in the PTV. This leads to considerable RBE variations and to elevated levels of the biological effect at the border of the PTV when using the normal dose optimization (cf figure 5.6). The mean RBE in the PTV was smaller than for the 3D modulation, and the homogeneity of RBE × dose was much worse than one would expect from the variations of the physical dose using a constant RBE of 1.1. However, these unfavourable effects can be overcome by the new RBE optimization, where the physical dose is modulated depending on the local LET to yield a uniform biological effect and survival level across the PTV (as in figure 5.15). Nevertheless, for the chordoma case the dose optimized 3D modulation plan was still slightly better in RBE × dose than the RBE optimized DET plan (table 5.3).

For both scanning techniques, the differences between the two optimization methods were mainly found in the PTV, whereas organs at risk were not much affected when switching from dose optimization to the RBE optimization. This can be understood qualitatively because it is the PTV region where the optimization algorithm has most degrees of freedom in increasing or decreasing the dose depending on the local LET. In organs at risk, one would always want to keep the physical dose as low as possible anyway, and there is not much room for the RBE optimization to reduce the dose further.

5.4.2 Limitations of the RBE optimization

Although the RBE variations observed in the previous sections qualitatively agree with the current knowledge of radiobiology, the resulting RBE distributions have to be considered with great care. In particular, they should not be interpreted as absolute RBE values for the respective clinical case, but rather as a study of relative effects. This is mainly due to the fact that tissue parameters for V79 cells *in vitro* were used instead of any more relevant data sets for clinical tissue types *in vivo*. Thus the RBE values given in this work almost certainly overestimate the real situation (cf section 4.4), at least in the PTV. This might not hold for organs at risk, where non-lethal endpoints like mutations or chromosome aberrations can be more important than survival. The problem how to obtain better parameter sets was already discussed in section 4.4. A next step towards more realistic situations could be to use three sets of tissue parameters, i.e. one for the PTV, one for all organs at risk and one set for normal tissue. In that case, the distribution of RBE × dose would not be “smooth” anymore, instead there would be discontinuities at the boundary between different tissue types — and one would need to carefully address the question what parameters to assign in “overlapping” regions.

One also has to keep in mind the other limitations of the models for LET and RBE that were already discussed in section 3.4 and 4.4, in particular the dose range of the RBE model. It probably does not hold for doses below 1 Gy, where hypersensitivity can occur (Joiner et al. 2001, Schettino et al. 2001). However, the RBE optimization is not affected by this as the dose per fraction in the PTV will in most cases be well above 1 Gy.

Furthermore, the dependency of RBE effects in IMPT on machine specific parameters like the spot size or the energy spectrum of the beam spots was not investigated in this chapter and leaves room for further research. With the methods given in chapter 3, it will be very easy to obtain the required three-dimensional LET distributions for realistic treatment situations in any particular proton facility under consideration.

Chapter 6

Outlook on RBE for Heavy Charged Particles

While the effects of a variable RBE are relatively small in proton beams, they become essential in hadrontherapy with heavier particles, e.g. for carbon beams. For the latter, clinical RBE values are of the order of 2–3 rather than 1.1, and neglecting their spatial variation would lead to unacceptable results. Therefore the question arises whether the methods presented in this work for protons can be applied to other ions as well, where the clinical need for biologically optimized treatment plans is much higher.

Although light ions like helium, lithium or beryllium also promise therapeutical advantages (e.g. Brahme 2004) and require careful RBE calculations (cf Tilly 2002), I will focus on carbon beams, because they are clinically used at several centres. At the carbon ion facility of the Gesellschaft für Schwerionenforschung (GSI) in Darmstadt, three-dimensional RBE distributions calculated with the local effect model (Scholz and Kraft 1994, Scholz et al. 1997) are taken into account during treatment planning and optimization (Jäkel and Krämer 1998, Jäkel et al. 1999, Krämer and Scholz 2000). However, besides requiring long optimization times their system does not allow for real multi-field optimization. Instead, every field has to be optimized individually, before they are added up in a final nonlinear calculation step (Krämer 2001). Somewhat easier methods of determining the RBE (e.g. Kanai et al. 1997, 1999, Schaffner et al. 2000) are employed in Japan, where patients are also treated with carbon beams.

If the algorithms for LET and RBE calculations (cf chapters 3 and 4) could be successfully transferred to heavier ions, the optimization strategies presented in chapter 5 would offer a very fast method for simultaneous multi-field optimization of the biological effect in heavy ion beams. In this chapter, I will therefore briefly describe how LET and RBE could be obtained for carbon ions, and I will illustrate in particular the problems that are encountered and have to be solved in this approach.

6.1 LET calculations for carbon beams

As far as Coulomb interactions are concerned, the LET calculations can be transferred easily from protons to carbon ions by appropriate scaling of the stopping powers. In first approximation, the range R_{ion} of an ion with atomic number Z and mass number A is A/Z^2 times the range of a proton of the same velocity, i.e. with the same energy per nucleon (Raju 1980, p 195). Using the range energy relation $R_{\mathrm{proton}} = \alpha E^p$ from equation (2.2), we get

$$R_{\mathrm{ion}}(E) = \frac{A}{Z^2} \cdot R_{\mathrm{proton}}(E/A) \overset{(2.2)}{=} \frac{A}{Z^2} \cdot \alpha(E/A)^p = \frac{A^{1-p}}{Z^2} \cdot R_{\mathrm{proton}}(E). \tag{6.1}$$

This means the analytical expressions for dose (cf Bortfeld 1997) and LET (chapter 3) can be used for other particles than protons if α is substituted by $\alpha A^{1-p}/Z^2$, i.e. by 9.02×10^{-6} cm MeV^{-p} for carbon ions ($Z = 6$, $A = 12$).

Using this modified α parameter and appropriate values for the width σ_E of the energy spectrum (taking into account beam modifying devices like ripple filters, cf Weber and Kraft 1999), depth dose curves for pristine carbon Bragg peaks can be obtained which compare well to experimental data in the entrance region as well as in the Bragg peak. However, this model can obviously not describe the dose due to nuclear fragments originating in nonelastic nuclear interactions and projectile fragmentation. As these secondaries can have greater ranges than the primary carbon ions, they cause considerable dose values behind the primary peak, the so-called “tail”. For any practical applications, this tail needs to be modeled adequately.

The resulting distribution of the dose averaged linear energy transfer for carbon ions looks qualitatively very similar to the proton LET curve (cf figure 2.1), although the absolute values are approximately a factor of $Z^2 = 36$ higher. For depths up to the Bragg peak, these values agree reasonably well with the measured LET distribution for a carbon beam given by Kanai et al. (1997). However, behind the peak the total LET over all particles is (like the dose) dominated by the nuclear fragments. As the latter are lighter than carbon, their stopping powers are smaller than those from the stopping primary particles in the peak. Therefore the measured LET shows a steep falloff behind the Bragg peak, which cannot be obtained by scaling the proton LET. This means that one either has to include the fragments into the analytical LET model, or that the LET distributions have to be taken from Monte Carlo simulations that account for hadronic interactions.

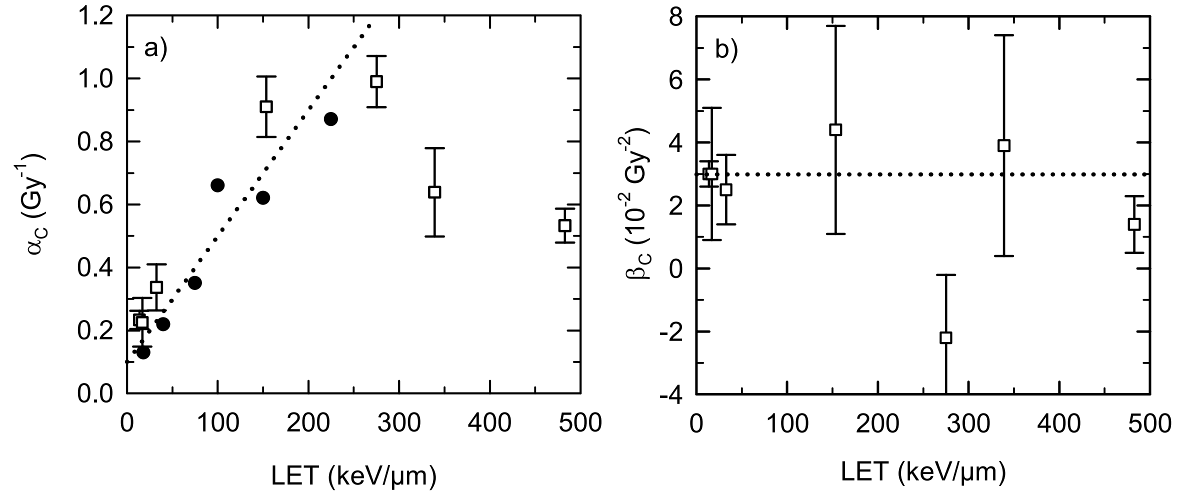

Figure 6.1: *Experimental results for the LQ parameters α_C and β_C as a function of LET for the survival of V79 Chinese hamster cells in vitro under irradiation with carbon ions (cf figure 4.1): (a) α_C vs. LET, (b) β_C vs. LET (● Kanai et al. 1997, □ Weyrather et al. 1999). In (a), a linear fit according to equation (6.2) with $\alpha_{C,0} = 0.1$ Gy^{-1} and $\lambda_C = 0.004$ µm keV^{-1} Gy^{-1} was added, while the dotted line in (b) corresponds to a constant β_C of 0.0298 Gy^{-2}.*

In principle, the LET distributions could be precalculated with Monte Carlo techniques for any desired beam energy, although the high number of possible beam energies for synchrotron installations with active energy variation makes an analytical approach more desirable.

Nevertheless, it certainly requires further investigation whether it makes sense to use a dose averaged LET for different particle species, i.e. averaging the stopping powers of primary carbon ions with secondary fragments like protons or alpha particles. For the RBE calculations it might be necessary to keep separate LETs for every particle type, or to use LET spectra instead of the dose averaged mean. Furthermore, the lateral behaviour of the LET as described in section 3.2.2 for protons has to be studied for carbon ions as well.

6.2 RBE modeling for carbon beams

To apply the phenomenological RBE model to carbon beams, experimental data for the LQ parameters α_C and β_C as a function of LET are needed (cf chapter 4). Again, I will concentrate on V79 cells, although there are also extensive data for human cell lines (e.g.

Suzuki et al. 2000). From the data shown in figure 6.1, it seems that a linear function for the dependence of α_{C} on LET can be used for carbon as well, i.e.

$$\alpha_{\mathrm{C}}(L) = \alpha_{\mathrm{C},0} + \lambda_{\mathrm{C}} L. \tag{6.2}$$

The best fit parameters were $\alpha_{\mathrm{C},0} = 0.1$ Gy^{-1} and $\lambda_{\mathrm{C}} = 0.004$ μm keV^{-1} Gy^{-1}, while a constant value for $\beta_{\mathrm{C}} = \beta_{\mathrm{x}} = 0.0298$ Gy^{-2} can be assumed. Using these parameters and $\alpha_{\mathrm{x}} = 0.112$ Gy^{-1} as in the previous chapters results in RBE values between 2 and 3 (at 2 Gy carbon dose) in the LET region found in SOBPs (∼75–150 keV/μm, Kanai et al. 1997), which are reasonable values for carbon ions.

An important issue that needs further clarification is the maximum LET value that is relevant in therapeutical carbon beams, i.e. whether it is enough to model the linear increasing part of the α_{C} vs. LET relation, as it was the case for protons (cf section 4.2). If, on the other hand, the decreasing part beyond the maximum becomes important, then the argument from section 4.2.3 does no longer hold that α as a linear function of the dose averaged LET is equivalent to the established model of a dose averaged α for mixed LET irradiations (Zaider and Rossi 1980, Kanai et al. 1997).

The most critical point is certainly the influence of the nuclear fragments on the RBE, which cannot be neglected. Therefore the relative contributions of all individual particle species to dose and LET have to be known (from Monte Carlo simulations or measurements, cf Matsufuji et al. 2003), and their effect on RBE × dose needs to be investigated similarly to a study by Paganetti (2002), where the influence of secondary particles in proton beams was examined. This could help to identify the biologically most important particle types, which subsequently have to be integrated into the LET calculations and the phenomenological RBE model.

Nevertheless, this will require a concept to describe how the biological effects of different particles add up nonlinearly in a mixed radiation field, and the total dose averaged LET alone might not be sufficient for this approach, for example because the measured $\alpha(LET)$ curves are in most cases particle specific. However, if a relatively simple model for the RBE in carbon beams can be found, then the optimization strategies presented in chapter 5 will offer a fast tool to study RBE effects in inverse planning for carbon ions.

Chapter 7

Summary and Conclusions

Before some final conclusions are drawn, I will briefly recapitulate the main parts of this work. In order to study and to optimize the biological effects of a variable RBE in intensity modulated proton therapy, fast models for three-dimensional LET and RBE calculations were developed, and a new strategy was presented to utilize this information in inverse therapy planning.

In chapter 3, a fast algorithm for three-dimensional calculations of the dose averaged LET as a measure of the local radiation quality was derived, which offers the possibility of obtaining LET distributions on computed tomography (CT) data sets for any desired irradiation geometry (Wilkens and Oelfke 2004). It is based on an analytical expression for the LET along the central axis of a single beam spot (Wilkens and Oelfke 2003) and on the assumption of a laterally constant LET, which was motivated by Monte Carlo simulations. The algorithm was applied to clinical treatment plans and revealed considerable differences in the LET distributions depending on the chosen scanning technique, even if the dose distributions were very similar. Besides being used for RBE calculations, the LET distributions might have applications in predicting the response of LET dependent dosimetry systems (e.g. gel dosimetry or alanine detectors).

In a second step, a phenomenological model for the RBE in therapeutical proton beams was developed in chapter 4. It describes the RBE as a function of dose, LET and tissue specific parameters in the framework of the linear-quadratic model of radiobiology, and it can reproduce the basic experimental results from cell survival measurements. The model was applied to spread-out Bragg peaks (SOBPs), where the main effects of a variable RBE are an increase of the RBE along the SOBP plateau and a shift in depth of the distal falloff. The new method allows fast RBE estimations and is therefore well suited for the purpose of this work, i.e. for the evaluation of RBE effects in inverse treatment planning.

In chapter 5, new objective functions were presented that utilize the LET and RBE information within the optimization loop of the inverse planning process. Instead of the "normal" optimization of the physical dose, they allow the optimization of dose and LET, or — most promising — the direct optimization of the biological effect in terms of RBE × dose ("RBE optimization"). These new optimization strategies were applied to SOBPs as well as to treatment plans for scanning techniques, where they provide a method for simultaneous multi-field optimization of the biological effect in intensity modulated proton therapy. In its current form, the RBE optimization takes approximately two to three times longer than the conventional optimization of the physical dose, which makes it still feasible for practical applications.

Finally, a brief outlook on the transferability of these concepts from protons to heavier ions like carbon was given in chapter 6. For the latter, the consideration of a variable RBE is essential for treatment planning, which makes a fast method for biological optimization very desirable. However, this requires further investigation as the biological effects in such beams are more complicated, mainly due to the fragmentation of the projectiles.

In short, the main conclusions can be summarized in four major points: (1) The LET distributions for IMPT treatment plans can vary significantly depending on the chosen scanning technique. (2) This influences the biological effect, which in certain situations (e.g. for distal edge tracking) can become considerably worse than one would expect using a constant RBE. (3) To evaluate these effects for a given treatment plan, the methods for LET and RBE calculations presented in this work provide tools for fast identification of potentially dangerous situations, e.g. regions of elevated or depleted LET. (4) Additionally, unfavourable RBE effects can be compensated for by direct optimization of the product of RBE and dose using new strategies that integrate the RBE into the optimization loop.

(1) LET variations The LET within a proton beam shows a steep increase at the end of its range. This leads to significant differences of the LET distributions depending on the scanning technique, although the corresponding dose distributions are very similar. While the 3D modulation shows a more or less homogeneous LET within the planning target volume (PTV), lower LET values are found in the centre of the PTV for distal edge tracking. At the same time, the border of the PTV and the surrounding tissue are exposed to much higher LET levels.

(2) Influence on the biological effect The LET variations lead to variations in the biological effect, i.e. in the distribution of RBE × dose. The consequences of a variable

RBE are therefore most important in the regions of elevated LET. This means that in some situations — depending on the individual case and the scanning technique — the deviations from a constant RBE can become potentially dangerous, for example at the PTV border for the distal edge tracking technique or if Bragg peaks are placed very close to critical structures. In other situations, however, the effects of a variable RBE are small, and the use of a constant RBE is sufficient. Consequently, it is not possible to give a general answer regarding the impact of RBE variations in proton therapy, as it depends on the patient and the individual treatment plan. Nevertheless, if distal edge tracking shall be employed, one should certainly be more concerned about RBE issues than for the 3D modulation. The latter is definitely the safer option if no reliable RBE calculations are available. In any case, the physical dose should not be the only criterion for comparing treatment plans for different scanning techniques with protons.

(3) Evaluation tools To clarify the situation, tools were developed that allow the fast evaluation of potential RBE effects for a treatment plan under consideration. First, three-dimensional LET calculations can locate high and low LET regions, which are physical properties of the radiation field. Secondly, if appropriate biological parameters are available, one can employ the phenomenological RBE model to compute a three-dimensional distribution of RBE × dose to estimate the biological effects of the observed LET variations. Even if the tissue parameters are not precisely known, one can obtain qualitative statements, e.g. where RBE effects are important, or simulate a worst case scenario.

(4) Optimization strategies If the evaluation of RBE effects reveals that a certain treatment plan is not satisfactory from the biological point of view, one can either change the setup for the plan, i.e. modify the beam directions or the scanning technique, or one can employ the objective functions from chapter 5 to obtain an optimized distribution of the biological effect. As the LET distribution for a given irradiation setup cannot be changed extensively in most cases, the physical dose in the PTV must become inhomogeneous in order to achieve a uniform biological outcome. The methods presented in this work provide a feasible solution for such biological optimization, which can be implemented in clinical practice as soon as reliable and appropriate tissue parameters have been derived. Especially for DET, there seems to be a high potential in this approach, which can combine the technical advantages of DET with an optimized distribution of the biological effect. On the other hand, only slight improvements may be gained for the 3D modulation technique, because its biological properties can be satisfying even for the normal optimization of the physical dose.

The points mentioned above include some implications for practical treatment planning. If a variable RBE shall be used, the prescribed dose per fraction has to be known before the RBE calculations or the RBE optimization are carried out, as the RBE model is based on dose per fraction. Nonlinear effects prohibit a simple rescaling of RBE × dose to a new prescription later on. Moreover, appropriate visualization tools are required to display the distributions of LET, RBE or RBE × dose in addition to the physical dose. If two (or more) different biological endpoints are of interest for the same organ at risk, one would need even more than one distribution of RBE × dose for that region.

However, one has to keep in mind that the RBE model used in this work has several limitations, and the accurate prediction of absolute RBE values for clinically relevant situations is very difficult. Since it is a phenomenological model, it cannot be better than the experimental data that are used to derive its tissue parameters. Currently such data for the relevant endpoints are scarce and there is certainly a clear need for more radiobiological measurements in proton beams, especially for *in vivo* systems (Paganetti et al. 2002, Paganetti 2003). Preferably, such studies should use realistic doses (1–3 Gy per fraction) and explore several positions along the Bragg curve or the SOBP including the high LET region at the distal edge in order to determine the LET dependence. Till then, data from *in vitro* measurements as used in this work can be employed to estimate the potential effects of a variable RBE, in particular the elevated RBE values in the distal part of the Bragg curve. Independently of the tissue parameters, the calculation or even optimization of three-dimensional LET distributions can help to identify and avoid unfavourable effects in high LET regions.

In this work, radiobiological uncertainties of intensity modulated proton therapy were investigated. It was shown that in some cases RBE effects can become potentially dangerous, which justifies the effort required to detect and compensate for these effects in order to deliver the best possible treatment to the patient. Besides this radiobiological aspect, there are still more challenges for IMPT. Among others, they include the development of adaptive techniques that account for both intra- and interfraction organ motion, methods for quantifying and minimizing adverse effects due to range uncertainties and last but not least further advances in hardware components and quality assurance procedures. Nevertheless, intensity modulated proton therapy — if carefully administered — carries high potential for improved clinical results for tumour patients in radiotherapy.

Appendix A

Derivation of the Analytical LET Model

In this appendix, analytical expressions for LET distributions along the central axis of proton beams in water are derived (cf section 3.2.1.1). The derivation follows closely the work by Bortfeld (1997), in which an analytical approximation for the depth dose curve was developed.

To work out the track averaged and dose averaged LET at depth z, we will need the local proton spectrum $\varphi_r(z)$ with respect to the residual range r and the stopping powers $\overline{S}_R(r)$ and $\overline{S_R^2}(r)$ (cf section 3.2.1.1). Expressions for these terms were already given in equations (3.11), (3.16) and (3.17), respectively. They can now be used to evaluate the three integrals (cf (3.8))

$$\Phi_z = \int_0^\infty \varphi_r(z)\mathrm{d}r, \quad \langle S\rangle_z = \int_0^\infty \varphi_r(z)\overline{S}_R(r)\mathrm{d}r \quad \text{and} \quad \langle S^2\rangle_z = \int_0^\infty \varphi_r(z)\overline{S_R^2}(r)\mathrm{d}r. \tag{A.1}$$

To solve these integrals we employ the parabolic cylinder functions $\mathcal{D}_\nu(x)$ (Gradshteyn and Ryzhik 1994, Abramowitz and Stegun 1972). They obey the equation

$$\int_0^\infty r^{-\nu-1}\mathrm{e}^{-(r-s)^2/2\sigma^2}\mathrm{d}r = \mathrm{e}^{-s^2/4\sigma^2}\sigma^{-\nu}\Gamma(-\nu)\mathcal{D}_\nu(-s/\sigma) \qquad (\nu < 0), \tag{A.2}$$

where $\Gamma(x)$ is the gamma function.

Let us first consider Φ_z. Inserting $\varphi_r(z)$ from (3.11) yields

$$\Phi_z = \int_0^\infty \varphi_r(z)\mathrm{d}r = \frac{\Phi_0}{\sqrt{2\pi}\sigma}\int_0^\infty \mathrm{e}^{-(r-R_0+z)^2/2\sigma^2}\mathrm{d}r. \tag{A.3}$$

By using (A.2) and $\zeta := (z - R_0)/\sigma$ we get

$$\Phi_z = \frac{\Phi_0}{\sqrt{2\pi}\sigma} \mathrm{e}^{-\zeta^2/4} \sigma \Gamma(1) \mathcal{D}_{-1}(\zeta) = \frac{\Phi_0}{\sqrt{2\pi}} \mathrm{e}^{-\zeta^2/4} \mathcal{D}_{-1}(\zeta), \tag{A.4}$$

as $\Gamma(1) = 1$. For $\langle S \rangle_z$, the stopping power from (3.16) is inserted into (A.1):

$$\begin{aligned} \langle S \rangle_z &= \frac{\Phi_0}{\sqrt{2\pi}\sigma R \alpha^{1/p}} \int_0^\infty \mathrm{e}^{-(r-R_0+z)^2/2\sigma^2} \left[(r+R)^{1/p} - r^{1/p} \right] \mathrm{d}r \qquad \text{(A.5)} \\ &= \frac{\Phi_0}{\sqrt{2\pi}\sigma R \alpha^{1/p}} \Big[\int_0^\infty \mathrm{e}^{-(r-R_0+z)^2/2\sigma^2} (r+R)^{1/p} \mathrm{d}r - \int_0^\infty \mathrm{e}^{-(r-R_0+z)^2/2\sigma^2} r^{1/p} \mathrm{d}r \Big]. \end{aligned}$$

With (A.2), the second integral yields $\mathrm{e}^{-\zeta^2/4}\sigma^{1+1/p}\Gamma(1+1/p)\mathcal{D}_{-1-1/p}(\zeta)$. In the first integral we can substitute $u := r + R$:

$$\begin{aligned} \int_0^\infty \mathrm{e}^{-(r-R_0+z)^2/2\sigma^2} (r+R)^{1/p} \mathrm{d}r &= \int_R^\infty \mathrm{e}^{-(u-R-R_0+z)^2/2\sigma^2} u^{1/p} \mathrm{d}u \\ &= \int_0^\infty f(u) \mathrm{d}u - \int_0^R f(u) \mathrm{d}u \qquad \text{(A.6)} \end{aligned}$$

with $f(u) = \mathrm{e}^{-(u-R-R_0+z)^2/2\sigma^2} u^{1/p}$. As R is small and $f(u)$ is not divergent for $u \to 0$, we can approximate $\int_0^R f(u) \mathrm{d}u$ by $Rf(\frac{1}{2}R)$. With (A.2) and $\xi := (z - R_0 - R)/\sigma$ we get

$$\begin{aligned} \int_0^\infty \mathrm{e}^{-(r-R_0+z)^2/2\sigma^2} (r+R)^{1/p} \mathrm{d}r &\approx \int_0^\infty f(u) du - Rf(\tfrac{1}{2}R) \\ &= \mathrm{e}^{-\xi^2/4} \sigma^{1+1/p} \Gamma(1 + \tfrac{1}{p}) \mathcal{D}_{-1-1/p}(\xi) - R(\tfrac{1}{2}R)^{1/p} \mathrm{e}^{-(\zeta+\xi)^2/8}. \qquad \text{(A.7)} \end{aligned}$$

Using $\tilde{\mathcal{D}}_\nu(\xi, \zeta) = \mathrm{e}^{-\xi^2/4}\mathcal{D}_{-\nu}(\xi) - \mathrm{e}^{-\zeta^2/4}\mathcal{D}_{-\nu}(\zeta)$, we therefore obtain

$$\langle S \rangle_z \approx \frac{\Phi_0}{\sqrt{2\pi}\sigma R \alpha^{1/p}} \left[\sigma^{1+1/p} \Gamma(1 + \tfrac{1}{p}) \tilde{\mathcal{D}}_{1+1/p}(\xi, \zeta) - R(\tfrac{1}{2}R)^{1/p} \mathrm{e}^{-(\zeta+\xi)^2/8} \right] \tag{A.8}$$

To calculate $\langle S^2 \rangle_z$, equations (3.17) and (3.11) are inserted into (A.1):

$$\langle S^2 \rangle_z = \frac{\Phi_0}{\sqrt{2\pi}\sigma R \alpha^{2/p} p(2-p)} \int_0^\infty \mathrm{e}^{-(r-R_0+z)^2/2\sigma^2} \left[(r+R)^{2/p-1} - r^{2/p-1} \right] \mathrm{d}r. \tag{A.9}$$

This expression can be evaluated in exactly the same way as (A.5) and leads to

$$\langle S^2 \rangle_z \approx \frac{\Phi_0}{\sqrt{2\pi}\sigma R \alpha^{2/p} p(2-p)} \left[\sigma^{2/p} \Gamma(\tfrac{2}{p}) \tilde{\mathcal{D}}_{2/p}(\xi, \zeta) - 2(\tfrac{1}{2}R)^{2/p} \mathrm{e}^{-(\zeta+\xi)^2/8} \right]. \tag{A.10}$$

The track averaged and dose averaged LET can now be calculated by simply inserting equations (A.4), (A.8) and (A.10) into (3.9).

Bibliography

Abramowitz M. and Stegun I.A. (editors) 1972 *Handbook of Mathematical Functions.* New York: Dover Publications.

Agosteo S., Birattari C., Caravaggio M., Silari M. and Tosi G. 1998 Secondary neutron and photon dose in proton therapy. *Radiother. Oncol.* **48**(3) 293–305.

Ando K., Furusawa Y., Suzuki M., Nojima K., Majima H., Koike S., Aoki M., Shimizu W., Futami Y., Ogino T., Murayama S. and Ikeda H. 2001 Relative biological effectiveness of the 235 MeV proton beams at the National Cancer Center Hospital East. *J. Radiat. Res.* **42**(1) 79–89.

Bäck S.Å.J., Medin J., Magnusson P., Olsson P., Grusell E. and Olsson L.E. 1999 Ferrous sulphate gel dosimetry and MRI for proton beam dose measurements. *Phys. Med. Biol.* **44**(8) 1983–1996.

Barendsen G.W. 1994 The relationships between RBE and LET for different types of lethal damage in mammalian cells: biophysical and molecular mechanisms. *Radiat. Res.* **139**(3) 257–270.

— 1997 Parameters of linear-quadratic radiation dose-effect relationships: dependance on LET and mechanisms of reproductive cell death. *Int. J. Radiat. Biol.* **71**(6) 649–655.

— 2000 RBE as a function of dose for effects on tissues and tumors assessed by the linear-quadratic model (letter). *Int. J. Radiat. Oncol. Biol. Phys.* **46**(3) 684–685.

Belli M., Bettega D., Calzolari P., Cera F., Cherubini R., Dalla Vecchia M., Durante M., Favaretto S., Gialanella G., Grossi G., Marchesini R., Moschini G., Piazzola A., Poli G., Pugliese M., Sapora O., Scampoli P., Simone G., Sorrentino E., Tabocchini M.A., Tallone L. and Tiveron P. 2000 Inactivation of human normal and tumour cells irradiated with low energy protons. *Int. J. Radiat. Biol.* **76**(6) 831–839.

Belli M., Campa A. and Ermolli I. 1997 A semi-empirical approach to the evaluation of the relative biological effectiveness of therapeutic proton beams: the methodological framework. *Radiat. Res.* **148**(6) 592–598.

Belli M., Cera F., Cherubini R., Dalla Vecchia M., Haque A.M.I., Ianzini F., Moschini G., Sapora O., Simone G., Tabocchini M.A. and Tiveron P. 1998 RBE-LET relationships for cell inactivation and mutation induced by low energy protons in V79 cells: further results at the LNL facility. *Int. J. Radiat. Biol.* **74**(4) 501–509.

Belli M., Cera F., Cherubini R., Haque A.M.I., Ianzini F., Moschini G., Sapora O., Simone G., Tabocchini M.A. and Tiveron P. 1993 Inactivation and mutation induction in V79 cells by low energy protons: re-evaluation of the results at the LNL facility. *Int. J. Radiat. Biol.* **63**(3) 331–337.

Belli M., Cherubini R., Finotto S., Moschini G., Sapora O., Simone G. and Tabocchini M.A. 1989 RBE-LET relationship for the survival of V79 cells irradiated with low energy protons. *Int. J. Radiat. Biol.* **55**(1) 93–104.

Berger M.J. 1993 *Penetration of Proton Beams Through Water I. Depth-dose Distribution, Spectra and LET Distribution. NISTIR Publication 5226.* Gaithersburg, MD: National Institute of Standards and Technology.

Bettega D., Birattari C., Bombana M., Fuhrman Conti A.M., Gallini E., Pelucchi T. and Tallone Lombardi L. 1979 Relative biological effectiveness for protons of energies up to 31 MeV. *Radiat. Res.* **77**(1) 85–97.

Bettega D., Calzolari P., Chauvel P., Courdi A., Herault J., Iborra N., Marchesini R., Massariello P., Poli G.L. and Tallone L. 2000 Radiobiological studies on the 65 MeV therapeutic proton beam at Nice using human tumour cells. *Int. J. Radiat. Biol.* **76**(10) 1297–1303.

Bettega D., Calzolari P., Marchesini R., Noris Chiorda G.L., Piazzolla A., Tallone L., Cera F., Cherubini R., Dalla Vecchia M., Favaretto S. and Tiveron P. 1998 Inactivation of C3H10T1/2 cells by low energy protons and deuterons. *Int. J. Radiat. Biol.* **73**(3) 303–309.

Biaggi M., Ballarini F., Burkard W., Egger E., Ferrari A. and Ottolenghi A. 1999 Physical and biophysical characteristics of a fully modulated 72 MeV therapeutic proton beam: model predictions and experimental data. *Nucl. Instrum. Methods B* **159**(1-2) 89–100.

Bichsel H. 1968 Charged particle interactions. In: Attix F.H. and Roesch W.C. (editors), *Radiation Dosimetry*, volume I. Fundamentals, chapter 4, pp 157–228. New York and London: Academic Press, 2nd edition.

Blakely E.A. 1994 Current issues in low- and high-LET medical radiobiology. In: Amaldi U. and Larsson B. (editors), *Hadrontherapy in Oncology. Proc. of the 1st Int. Symposium on Hadrontherapy, Como 1993*, pp 693–701. Amsterdam: Elsevier.

Blomquist E., Russell K.R., Stenerlöw B., Montelius A., Grusell E. and Carlsson J. 1993 Relative biological effectiveness of intermediate energy protons. Comparisons with ^{60}Co gamma-radiation using two cell lines. *Radiother. Oncol.* **28**(1) 44–51.

Bortfeld T. 1997 An analytical approximation of the Bragg curve for therapeutic proton beams. *Med. Phys.* **24**(12) 2024–2033.

Bortfeld T. and Schlegel W. 1996 An analytical approximation of depth-dose distributions for therapeutic proton beams. *Phys. Med. Biol.* **41**(8) 1331–1339.

Brahme A. 2004 Recent advances in light ion radiation therapy. *Int. J. Radiat. Oncol. Biol. Phys.* **58**(2) 603–616.

Bussière M.R. and Adams J.A. 2003 Treatment planning for conformal proton radiation therapy. *Technology in Cancer Research & Treatment* **2**(5) 389–399.

Butts J.J. and Katz R. 1967 Theory of RBE for heavy ion bombardment of dry enzymes and viruses. *Radiat. Res.* **30**(4) 855–871.

Carlsson Å.K., Andreo P. and Brahme A. 1997 Monte Carlo and analytical calculation of proton pencil beams for computerized treatment plan optimization. *Phys. Med. Biol.* **42**(6) 1033–1053.

CERN Application Software Group 1994 *GEANT—Detector Description and Simulation Tool. CERN Program Library Long Writeup W5013.* Geneva: CERN.

Chapman J.D., Blakely E.A., Smith K.C. and Urtasun R.C. 1977 Radiobiological characterization of the inactivating events produced in mammalian cells by helium and heavy ions. *Int. J. Radiat. Oncol. Biol. Phys.* **3** 97–102.

Chen G.T.Y., Singh R.P., Castro J.R., Lyman J.T. and Quivey J.M. 1979 Treatment planning for heavy ion radiotherapy. *Int. J. Radiat. Oncol. Biol. Phys.* **5**(10) 1809–1819.

Courdi A., Brassart N., Hérault J. and Chauvel P. 1994 The depth-dependent radiation response of human melanoma cells exposed to 65 MeV protons. *British Journal of Radiology* **67**(800) 800–804.

Coutrakon G., Cortese J., Ghebremedhin A., Hubbard J., Johanning J., Koss P., Maudsley G., Slater C.R. and Zuccarelli C. 1997 Microdosimetry spectra of the Loma Linda proton beam and relative biological effectiveness comparisons. *Med. Phys.* **24**(9) 1499–1506.

Dale R.G. and Jones B. 1999 The assessment of RBE effects using the concept of biologically effective dose. *Int. J. Radiat. Oncol. Biol. Phys.* **43**(3) 639–645.

Deasy J.O. 1998 A proton dose calculation algorithm for conformal therapy simulations based on Molière's theory of lateral deflections. *Med. Phys.* **25**(4) 476–483.

Deasy J.O., Shepard D.M. and Mackie T.R. 1997 Distal edge tracking: a proposed delivery method for conformal proton therapy using intensity modulation. In: Leavitt D.D. and Starkschall G. (editors), *Proc. 12th Int. Conf. on the Use of Computers in Radiation Therapy*, pp 406–409. Madison: Medical Physics Publishing.

Debus J., Hug E.B., Liebsch N.J., O'Farrel D., Finkelstein D., Efird J. and Munzenrider J.E. 1997 Brainstem tolerance to conformal radiotherapy of skull base tumors. *Int. J. Radiat. Oncol. Biol. Phys.* **39**(5) 967–975.

Denekamp J., Waites T. and Fowler J.F. 1997 Predicting realistic RBE values for clinically relevant radiotherapy schedules. *Int. J. Radiat. Biol.* **71**(6) 681–694.

Fassò A., Ferrari A., Ranft J. and Sala P.R. 1994 FLUKA: present status and future developments. In: Menzione A. and Scribano A. (editors), *Proc. IV Int. Conf. on Calorimetry in High Energy Physics*, pp 493–502. Singapore: World Scientific.

Fassò A., Ferrari A., Ranft J., Sala P.R., Stevenson G.R. and Zazula J.M. 1993 A comparison of FLUKA simulations with measurements of fluence and dose in calorimeter structures. *Nucl. Instrum. Methods A* **332**(3) 459–468.

Folkard M., Prise K.M., Vojnovic B., Newman H.C., Roper M.J. and Michael B.D. 1996 Inactivation of V79 cells by low-energy protons, deuterons and helium-3 ions. *Int. J. Radiat. Biol.* **69**(6) 729–738.

Gardey K.U., Oelfke U. and Lam G.K.Y. 1999 Range modulation in proton therapy—an optimization technique for clinical and experimental applications. *Phys. Med. Biol.* **44**(6) N81–N88.

Gerweck L.E. and Kozin S.V. 1999 Relative biological effectiveness of proton beams in clinical therapy. *Radiother. Oncol.* **50**(2) 135–142.

Goitein M. and Chen G.T.Y. 1983 Beam scanning for heavy charged particle radiotherapy. *Med. Phys.* **10**(6) 831–840.

Goodhead D.T., Belli M., Mill A.J., Bance D.A., Allen L.A., Hall S.C., Ianzani F., Simone G., Stevens D.L., Stretch A., Tabocchini M.A. and Wilkinson R.E. 1992 Direct comparison between protons and alpha-particles of the same LET: I. Irradiation methods and inactivation of asynchronous V79, HeLa and C3H 10T$\frac{1}{2}$ cells. *Int. J. Radiat. Biol.* **61**(5) 611–624.

Gottschalk B., Koehler A.M., Schneider R.J., Sisterson J.M. and Wagner M.S. 1993 Multiple Coulomb scattering of 160 MeV protons. *Nucl. Instrum. Methods B* **74**(4) 467–490.

Gottschalk B., Platais R. and Paganetti H. 1999 Nuclear interactions of 160 MeV protons stopping in copper: A test of Monte Carlo nuclear models. *Med. Phys.* **26**(12) 2597–2601.

Gradshteyn I.S. and Ryzhik I.M.; Jeffrey A. (editor) 1994 *Table of Integrals, Series, and Products.* San Diego: Academic Press, 5th edition.

Gueulette J., Böhm L., Slabbert J.P., De Coster B.M., Rutherfoord G.S., Ruifrok A., Octave-Prignot M., Binns P.J., Schreuder A.N., Symons J.E., Scalliet P. and Jones D.T.L. 2000 Proton relative biological effectiveness (RBE) for survival in mice after thoracic irradiation with fractionated doses. *Int. J. Radiat. Oncol. Biol. Phys.* **47**(4) 1051–1058.

Gueulette J., Slabbert J.P., Böhm L., De Coster B.M., Rosier J.F., Octave-Prignot M., Ruifrok A., Schreuder A.N., Wambersie A., Scalliet P. and Jones D.T.L. 2001 Proton RBE for early intestinal tolerance in mice after fractionated irradiation. *Radiother. Oncol.* **61**(2) 177–184.

Hall E.J. 2000 *Radiobiology for the Radiologist.* Philadelphia: Lippincott, 5th edition.

Hall E.J., Kellerer A.M., Rossi H.H. and Lam Y.P. 1978 The relative biological effectiveness of 160 MeV protons—II. *Int. J. Radiat. Oncol. Biol. Phys.* **4**(11–12) 1009–1013.

Hawkins R.B. 1998 A microdosimetric-kinetic theory of the dependence of the RBE for cell death on LET. *Med. Phys.* **25**(7) 1157–1170.

— 2003 A microdosimetric-kinetic model for the effect of non-Poisson distribution of lethal lesions on the variation of RBE with LET. *Radiat. Res.* **160**(1) 61–69.

Heese J., Kluge H., Fuchs H., Homeyer H., Morgenstern H., Rethfeldt C., Reng I., Nausner M., Bechrakis N., Kreusel K.M., Bornfeld N., Hinkelbein W. and Foerster M.H. 2001 Proton beam eye treatments in Berlin: experiences of the first two years. *Physica Medica* **XVII**(Suppl. 3) 20–22.

Heufelder J., Stiefel S., Pfaender M., Lüdemann L., Grebe G. and Heese J. 2003 Use of BANG polymer gel for dose measurements in a 68 MeV proton beam. *Med. Phys.* **30**(6) 1235–1240.

Holmes T. and Mackie T.R. 1994 A comparison of three inverse treatment planning algorithms. *Phys. Med. Biol.* **39**(1) 91–106.

Hong L., Goitein M., Bucciolini M., Comiskey R., Gottschalk B., Rosenthal S., Serago C. and Urie M. 1996 A pencil beam algorithm for proton dose calculations. *Phys. Med. Biol.* **41**(8) 1305–1330.

ICRP 1989 *RBE for Deterministic Effects (ICRP Publication 58).* Oxford: Pergamon Press.

ICRU 1970 *Linear Energy Transfer (ICRU Report 16).* Washington, D.C.: International Commission on Radiation Units and Measurements.

— 1983 *Microdosimetry (ICRU Report 36).* Bethesda, MD: International Commission on Radiation Units and Measurements.

— 1993 *Stopping Powers and Ranges for Protons and Alpha Particles (ICRU Report 49).* Bethesda, MD: International Commission on Radiation Units and Measurements.

— 1998 *Fundamental Quantities and Units for Ionizing Radiation (ICRU Report 60).* Bethesda, MD: International Commission on Radiation Units and Measurements.

— 1999 *Prescribing, Recording and Reporting Photon Beam Therapy (ICRU Report 62, Supplement to ICRU Report 50).* Bethesda, MD: International Commission on Radiation Units and Measurements.

Jäkel O., Debus J., Krämer M., Scholz M. and Kraft G. 1999 Treatment planning for light ions: how to take into account relative biological effectiveness (RBE). *Strahlenther. Onkol.* **175**(Suppl. II) 12–14.

Jäkel O. and Krämer M. 1998 Treatment planning for heavy ion irradiation. *Physica Medica* **XIV**(Suppl. 1) 53–62.

Johns H.E. and Cunningham J.R. 1983 *The Physics of Radiology.* Springfield, IL: Charles C. Thomas, 4th edition.

Joiner M.C. and Field S.B. 1988 The response of mouse skin to irradiation with neutrons from the 62 MV cyclotron at Clatterbridge, U.K. *Radiother. Oncol.* **12**(2) 153–166.

Joiner M.C., Marples B., Lambin P., Short S.C. and Turesson I. 2001 Low-dose hypersensitivity: current status and possible mechanisms. *Int. J. Radiat. Oncol. Biol. Phys.* **49**(2) 379–389.

Jones B. and Dale R. 2003 The clinical radiobiology of high LET radiotherapy with particular reference to proton radiotherapy. *Clinical Oncology* **15**(1) S16–S22.

Kanai T., Endo M., Minohara S., Miyahara N., Koyama-ito H., Tomura H., Matsufuji N., Futami Y., Fukumura A., Hiraoka T., Furusawa Y., Ando K., Suzuki M., Soga F. and Kawachi K. 1999 Biophysical characteristics of HIMAC clinical irradiation system for heavy-ion radiation therapy. *Int. J. Radiat. Oncol. Biol. Phys.* **44**(1) 201–210.

Kanai T., Furusawa Y., Fukutsu K., Itsukaichi H., Eguchi-Kasai K. and Ohara H. 1997 Irradiation of mixed beam and design of spread-out Bragg peak for heavy-ion radiotherapy. *Radiat. Res.* **147**(1) 78–85.

Kanai T., Kawachi K., Kumamoto Y., Ogawa H., Yamada T., Matsuzawa H. and Inada T. 1980 Spot scanning system for proton radiotherapy. *Med. Phys.* **7**(4) 365–369.

Katz R., Ackerson B., Homayoonfar M. and Sharma S.C. 1971 Inactivation of cells by heavy ion bombardment. *Radiat. Res.* **47** 402–425.

Katz R., Zachariah R., Cucinotta F.A. and Zhang C. 1994 Survey of cellular radiosensitivity parameters. *Radiat. Res.* **140**(3) 356–365.

Kellerer A.M., Hahn K. and Rossi H.H. 1992 Intermediate dosimetric quantities. *Radiat. Res.* **130**(1) 15–25.

Kellerer A.M. and Rossi H.H. 1978 A generalized formulation of dual radiation action. *Radiat. Res.* **75**(3) 471–488.

Koehler A.M., Schneider R.J. and Sisterson J.M. 1977 Flattening of proton dose distributions for large-field radiotherapy. *Med. Phys.* **4**(4) 297–301.

Kraft G. 2000 Tumor therapy with heavy charged particles. *Prog. Part. Nucl. Phys.* **45**(Suppl. 2) S473–S544.

Krämer M. 2001 Treatment planning for heavy-ion radiotherapy: biological optimization of multiple beam ports. *J. Radiat. Res.* **42**(1) 39–46.

Krämer M. and Scholz M. 2000 Treatment planning for heavy-ion radiotherapy: calculation and optimization of biologically effective dose. *Phys. Med. Biol.* **45**(11) 3319–3330.

Lam G.K.Y. 1987 The survival response of a biological system to mixed radiations. *Radiat. Res.* **110**(2) 232–243.

Larsson B. 1961 Pre-therapeutic physical experiments with high energy protons. *British Journal of Radiology* **34** 143–151.

Lee M., Nahum A.E. and Webb S. 1993 An empirical method to build up a model of proton dose distribution for a radiotherapy treatment-planning package. *Phys. Med. Biol.* **38**(7) 989–998.

Liu H.H., Keall P. and Hendee W.R. (moderator) 2002 Point/Counterpoint: D_m rather than D_w should be used in Monte Carlo treatment planning. *Med. Phys.* **29**(5) 922–924.

Lomax A. 1999 Intensity modulation methods for proton radiotherapy. *Phys. Med. Biol.* **44**(1) 185–205.

Lorin S., Grusell E., Tilly N., Medin J., Blom M., Ziemann V., Reistad D. and Glimelius B. 2000 Development of a compact proton scanning system in Uppsala with a moveable second magnet. *Phys. Med. Biol.* **45**(5) 1151–1163.

Matsufuji N., Fukumura A., Komori M., Kanai T. and Kohno T. 2003 Influence of fragment reaction of relativistic heavy charged particles on heavy-ion radiotherapy. *Phys. Med. Biol.* **48**(11) 1605–1623.

Neary G.J. 1965 Chromosome aberrations and the theory of RBE. 1. General considerations. *Int. J. Radiat. Biol.* **9**(5) 477–502.

Nill S. 2001 *Development and Application of a Multi-Modality Inverse Treatment Planning System.* Ph.D. thesis, University of Heidelberg. URL `http://www.ub.uni-heidelberg.de/archiv/1802/`.

Nill S., Bortfeld T. and Oelfke U. 2004 Inverse planning of intensity modulated proton therapy. *Zeitschrift für Medizinische Physik* **14**(1) 35–40.

Nill S., Oelfke U. and Bortfeld T. 2000 A new planning tool for IMRT treatments: Implementation and first application for proton beams. In: Schlegel W. and Bortfeld T. (editors), *Proc. 13th Int. Conf. on the Use of Computers in Radiation Therapy*, pp 326–328. Heidelberg: Springer.

Noël G., Habrand J.L., Mammar H., Pontvert D., Haie-Méder C., Hasboun D., Moisson P., Ferrand R., Beaudré A., Boisserie G., Gaboriaud G., Mazal A., Kérody K., Schlienger M. and Mazeron J.J. 2001 Combination of photon and proton radiation therapy for chordomas and chondrosarcomas of the skull base: the Centre de Protonthérapie D'Orsay experience. *Int. J. Radiat. Oncol. Biol. Phys.* **51**(2) 392–398.

Oelfke U. 2002 *The Potential of Charged Particle Beams in Conformal Radiation Therapy.* Aachen: Shaker.

Oelfke U. and Bortfeld T. 2000 Intensity modulated radiotherapy with charged particle beams: Studies of inverse treatment panning for rotation therapy. *Med. Phys.* **27**(6) 1246–1257.

— 2001 Inverse planning for photon and proton beams. *Medical Dosimetry* **26**(2) 113–124.

Oelfke U., Lam G.K.Y. and Atkins M.S. 1996 Proton dose monitoring with PET: quantitative studies in Lucite. *Phys. Med. Biol.* **41**(1) 177–196.

Paganetti H. 1998 Calculation of the spatial variation of relative biological effectiveness in a therapeutic proton field for eye treatment. *Phys. Med. Biol.* **43**(8) 2147–2157.

— 2002 Nuclear interactions in proton therapy: dose and relative biological effect distributions originating from primary and secondary particles. *Phys. Med. Biol.* **47**(5) 747–764.

— 2003 Significance and implementation of RBE variations in proton beam therapy. *Technology in Cancer Research & Treatment* **2**(5) 413–426.

Paganetti H. and Goitein M. 2000 Radiobiological significance of beamline dependent proton energy distributions in a spread-out Bragg peak. *Med. Phys.* **27**(5) 1119–1126.

— 2001 Biophysical modelling of proton radiation effects based on amorphous track models. *Int. J. Radiat. Biol.* **77**(9) 911–928.

Paganetti H. and Gottschalk B. 2003 Test of GEANT3 and GEANT4 nuclear models for 160 MeV protons stopping in CH_2. *Med. Phys.* **30**(7) 1926–1931.

Paganetti H., Niemierko A., Ancukiewicz M., Gerweck L.E., Goitein M., Loeffler J.S. and Suit H.D. 2002 Relative biological effectiveness (RBE) values for proton beam therapy. *Int. J. Radiat. Oncol. Biol. Phys.* **53**(2) 407–421.

Paganetti H. and Schmitz T. 1996 The influence of the beam modulation technique on dose and RBE in proton radiation therapy. *Phys. Med. Biol.* **41**(9) 1649–1663.

Palmans H. 2003 Effect of alanine energy response and phantom material on depth dose measurements in ocular proton beams. *Technology in Cancer Research & Treatment* **2**(6) 579–586.

Parodi K., Enghardt W. and Haberer T. 2002 In-beam PET measurements of β^+ radioactivity induced by proton beams. *Phys. Med. Biol.* **47**(1) 21–36.

Pedroni E., Bacher R., Blattmann H., Böhringer T., Coray A., Lomax A., Lin S., Munkel G., Scheib S., Schneider U. and Tourovsky A. 1995 The 200-MeV proton therapy project at the Paul Scherrer Institute: conceptual design and practical realization. *Med. Phys.* **22**(1) 37–53.

Perris A., Pialoglou P., Katsanos A.A. and Sideris E.G. 1986 Biological effectiveness of low energy protons. I. Survival of Chinese hamster cells. *Int. J. Radiat. Biol.* **50**(6) 1093–1101.

Raju M.R. 1980 *Heavy Particle Radiotherapy.* New York: Academic Press.

Robertson J.B., Williams J.R., Schmidt R.A., Little J.B., Flynn D.F. and Suit H.D. 1975 Radiobiological studies of a high-energy modulated proton beam utilizing cultured mammalian cells. *Cancer* **35**(6) 1664–1677.

Rossi C.J. 1999 Conformal proton beam therapy of prostate cancer — update on the Loma Linda University Medical Center experience. *Strahlenther. Onkol.* **175**(Suppl. II) 82–84.

Russell K.R., Isacsson U., Saxner M., Ahnesjö A., Montelius A., Grusell E., Dahlgren C.V., Lorin S. and Glimelius B. 2000 Implementation of pencil kernel and depth penetration algorithms for treatment planning of proton beams. *Phys. Med. Biol.* **45**(1) 9–27.

Schaffner B., Kanai T., Futami Y., Shimbo M. and Urakabe E. 2000 Ridge filter design and optimization for the broad-beam three-dimensional irradiation system for heavy-ion radiotherapy. *Med. Phys.* **27**(4) 716–724.

Schaffner B. and Pedroni E. 1998 The precision of proton range calculations in proton radiotherapy treatment planning: experimental verification of the relation between CT-HU and proton stopping power. *Phys. Med. Biol.* **43**(6) 1579–1592.

Schettino G., Folkard M., Prise K.M., Vojnovic B., Bowey A.G. and Michael B.D. 2001 Low-dose hypersensitivity in Chinese hamster V79 cells targeted with counted protons using an charged-particle microbeam. *Radiat. Res.* **156**(5, Part 1) 526–534.

Schmid E., Roos H., Rimpl G. and Bauchinger M. 1997 Chromosome aberration frequencies in human lymphocytes irradiated in a multi-layer array by protons with different LET. *Int. J. Radiat. Biol.* **72**(6) 661–665.

Schneider U., Agosteo S., Pedroni E. and Besserer J. 2002 Secondary neutron dose during proton therapy using spot scanning. *Int. J. Radiat. Oncol. Biol. Phys.* **53**(1) 244–251.

Schneider U., Pedroni E. and Lomax A. 1996 The calibration of CT Hounsfield units for radiotherapy treatment planning. *Phys. Med. Biol.* **41**(1) 111–124.

Scholz M., Kellerer A.M., Kraft-Weyrather W. and Kraft G. 1997 Computation of cell survival in heavy ion beams for therapy. The model and its approximation. *Radiat. Environ. Biophys.* **36**(1) 59–66.

Scholz M. and Kraft G. 1994 Calculation of heavy ion inactivation probabilities based on track structure, X ray sensitivity and target size. *Radiat. Prot. Dosim.* **52**(1–4) 29–33.

Seltzer S.M. 1993 *An Assessment of the Role of Charged Secondaries from Nonelastic Nuclear Interactions by Therapy Proton Beams in Water. NISTIR Publication 5221.* Gaithersburg, MD: National Institute of Standards and Technology.

Sisterson J. (editor) 2004 *Particles* (Newsletter, Number 33). Particle Therapy Co-Operative Group (PTCOG). URL `http://ptcog.mgh.harvard.edu/`.

Skarsgard L.D. 1998 Radiobiology with heavy charged particles: a historical review. *Physica Medica* **XIV**(Suppl. 1) 1–19.

Spadinger I. and Palcic B. 1992 The relative biological effectiveness of ^{60}Co γ-rays, 55 kVp X-rays, 250 kVp X-rays, and 11 MeV electrons at low doses. *Int. J. Radiat. Biol.* **61**(3) 345–353.

Suzuki M., Kase Y., Yamaguchi H., Kanai T. and Ando K. 2000 Relative biological effectiveness for cell-killing effect on various human cell lines irradiated with heavy-ion medical accelerator in Chiba (HIMAC) carbon-ion beams. *Int. J. Radiat. Oncol. Biol. Phys.* **48**(1) 241–250.

Szymanowski H. and Oelfke U. 2002 Two-dimensional pencil beam scaling: an improved proton dose algorithm for heterogeneous media. *Phys. Med. Biol.* **47**(18) 3313–3330.

— 2003 CT calibration for two-dimensional scaling of proton pencil beams. *Phys. Med. Biol.* **48**(7) 861–874.

Tang J.T., Inoue T., Yamazaki H., Fukushima S., Fournier-Bidoz N., Koizumi M., Ozeki S. and Hatanaka K. 1997 Comparison of radiobiological effective depths in 65-MeV modulated proton beams. *British Journal of Cancer* **76**(2) 220–225.

Tepper J., Verhey L., Goitein M., Suit H.D. and Koehler A.M. 1977 *In vivo* determinations of RBE in a high energy modulated proton beam using normal tissue reactions and fractionated dose schedules. *Int. J. Radiat. Oncol. Biol. Phys.* **2**(11–12) 1115–1122.

Tilly N. 2002 *Radiobiological Investigations of Proton and Light Ion Therapy.* Ph.D. thesis, Stockholm University.

Tilly N., Brahme A., Carlsson J. and Glimelius B. 1999 Comparison of cell survival models for mixed LET radiation. *Int. J. Radiat. Biol.* **75**(2) 233–243.

Tilly N., Johansson J., Isacsson U., Medin J., Blomquist E., Grusell E. and Glimelius B. 2002 The influence of proton RBE variations in clinical proton beams. In: Tilly N., *Radiobiological Investigations of Proton and Light Ion Therapy,* Ph.D. thesis, Stockholm University.

Trofimov A. and Bortfeld T. 2003 Beam delivery sequencing for intensity modulated proton therapy. *Phys. Med. Biol.* **48**(10) 1321–1331.

Urie M., Goitein M., Holley W.R. and Chen G.T.Y. 1986 Degradation of the Bragg peak due to inhomogeneities. *Phys. Med. Biol.* **31**(1) 1–15.

Waheed A., Manzoor S., Moschini G., Cherubini R., Popa V. and Giacomelli G. 1997 A study of the radiobiological effectiveness with track etch detectors. *Radiat. Meas.* **28**(1–6) 463–466.

Wambersie A. 1999 RBE, reference RBE and clinical RBE: applications of these concepts in hadron therapy. *Strahlenther. Onkol.* **175**(Suppl. II) 39–43.

Wambersie A. and Menzel H.G. 1997 Specification of absorbed dose and radiation quality in heavy particle therapy (a review). *Radiat. Prot. Dosim.* **70**(1–4) 517–527.

Webb S. 1993 *The Physics of Three-Dimensional Radiation Therapy.* Bristol and Philadelphia: IOP Publishing.

— 1997 *The Physics of Conformal Radiotherapy.* Bristol and Philadelphia: IOP Publishing.

— 2001 *Intensity-Modulated Radiation Therapy.* Bristol and Philadelphia: IOP Publishing.

Weber U. and Kraft G. 1999 Design and construction of a ripple filter for a smoothed depth dose distribution in conformal particle therapy. *Phys. Med. Biol.* **44**(11) 2765–2775.

Weyrather W.K., Ritter S., Scholz M. and Kraft G. 1999 RBE for carbon track-segment irradiation in cell lines of differing repair capacity. *Int. J. Radiat. Biol.* **75**(11) 1357–1364.

Wilkens J.J. and Oelfke U. 2003 Analytical linear energy transfer calculations for proton therapy. *Med. Phys.* **30**(5) 806–815.

— 2004 Three-dimensional LET calculations for treatment planning of proton therapy. *Zeitschrift für Medizinische Physik* **14**(1) 41–46.

Wilson R.R. 1946 Radiological use of fast protons. *Radiology* **47** 487–491.

Wouters B.G., Lam G.K.Y., Oelfke U., Gardey K., Durand R.E. and Skarsgard L.D. 1996 Measurements of relative biological effectiveness of the 70 MeV proton beam at TRIUMF using Chinese hamster V79 cells and the high-precision cell sorter assay. *Radiat. Res.* **146**(2) 159–170.

Zaider M. and Rossi H.H. 1980 The synergistic effects of different radiations. *Radiat. Res.* **83**(3) 732–739.

List of Figures

List of Tables

Acknowledgments

First of all, I would like to thank my supervisor PD Dr. Uwe Oelfke for his support, his constant flow of ideas and suggestions for my work and numerous discussions. I am also grateful to Prof. Dr. Josef Bille for his willingness to act as the second referee.

This work was carried out at the German Cancer Research Center (DKFZ) in Heidelberg, and I wish to thank Prof. Dr. Wolfgang Schlegel for accepting me into his Department of Medical Physics in Radiotherapy. I enjoyed working with this group and profited from many interesting discussions. In particular, I would like to acknowledge the competent help from Dr. Simeon Nill regarding the *KonRad* software, and the generous assistance of Dr. Hanitra Szymanowski with the Monte Carlo simulations. But also all my other colleagues and especially my various room mates deserve thanks for providing a friendly environment, lots of cake and company at sports.

This work was supported in part by the Helmholtz Gesellschaft (grant HGF-B304) and in part by a PhD grant from DKFZ. Financial aid by the German Academic Exchange Service (DAAD Doktorandenstipendium) for my stay at the Massachusetts General Hospital in Boston is gratefully appreciated. I also thank the team at the Northeast Proton Therapy Center (NPTC) and in particular Prof. Dr. Thomas Bortfeld for their friendly welcome in Boston.

Last but not least I want to express my gratitude to Katharina Schubert for careful proof reading and continuous encouragement throughout the whole work. Ahsante sana!

In accordance with the relevant regulations,[*] parts of this work have already been published:

Wilkens J.J. and Oelfke U. 2003 Analytical linear energy transfer calculations for proton therapy *Medical Physics* **30**(5) pp 806–815.[†]

— 2004a Three-dimensional LET calculations for treatment planning of proton therapy *Zeitschrift für Medizinische Physik* **14**(1) pp 41–46.

— 2004b A phenomenological model for the RBE in therapeutic proton beams, submitted.

---

[*] Promotionsordnung der Universität Heidelberg für die Naturwissenschaftlich-Mathematische Gesamtfakultät.